Thomas Jauk, BSc

Energy-Filtered Photoemission Electron Microscopy of Surfaces, Nanoparticles and Nanostructures

MASTER'S THESIS

to achieve the university degree of

Diplom-Ingenieur

Master's degree programme: Technical Physics

submitted to

Graz University of Technology

Supervisor

Em.Univ.-Prof. Dipl.-Phys. Dr.rer.nat. Wolfgang E. Ernst

Institute of Experimental Physics

Co-Supervisor
Dipl.-Ing. Dr.techn. Florian Lackner

Graz, November 2019

AFFIDAVIT

I declare that I have authored this thesis independently, that I have not used other than the declared sources/resources, and that I have explicitly indicated all material which has been quoted either literally or by content from the sources used. The text document uploaded to TUGRAZonline is identical to the present master's thesis.

Date

Signature

Abstract

Energy-filtered photoemission electron microscopy (EF-PEEM) provides a powerful and versatile method for the investigation of a large variety of materials and the characterization of their properties. With the advent of the NanoESCA instrument (from Scienta Omicron/Focus GmbH), new and enriching possibilities in research have been opened up at the Institute of Experimental Physics. Based on a combination of an ordinary photoemission electron microscope and a tandem arrangement of two hemispherical energy analysers, this novel spectro-microscopy technique allows for visualizing the distribution of photoelectrons with high spatial, energy and momentum resolution. Employing a variety of different light sources, furthermore, enables the great versatility of the NanoESCA instrument as it provides access to a broad range of material properties and phenomena in multiple dimensions. Within the scope of this thesis the instrument has been used to study various systems, ranging from simple single crystals over exotic surfaces, such as topological insulators, to nanostructures fabricated by electron beam lithography and nanoparticles formed by the helium nanodroplet synthesis approach. Besides the helium discharge lamp, pulsed laser sources have been employed to investigate coherent electronic excitations, such as plasmons, and, furthermore, to implement a pump-probe setup for establishing time-resolved studies in the femtosecond time domain. This Master's thesis presents first experiments and results of the NanoESCA microscope, paving the way for promising future research at the Institute of Experimental Physics.

Kurzfassung

Energie-gefiltertete Photoemissionselektronenmikroskopie (EF-PEEM) verkörpert eine mächtige und vielseitige Methode zur Untersuchung von unterschiedlichsten Materialoberflächen und deren Eigenschaften. Für das Institut für Experimentalphysik ergeben sich mit dem neuen NanoESCA System (von Scienta Omicron / Focus GmbH) neue und bereichernde Möglichkeiten in der Forschung. Basierend auf einer Kombination eines gewöhnlichen Photoemissionselektronenmikroskops und einer Tandemanordnung zweier Halbkugelanalysatoren ermöglicht diese neuartige spektro-mikroskopische Methode das Abbilden der Photoelektronen mit hoher Orts-, Energie- und Winkelauflösung. Das Verwenden von unterschiedlichsten Lichtquellen entfaltet dabei erst die großartige Vielseitigkeit des NanoESCA Systems, da es Zugang zu einer Vielzahl von Materialeigenschaften und Phänomenen in mehreren Dimensionen verschafft. Im Umfang dieser Masterarbeit wurden unterschiedlichste Systeme untersucht, von einfachen Einkristallen über exotische Oberflächen, wie Topologische Isolatoren, bis hin zu Elektronstrahl lithographierten Nanostrukturen und Nanopartikeln, die mit der Heliumtröpfchenmethode hergestellt wurden. Neben der Helium-Gasentladungslampe wurden auch gepulste Laserquellen eingesetzt, um kohärente elektronische Anregungen, wie z.B. Plasmonen, und darüber hinaus ultraschnelle Vorgänge in extrem kurzen Zeitbereichen (10^{-15} s) zu untersuchen. Diese Masterarbeit präsentiert daher erste Experimente und Ergebnisse mit dem NanoESCA System, die den Weg für vielversprechende Forschung am Institut für Experimentalphysik bereiten.

Contents

List of Figures vi

List of Abbreviations viii

1 Introduction 1

2 Basics 3
2.1 Electronic Structure of Surfaces . . . 3
2.1.1 The Jellium Model . . . 4
2.1.2 Electronic States at Surfaces . . . 5
2.1.3 Work Function . . . 7
2.2 Photoemission Spectroscopy . . . 10
2.2.1 The Three-Step Model . . . 11
2.2.2 Two-Photon-Photoemission . . . 14

3 Experimental Setup 18
3.1 Instrumental Aspects of the NanoESCA Microscope . . . 18
3.1.1 Electron Optics . . . 19
3.1.2 The Imaging Double Energy Analyser (IDEA) . . . 21
3.1.3 Detection Units . . . 22
3.1.4 Principles of Operation . . . 23
3.2 Light Sources . . . 26
3.2.1 The Helium Discharge Lamp . . . 26
3.2.2 The Nanosecond Pulsed Ti:Sapphire Laser . . . 28
3.2.3 The Femtosecond Laser Setup . . . 31

4 Experimental Results 35
4.1 Instrumental Characterization Measurements . . . 35
4.1.1 The Real Space Imaging Mode . . . 36
4.1.2 The Spectroscopy Mode . . . 39
4.1.3 The k-Space Imaging Mode . . . 42
4.2 A new Investigation Method for Nanoparticles Synthesized with the Helium Droplet Approach . . . 47
4.2.1 Ag Clusters - A Spectro-microscopic Analysis . . . 47
4.2.2 Various Nanoparticles under Investigation . . . 52
4.2.3 Conclusion and Outlook . . . 57
4.3 Mapping of Surface Plasmon Polaritons . . . 58
4.3.1 Launching SPPs - ns vs. fs Laser System . . . 58

4.3.2 Multiple SPP-Generation in Al Triangle Arrays 63
4.3.3 Momentum Microscopy on Lithographed Surfaces - An Outlook . . 66
4.4 Towards Time-Resolved Photoemission Electron Microscopy 70

5 Summary and Outlook **77**

Acknowledgement **79**

Bibliography **80**

List of Figures

Fig. 2.1: Overview of the two operation modes of energy-filtered photoemission microscopy and the corresponding data evaluation 4
Fig. 2.2: Self-consistent charge density near metal surface for two different Wigner-Seitz-radii in a uniform positive background 5
Fig. 2.3: One-dimensional potential for a semi-infinite crystal and the solutions for the real part of the wavefunctions $Re\Psi$ 6
Fig. 2.4: Image potential in front of a metal surface and the square of the wave functions $|\Psi^2|$ for the lowest two image states 7
Fig. 2.5: Scheme of the Smochulowski effect. 8
Fig. 2.6: Schematic illustration of adsorbed dipoles on a metal surface. 9
Fig. 2.7: Overview of the potentials experienced by an electron with and without an external electric field 10
Fig. 2.8: Schematic of the energy levels in a solid and the corresponding electron energy distribution produced by photons of energy $h\nu$ 11
Fig. 2.9: Photoemission spectroscopy as a three-step process 12
Fig. 2.10: Photo-excitation from an initial state E_i to a final state E_f and the inelastic mean free path of electrons in solids 13
Fig. 2.11: Momentum relations at the solid-vacuum interface 14
Fig. 2.12: Elementary excitation processes in two-photon photoemission 16
Fig. 2.13: Overview of the time scales of laser driven excitation and relaxation processes 16

Fig. 3.1: Schematic layout of the NanoESCA instrument 19
Fig. 3.2: Scheme of the Imaging Double Energy Analyser (IDEA) 22
Fig. 3.3: Schematic of a channeltron and of the imaging unit 23
Fig. 3.4: Energy scheme of a photoemeission experiment with x-ray radiation . . . 24
Fig. 3.5: The three main operating modes of the NanoESCA 25
Fig. 3.6: Schematic layout of the VUV source HIS 13 27
Fig. 3.7: Spatial beam profiles for He I (left ordinate) and He II (right ordinate) resonance radiation 28
Fig. 3.8: Optical layout of the Evolution-15 29
Fig. 3.9: Optical layout of the Ti:sapphire oscillator 30
Fig. 3.10: Optical layout of the second harmonic generation and extraction of the second harmonic of the Ti:sapphire laser 31
Fig. 3.11: A typical cavity design of a self-mode-locked Ti:sapphire laser using the Kerr lens mode-locking process 32
Fig. 3.12: The ultrafast laser setup in the PEEM laboratory 34

Fig. 4.1: EF-PEEM images of a Cu(110) surface . . . 37
Fig. 4.2: EF-PEEM image of Ag bar structures for determining the lateral resolution 38
Fig. 4.3: UPS spectrum of a Cu(110) surface . . . 40
Fig. 4.4: Determination of the work function of a Cu(110) surface and the total energy resolution . . . 41
Fig. 4.5: Determination of the work function of a monolayer H_2TPP on a Ag(100) surface and the total energy resolution . . . 42
Fig. 4.6: k-space images of the Cu(110) 3d-band . . . 43
Fig. 4.7: k-space images and the band dispersion of the Cu(110) sp-band and the surface states . . . 44
Fig. 4.8: Band structure of Bi_2Se_3 . . . 45
Fig. 4.9: Photoemission horizon from a highly oriented pyrolytic graphite (HOPG) surface . . . 46
Fig. 4.10: EF-PEEM image and the corresponding UPS-spectra of the pristine p-type Si-wafer region and the Ag cluster deposited region . . . 49
Fig. 4.11: Spatial resolution and size distribution of Ag clusters deposited on a p-type Si-wafer . . . 50
Fig. 4.12: 2PPE images of the Ag cluster . . . 51
Fig. 4.13: PEEM image and UPS spectra of the contaminated p-type Si-wafer and the deposited Au cluster region . . . 52
Fig. 4.14: UPS spectra and EF-PEEM images of a pristine p-type Si-wafer and deposited ZnO cluster region . . . 53
Fig. 4.15: Work function contrast between the ZnO cluster region and the pristine p-type Si-wafer . . . 54
Fig. 4.16: Work function maps of the ZnO region and the pristine p-type Si-wafer . 55
Fig. 4.17: Averaged UPS spectra of V_2O_5 particles deposited on ITO . . . 56
Fig. 4.18: 2PPE-EF-PEEM images of the nanosecond and femtosecond laser spots 60
Fig. 4.19: Mapping the Moiré pattern initiated by a 30 μm 30 μm triangle triangle 61
Fig. 4.20: Illustration of space charge effects and their impact onPEEM measurements. . . . 62
Fig. 4.21: Moiré pattern of a 3 μm aluminium triangle array . . . 63
Fig. 4.22: Moiré pattern of a 30° rotated 3 μm aluminium triangle array . . . 64
Fig. 4.23: Moiré pattern of a 60° rotated 3 μm aluminium triangle array . . . 65
Fig. 4.24: Moiré fringe spacing: Theory and Experiment . . . 66
Fig. 4.25: EF-PEEM images of Al wave guides . . . 67
Fig. 4.26: PAD patttern and band dispersion of the Al wave guides . . . 69
Fig. 4.27: 2PPE-EF-PEEM images of the spatially and temporally overlapped pump and probe pulses . . . 71
Fig. 4.28: Schematic of the two-photon photoexcitation processes by two phase-coherent pulses . . . 73
Fig. 4.29: Interferometric 2-pulse correlation trace of Bi_2Se_3 . . . 74
Fig. 4.30: Interferometric 2-pulse correlation trace of Bi_2Se_3 and its phase averaged component . . . 75

List of Abbreviations

PEEM	Photoemission electron microscopy
EF-PEEM	Energy-filtered photoemission electron microscopy
2PPE	Two-photon-photoemission
TR-2PPE	Time-resolved two-photon-photoemission
STM	Scanning tunneling microscopy
ESCA	Electron spectroscopy for chemical analysis
VUV	Vacuum ultraviolet
UV-PEEM	Ultraviolet photoemission electron microscopy
CW	Continuous wave
IDEA	Imaging double energy analyser
HSA	Hemispherical energy analyser
MCP	Multichannel plate
CA	Contrast aperture
FA	Field aperture
UHV	Ultra-high vacuum
SHG	Second harmonic generation
GVD	Group velocity dispersion
LEEM	Low-energy electron microscopy
UPS	Ultraviolet photoemission spectroscopy
IPES	Inverse photoemisssion spectroscopy
ARPEs	Angular resolved photoemission spectroscopy
1PPE	One-photon-photoemission
VBM	Valence band maximum
PAD	Photoemission angular distribution
ITO	Indium tin oxide
LSP	Localized surface plasmon
LSPR	Localized surface plasmon resonance
TEM	Transmission electron microscopy

XPS	X-ray photoemission spectroscopy
UV-VIS	Ultraviolet-visible
DFT	Density functional theory
EBL	Electron beam lithography
SPP	Surface plasmon polariton
I2PC	Interferometric 2-pulse autocorrelation trace of photoemission

Chapter 1

Introduction

Entering a new field in physics proves to be quite difficult since know-how has to be developed by self-studying, researching and experimenting whereas groups with experience for decades can just pass on their knowledge to next generations. Such a new research field has arisen for the Institute of Experimental Physics with the advent of an energy-filtered photoemission electron microscope (EF-PEEM), the so-called NanoESCA instrument [1]. Based on a combination of an ordinary photoemission electron microscope and a tandem arrangement of two hemispherical energy analysers this novel PEEM technique allows for visualizing the distribution of photoelectrons with high spatial, energy and momentum resolution. Employing a variety of different light sources, furthermore, enables the great versatility of the NanoESCA instrument as it provides access to a broad range of material properties and phenomena in multiple dimensions, surpassing, thereby, comparable PEEM systems. However, in order to exploit the full potential of the microscope one has to acquire a broad knowledge about the instrument covering the strengths, weaknesses, operating issues and especially the limitations. Therefore, a pioneering work, completely addressed to the NanoESCA instrument, is essential to make any progress in realizing existing intentions and to gain a broad perspective of possible promising research fields.

This Master's thesis presents first experimental results from the NanoESCA, paving the way for future interesting and insightful experiments. Within the scope of this thesis, the instrument has been used to study various systems ranging from simple single crystals over exotic surfaces, such as the topological insulator Bi_2Se_3, to nanostructures fabricated by electron beam lithography and nanoparticles formed by the helium nanodroplet synthesis approach. Besides the helium discharge lamp for classical photoemission spectroscopy of the valence band structure, pulsed laser sources have been employed to investigate multiphoton photoemission processes and, furthermore, to implement a pump-probe setup for establishing time-resolved studies in the femtosecond time domain. The NanoESCA photoemission electron microscope, thereby, can unveil static and dynamic processes of photoexcited electrons by exploiting a high energy resolution of only a few 100 meV together with a good spatial and momentum resolution down to 30 nm and sub-$Å^{-1}$, respectively. [2,3] Furthermore, the temporal resolution is only restricted by the duration of the laser pulses and can in principle reach the attosecond time domain. [4] These high resolutions usually imply a reduction in electron transmission and, thus, longer image acquisition times, emphasizing the importance of knowing the individual components' influences in the electron optics. [5] However, apart from the sophisticated technique including the magnifying, analysing and detecting scheme, an equally important role has to be attributed to the photoexcitation governed by the light source and its polarization.

Consequently, a part of this thesis also focuses on the photoemission process and the underlying physics.

In chapter 2, the fundamental aspects of photoemission are briefly reviewed, providing an overview about the electronic structure at surfaces, the work function and photoemission spectroscopy. A detailed description about the NanoESCA instrument and the employed light sources is given in chapter 3. Subdivided into four subsections, the electron optics, the imaging double energy analyser, the detection units and the working principle of the energy-filtered photoemission electron microscope are compactly summarized from Ref. [5], the manuals [2,3] and the experience gained so far. As already mentioned, a major element in photoemission microscopy is the photoexcitation process. Therefore, the cw helium discharge lamp capable of producing 21 eV and 41 eV photon energy and the two pulsed Ti:sapphire laser systems, providing nanosecond to femtosecond pulses with photon energies of a few eV, are introduced. Furthermore, the pump-probe setup, consisting of a Michelson interferometer, is presented, which allows for time-resolved studies. In chapter 4 first experimental results are shown. At the beginning of this chapter the relevant operating modes, the information which can be extracted from each mode, and the limitations in space, energy and momentum resolved experiments are introduced by instrumental characterization measurements. Furthermore, first experiments have been performed to present the applicability of investigating plasmonic nanoparticles formed by the helium nanodroplet synthesis approach. Followed by another class of plasmon oscillations, first concrete results of mapping surface plasmon polaritons obtained from aluminium triangles, fabricated by electron beam lithography, are demonstrated, paving the way for promising future research in the field of plasmonics. The last section of chapter 4 introduces first time-resolved measurements and shows the current deficiencies, which have to be overcome in the near future in order to perform competitive research in the field of ultrafast microscopy. Chapter 5, finally, summarizes all relevant advances and results and, additionally, gives an outlook to future studies carried out with the NanoESCA microscope.

Chapter 2

Basics

Photoemission spectroscopy has emerged as a powerful technique for unravelling the electronic structure of surfaces. Due to the worldwide advances in nanoscience and nanotechnology spatially resolved spectroscopic examination has become very important in order to unveil or explain a variety of different effects, also in prospect of future applications. Consequently, classical photoemission spectroscopy has also evolved into a microscopy method, the so-called energy-filtered electron microscopy (EF-PEEM), from which substantial information about spatial and angular distribution of the photoelectrons can be extracted. A good overview of the two main microscopy modes is depicted in Fig. 2.1, taken from Ref. [5]. By absorbing energy from photons, electrons are emitted from the sample if the kinetic energy is high enough to overcome the binding energy and the work function. A strong electric field between the sample and the objective lens is used to accelerate the free electrons into the microscope. After passing several electrostatic lenses and the imaging double energy analyser, the photoelectron distribution is projected onto a two-dimensional screen. By changing the settings in the objective lens configuration the microscope can either acquire a spatially resolved image of the sample by integrating over all emission angles in each point (real-space microscopy) or map the momentum (angular) distribution by integrating over the selected sample area (momentum microscopy). By recording image series for each kinetic energy, on the one hand (real-space microscopy) photoemission spectra can be extracted from different positions on the sample and their chemical composition may be analysed. On the other hand, the energy-momentum dispersion can be deduced by cutting the image-stack along high-symmetry axis.
As already mentioned, a basic knowledge about photoemission processes is necessary for the understanding of the working principle of an energy-filtered photoemission microscope and, furthermore, for implementing relevant experiments for future research. This chapter should provide a brief overview about the fundamental aspects of photoemission. This includes general considerations about the electronic structure at the surface, the work function and the fundamental aspects of photoemission such as the three-step model and two-photon photoemission.

2.1 Electronic Structure of Surfaces

Since this master's thesis is all about photoemission, a brief section of the electronic structure of surfaces should not be omitted. Due to the truncation of the infinite bulk crystal, a change of coordination occurs which can lead to reconstruction or relaxation

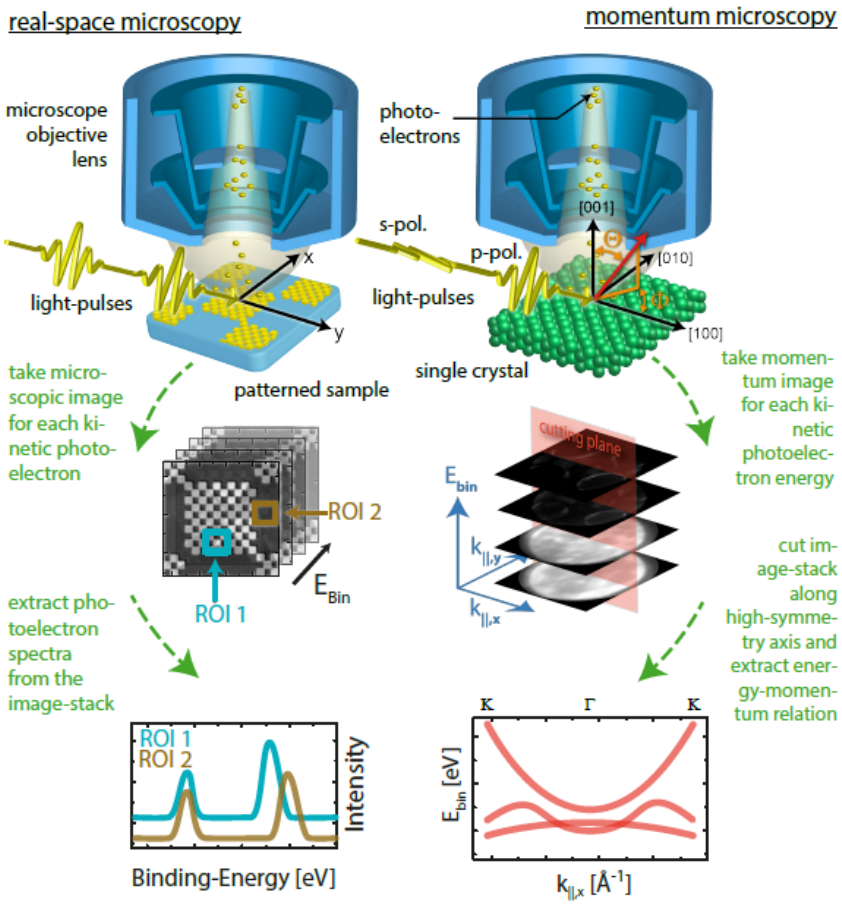

Figure 2.1: Overview of the two operation modes of energy-filtered photoemission microscopy and the corresponding data evaluation. Taken and edited from Ref. [5].

and, consequently, to a modification of the phonon dispersion and the electronic structure at the surface.

2.1.1 The Jellium Model

The jellium model [6] tries to explain the behaviour of the valence electron density at the surface as a result of the abrupt truncation of the positive ion core distribution. In this theory the electrons are assumed to be an electron gas, which includes exchange and correlation effects and moves in a uniform background of positive charge with a density of

$$\rho_+(z) = \begin{cases} \rho, & \forall\, z \leq 0 \\ 0, & \forall\, z > 0. \end{cases} \tag{2.1}$$

The only parameter in this model is the electron density ρ_e:

$$\frac{1}{\rho_e} = \frac{4}{3}\pi r_s^3, \tag{2.2}$$

where r_s represents the Wigner-Seitz-radius.
In Fig. 2.2 calculated results for the electron charge densities with different values of r_s are depicted. The electron density decreases smoothly and spills out into the vacuum site ($z > 0$) resulting in a surface dipole. Furthermore, an oscillatory behaviour, the so-called Friedel oscillations [7], can be seen, originating from the interference of Bloch waves at the potential barrier.

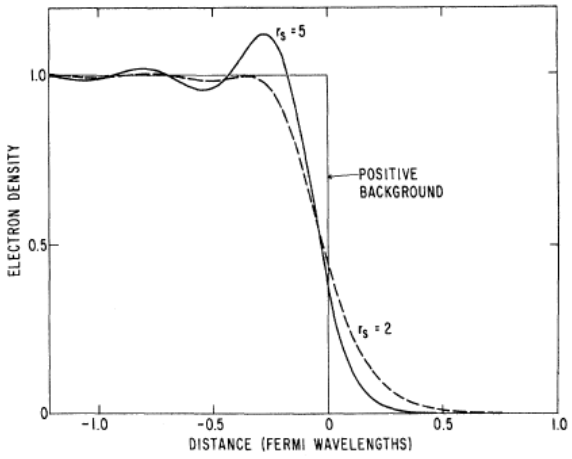

Figure 2.2: Self-consistent charge density near metal surface for two different Wigner-Seitz-radii in an uniform positive background [6]

However, the jellium model fails to describe two dimensional variations of the electron density distribution at the surface. Consequently, a model was developed in which the ions, localized at the sites of a regular half lattice, are represented by appropriate pseudopotentials and DFT (density functional theory) calculations, thereby, provides plausible solutions for the two dimensional electronic density [6]. However, within the scope of this thesis the qualitative picture of the Jellium model is sufficient in order to describe relevant effects, such as the work function.

2.1.2 Electronic States at Surfaces

As already mentioned, due to the truncation of the infinite bulk crystal the electronic structure of the valence and conduction bands changes at the surface. Additional states appear such as Shockley surface states [8] and image potential states [9, 10]. In this subsection the origin of these two states will briefly be discussed.

Considering a one-dimensional potential for a semi-infinite crystal, see Fig. 2.3(a), the Schrödinger equation

$$\left[-\frac{\hbar^2}{2m}\frac{\partial^2}{\partial z^2} + V(z)\right]\Psi(z) = E\Psi(z) \tag{2.3}$$

results in two qualitatively different types of solutions. The first solution corresponds to bulk states Fig. 2.3(b) representing standing Bloch waves inside the crystal and an exponentially decaying tail reaching into the vacuum. The second solution covers so-called surface states Fig. 2.3(c) which decay exponentially both into the vacuum and the bulk

crystal. Surface states are localized close to the surface and exist only in the projected band gaps of the bulk solutions, i.e. in the case of semiconductors in the forbidden band gaps and for metals in local gaps of the projected band structure. A special class of surface states is occupied by topological insulators which behave as an insulator in the bulk but are conducting at the surface. [11] A combination of spin-orbit interactions and time-reversal symmetry enables these surface states exhibiting a linear Dirac-like dispersion with a protected crossing point, the so-called Dirac cone. [11] Beside the "true" surface states there are also surface resonances, an interference between bulk and surface states forming a wave function with a superelevated amplitude at the surface.

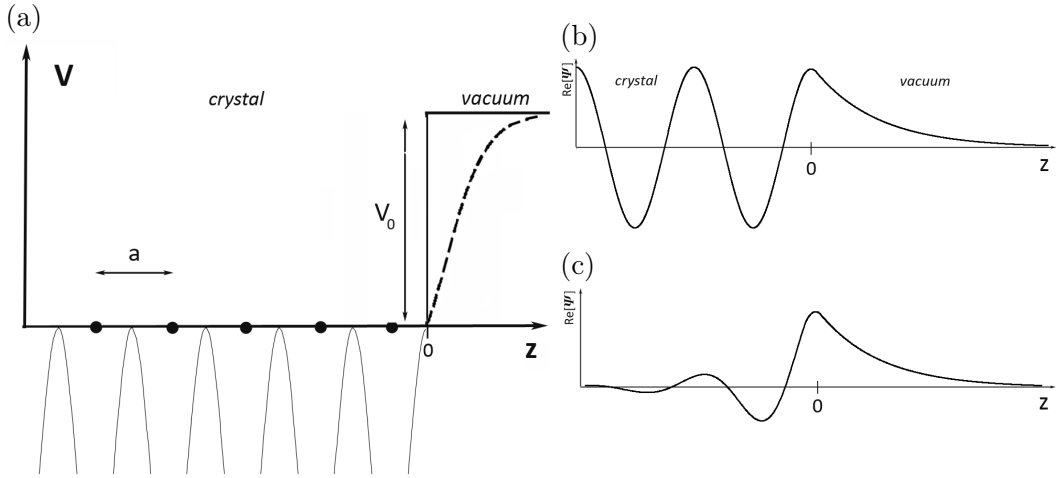

Figure 2.3: (a) One-dimensional potential for a semi-infinite crystal. [12] (b) Real part of the wave function from the one-dimensional Schrödinger equation representing the first solution, the bulk states characterized by a Bloch behaviour inside the crystal and an exponentially decaying tail inside the vacuum. [13] (c) The second solution corresponds to so-called surface states, which decay into the vacuum and the bulk crystal. [13]

Another type of unoccupied electronic states are image potential states which do not have their origin in the broken translational symmetry. When an electron is excited into a projected band gap it experiences an attractive force associated with its image potential

$$V(z) = E_{vac} - \frac{1}{4\pi\epsilon_0}\frac{e^2}{4z}. \tag{2.4}$$

This results in a series of bound states which can be described in analogy to Rydberg states in atomic or molecular systems, see Fig. 2.4,

$$E_n \approx E_{vac} - \frac{R_y}{16(n+a)^2}. \tag{2.5}$$

Furthermore, time-resolved two-photon-photoemission (TR-2PPE) studies of image potential states revealed lifetimes on the order of several tens of femtoseconds [15–17]. A brief discussion about time-resolved two-photon photoemission (TR-2PPE) and image potential states is given in subsection 2.2.2.

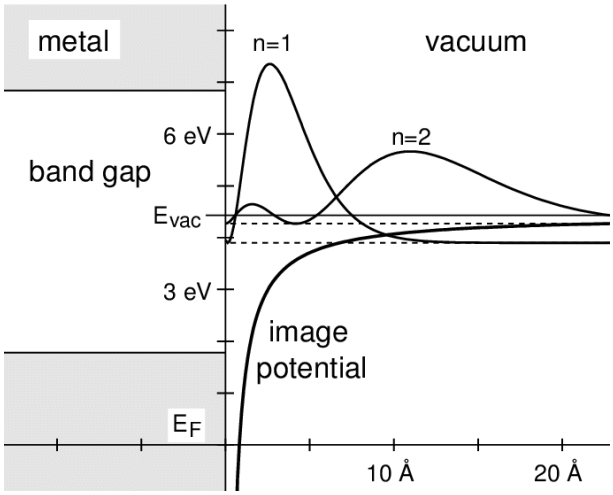

Figure 2.4: Image potential in front of a metal surface and the the square of the wave functions $|\Psi^2|$ for the lowest two image states. [14]

2.1.3 Work Function

In general, the work function Φ is the energy required to remove an electron completely from a metal surface. A more detailed description considers, again, the assumption of a semi-infinite crystal, the work function is the minimum energy difference between a first ground state of an N electron system with energy E_N and a second ground state of an $N-1$ electron system with energy E_{N-1} plus an energy contribution of an electron at infinite distance away from the surface on the vacuum side ($\Phi_{+\infty}$) [18]

$$\Delta E = \Phi = (E_{N-1} + \phi_{+\infty}) - E_N. \tag{2.6}$$

Using the definition of the electrochemical potential $\mu = E_N - E_{N-1}$ yields to

$$\Phi = \phi_{+\infty} - \mu. \tag{2.7}$$

Here, the work function can be seen as the difference between the vacuum level $E_{vac} = \phi_{+\infty}$ and the Fermi energy $E_F = \mu$. For a quantitative discussion within the scope of the Jellium model, Φ can be divided into two contributions: a surface $\Delta\phi = \phi_{+\infty} - \phi_{-\infty}$ and a bulk part $\bar{\mu} = \mu - \phi_{-\infty}$ [19]. The surface part $\Delta\Phi$ is determined by the surface dipol, whereas the bulk part consists of the Fermi energy of the free electron gas and the exchange-correlation-potential describing the energy change by cooperatively behaving electrons. For instance, for an electron approaching a metal surface, the metal electrons will move to screen the external field. If the electron gets inside the metal, again, the metal electrons will move away from the electron leaving an "exchange correlation hole". Lang and Kohn showed in their work [6] that the work function calculations with the Jellium model agree with experimental results. However, the simple model fails when considering anisotropy of the surface.

In the following paragraphs the influences on work functions, such as different crystal faces, stepped surfaces, adsorbates and external electric fields, will be discussed.
In order to describe the surface dependence of the work function in a qualitative way the

so-called Smoluchowski effect [20] is discussed in the following. Considering Wigner-Seitz cells, in the bulk each of this cell carries equal amounts of positive and negative charge and has no dipole moment. At the surface, the negative charge does not abruptly drop to zero at the boundary of the Wigner-Seitz cells. Moreover, the charge redistributes from the protruding parts of the Wigner-Seitz cells to the grooves, see Fig. 2.5. This smoothing leads to an additional dipole, which is aligned antiparallel to the surface dipole originating from the spill-out effect, c.f. subsection 2.1.1. Consequently, the Smochulowski effect tends to reduce the work function. [18]

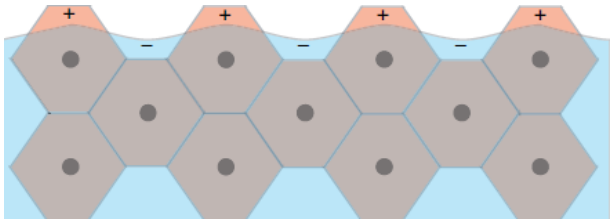

Figure 2.5: Scheme of the Smochulowski effect. The positive background is smoothed by negative charge distribution resulting in a net dipole which is superimposed to the dipole layer caused by the spill-out effect. [18]

In this qualitative picture, the more corrugated a surface is, the more the work function is reduced. This also holds for differently oriented surfaces, for a closed-packed surface such as Cu(111) the Smochulowski smoothing does not have a large impact whereas more open structures such as Cu(110) are effected more strongly. EF-PEEM studies on a polycrystalline copper surface [21] show variations in the local work function of grains having different crystalline orientation, e.g. for a Cu(111) grain, a work function of 4.8 eV was measured whereas the Cu(110) grain revealed a lower work function of 4.4 eV. Furthermore, stepped surfaces are also strongly influenced by the redistribution of the negative charge, which was experimentally verified by STM studies [22], unravelling a local work function decrease when crossing a monoatomic step.

In surface science, a clean surface is crucial in order to investigate processes under controlled conditions. In principle, clean single crystalline surfaces are provided *in vacuo* by applying several sputtering and annealing cycles and then, molecules, thin films or nanoparticles can be assembled under ultra high vacuum conditions. Sample processing under these conditions guarantees trouble-free measurements. However, in the scope of this master's thesis most of the EF-PEEM studies were performed without a preparation chamber leading to a complication of interpretations. Thus, hydrogen, water or hydrocarbons adsorb very likely at a surface, the influences of adsorption, especially on the work function, should briefly be discussed.
The Topping model [23] assumes an arrangement of dipoles as a planar network on the surface, see Fig. 2.6. The distance between the dipoles decreases gradually with increasing surface coverage, leading to a reduction of the work function. An advanced model [24] additionally considers the electronegativity of the adsorbate and the metal surface for describing the direction of the electron transfer. For alkalis adsorbed on meal surfaces a coverage-dependent work function reduction can quite well be predicted by using these simple models, as shown in Ref. [25], e.g. the absorption of potassium on a Re(001) surface leads to a charge transfer from the adsorbate to the metal, forming a dipole at the

surface as illustrated in Fig. 2.6. Increasing the coverage results in a further reduction until a point is reached where the work function starts to increase and finally converges to the usual bulk work function of potassium. However, due to small differences in the electronegativity, such as for carbon absorbed on Au(110) [26], the considerations according to Topping and Gyftopoulos fail. Therefore, modern molecular dynamics simulations have to be used in order to describe the surface dynamics correctly.
Despite all those effects, the work function unveils a useful parameter in energy-filtered microscopy, e.g. for contrast imaging and also for generating work function maps.

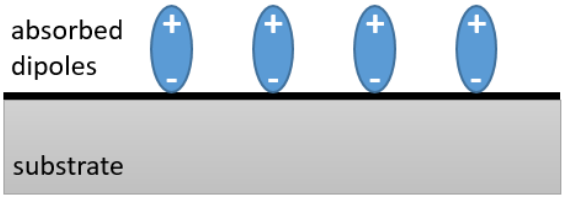

Figure 2.6: Schematic illustration of adsorbed dipoles on a metal surface.

The last influence on the work function discussed in the scope of this thesis is an external electric field. This is an important aspect, considering that in the case of the NanoESCA, the emitted photoelectrons are accelerated by an extractor voltage V_{ext} with a magnitude of several kilovolts. A detailed description of the effect of an accelerating field on the work function can be found in Refs. [5, 27].
The electrostatic potential of an electron outside the surface can be described by the image potential

$$V(r) = -\frac{e}{16\pi\epsilon_0 r} \tag{2.8}$$

with the distance r between the surface and the electron. This potential converges to the vacuum level $E_{vac} = \Phi_{+\infty}$, see Fig. 2.7(a). In the presence of a constant electrical field E_{acc} outside the sample surface the potential is modified, leading to a reduction of the work function by $\delta\phi$ due to the so-called Schottky effect [28], which can be calculated:

$$\delta\phi = \sqrt{\frac{e}{4\pi\epsilon_0}}\sqrt{E_{acc}}, \tag{2.9}$$

with

$$E_{acc} = \frac{V_{ext} - V_{spl}}{d_{obj}}, \tag{2.10}$$

where V_{spl} is the sample voltage for filtering the electrons according to their kinetic energy and d_{obj} the distance between the extractor and the sample. In Fig. 2.7(b), the work function difference $\delta\phi$ as a function of the extractor voltage is depicted. V_{spl} was thereby neglected due to $V_{spl} \ll V_{ext}$ and d_{obj} was set to $d_{obj} = 1.830$ mm. For the typical extractor voltage of 12 kV, the reduction of the work function is approximately 0.1 eV. The Schottky effect has to be taken into account when comparing measurements with different extractor voltages to each other.

(a) (b)

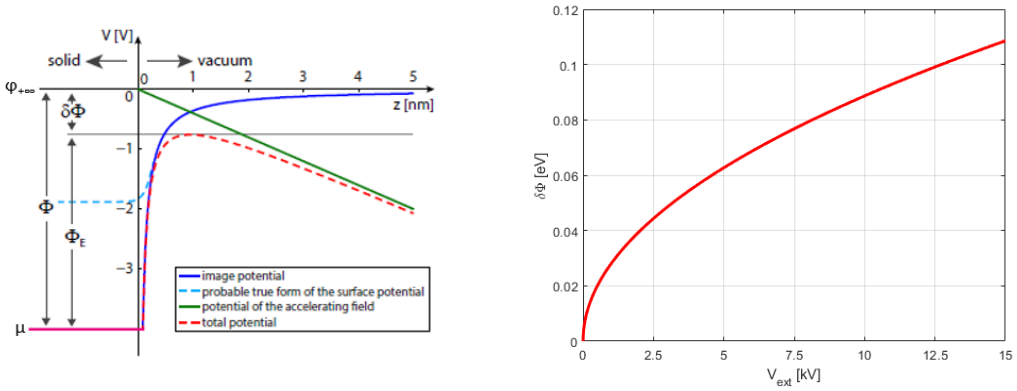

Figure 2.7: (a) Overview of the potentials experienced by an electron with and without an external electric field. Edited from [5] (b) Calculated work function reduction $\delta\phi$ depending on the extractor voltage V_{ext}.

2.2 Photoemission Spectroscopy

In this section the fundamental aspects of photoemission spectroscopy should be reviewed briefly. One part introduces the main idea of the three-step model [29], whereas the other part focuses on two-photon photoemission (2PPE) and, furthermore, on time-resolved 2PPE. For a more detailed discussion the reader is referred to the literature, such as Refs. [5], [30] or [31].

The phenomenon of photoemission was detected by Hertz [32] in 1887 and in 1905, Einstein [33] explained the effect by an energy quantization of the electro-magnetic field. The proportionality factor in Einstein's equation, Planck's constant h, was experimentally verified by Millikan [34] eleven years later. Einstein's equation can be summarized, considering Millikan's experiments, as follows:

$$E_{kin,max} = eU = h\nu - \Phi, \tag{2.11}$$

the maximum kinetic energy $E_{kin,max}$ of electrons depends on the quantized energy of photons with frequency ν and the work function Φ. This kinetic energy is thereby equivalent to the kinetic energy of electrons accelerated by a potential difference U.
Considering a solid material, the electronic structure is subdivided into core levels, a valence and a conduction band. The energy which separates the occupied (the valence band) and unoccupied states (the conduction band) is called Fermi energy E_F. In the case of a metal the Fermi energy is at the top of the valence band, whereas for semiconductor and insulators the Fermi level lies in a band gap between the valence and the conduction band and the electronic states are only filled up to the valence band edge. The work function defines the energy difference between the vacuum level E_{vac} and the Fermi energy. If light with a photon energy of $h\nu$ impinges on a solid sample, the energy distribution of

photoemitted electrons can be measured by analysing their kinetic energies. One can then determine the corresponding binding energies E_{bin}:

$$E_{kin} = h\nu - \Phi - E_{bin}, \tag{2.12}$$

which are characteristic for each solid and can unveil the prevailing elemental components and the chemical composition (e.g. oxidation states). Hence, photoemission spectroscopy, in this context, is also called Electron Spectroscopy for Chemical Analysis (ESCA). Fig. 2.8 shows schematically how the energy-level diagram and the energy distribution of photoemitted electrons relate to each other.

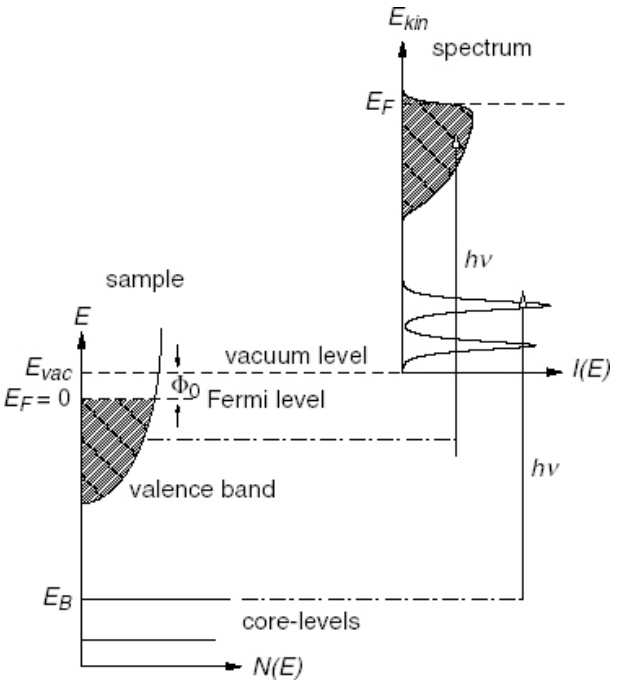

Figure 2.8: Schematic of the energy levels in a solid and the corresponding electron energy distribution produced by photons of energy $h\nu$. [35] Electrons from core-levels and the valence band, represented by the density of states $N(E)$, can be excited above the vacuum level by photons with energy $h\nu > E_B + \Phi_0$ and, thus, the photoemission spectrum $I(E)$ can be measured. The spectrum is a convolution of the density of states, the Fermi Dirac distribution and the linewidth of light source. Furthermore, a background, not shown here, is generated by secondary electrons.

2.2.1 The Three-Step Model

The three-step model [29] is a purely phenomenological approach for interpreting the photoemission process separated into three steps: The excitation of the photoelectron, the transport to the surface and the transmission through the surface into vacuum. The three-step model is sketched in Fig. 2.9. These three steps are treated within the same framework in the so-called one-step model [36,37]. However, in many cases the three-step model proved to be a useful approximation. In the following paragraphs all steps are discussed separately.

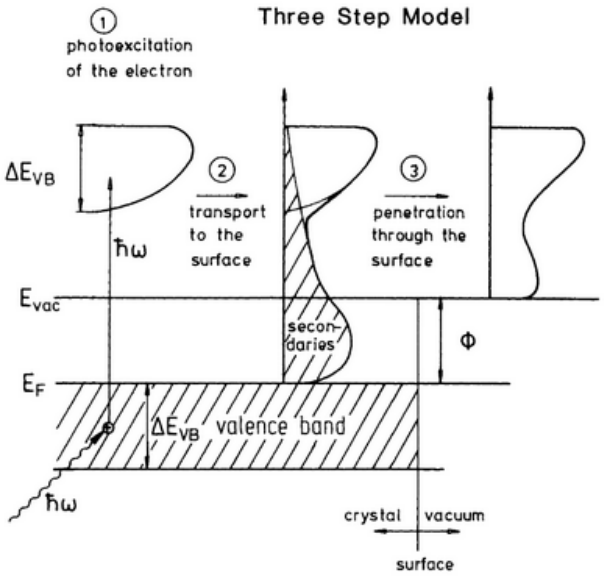

Figure 2.9: Photoemission spectroscopy as a three-step process. [30] In the first step, electrons from the valence band are excited to final states above the vacuum level. The second step covers the transport to the surface and, thus, the generation of secondary electrons due to inelastic scattering. In the third and last step, the photoexcited electrons are transmitted through the surface while conserving the parallel component of the wave vector. The final spectrum contains information about the valence band and, due to the cut-off of the secondary electrons, the work function.

Step 1: Photo-excitation

In solids, the electronic states are described by bands and the wave functions of electrons can be represented by Bloch functions, written without considering orbital momentum and spin quantum number as

$$|\Psi_n(\mathbf{k})\rangle = |n, \mathbf{k}\rangle\,, \tag{2.13}$$

which have eigenstates $E_n(\mathbf{k})$, where n is the band index and $\mathbf{k}$ the electron wave vector. Considering an optical transition between two bands, as indicated in Fig. 2.10(a), an electron with energy E_i from an initial band $|i, \mathbf{k_i}\rangle$ is transferred into a final state E_f above the vacuum level with the corresponding wave function $|f, \mathbf{k_f}\rangle$. Note that this is a momentum conserving transition. The transition probability W_{fi} of the photo-excitation can be described by using Fermi's golden rule:

$$W_{fi} = \frac{2\pi}{\hbar} \cdot |\langle f, \mathbf{k_f}| \mathcal{H} |i, \mathbf{k_i}\rangle|^2 \cdot \delta(E_f(\mathbf{k_f}) - E_i(\mathbf{k_i}) - h\nu) \tag{2.14}$$

$$= \frac{2\pi}{\hbar} \cdot m_{fi} \cdot \delta(E_f(\mathbf{k_f}) - E_i(\mathbf{k_i}) - h\nu), \tag{2.15}$$

where m_{fi} is the transition matrix and $\mathcal{H}$ the perturbing Hamiltonian consisting of the momentum operator and the vector potential of the electric field. The δ-function describes the energy conservation in the excitation.

Step 2: Transport to the surface

After photo-excitation the electrons are transported to the surface. On their way they may loose energy due to various scattering processes, such as electron-electron, electron-plasmon, electron-phonon or electron-defect scattering. These scattered electrons, the so-called secondary electrons, contribute to the continuous background of the photoemission spectrum. The probability of an electron reaching the surface can be described by the inelastic mean free path $\lambda(E, \mathbf{k})$, which depends on the energy E, the wave-vector $\mathbf{k}$ and, furthermore, on the crystallographic direction. The energy dependence of the inelastic mean free path, proposed as a universal curve [38], is depicted in Fig. 2.10(b). For kinetic energies around 10 eV, an inelastic mean free path of approximately 1 nm can be assumed. Maximum surface sensitivity can be reached with kinetic energies around 50 eV.

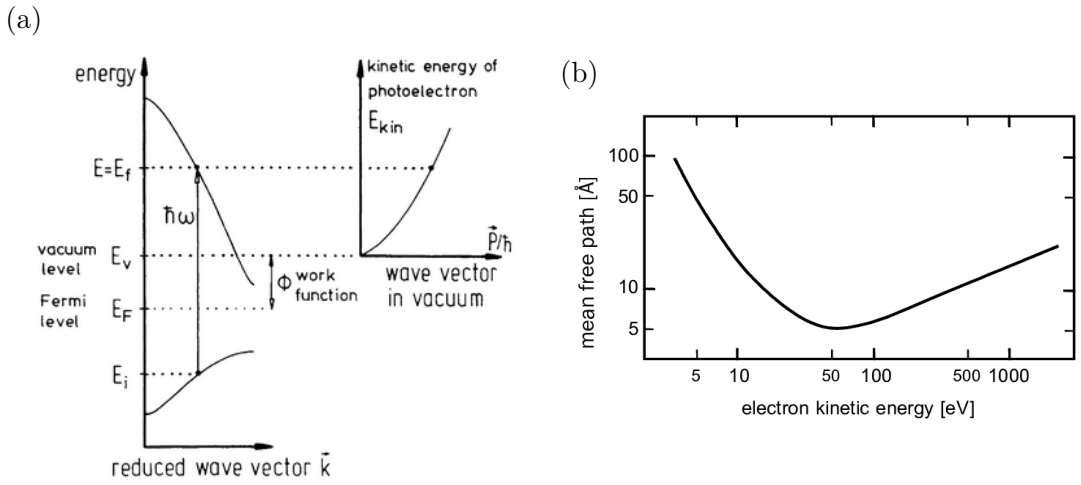

Figure 2.10: (a) Photo-excitation from an initial state E_i to a final state E_f above the vacuum level and the kinetic energy of the photo-electrons in the vacuum as a function of its wave vector. [30] (b) Inelastic mean free path of electrons in solids. [39]

Step 3: Transmission through the surface

The last step of the three-step model is the transmission of the photo-excited electron through the surface. The momentum relations at the solid-vacuum interface are shown in Fig. 2.11.

An electron can escape from the surface if the component of the kinetic energy normal to the surface inside the crystal is sufficient to overcome the surface potential barrier:

$$E_{kin,\perp} = \frac{(\hbar \mathbf{k_f}_{,\perp})^2}{2m} \geq E_{vac} - E_0, \tag{2.16}$$

with E_0 as the bottom of the valence band. The other electrons with insufficient energy are totally reflected back into the bulk. The parallel component of the wave vector $\mathbf{k_f}$ of

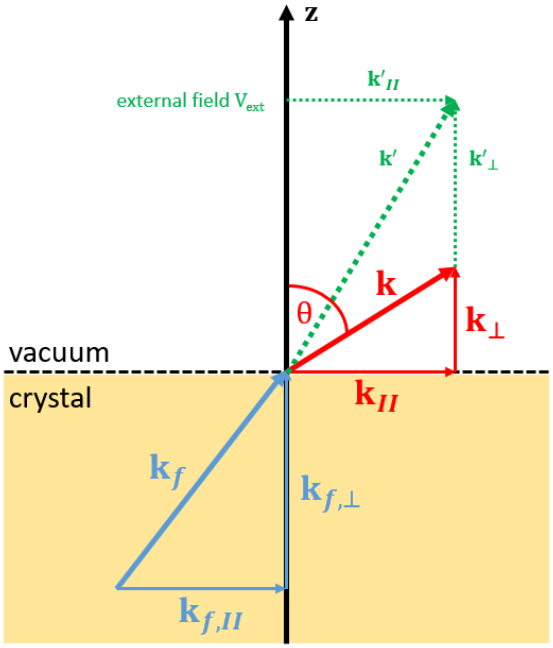

Figure 2.11: Momentum relations at the solid-vacuum interface. The individual momentum components, the condition for the transmission and the conservation of the parallel component are described in the text.

the photo-excited electron is conserved during the refraction at the surface potential

$$\mathbf{k}_{\parallel} = \mathbf{k}_{\mathbf{f},\parallel} + \mathbf{G}_{\mathbf{f},\parallel}, \tag{2.17}$$

with the surface parallel component of the reciprocal lattice vector $\mathbf{G}_{\mathbf{f},\parallel}$. The kinetic energy of the electron outside the surface can be written as

$$E_{kin} = \frac{(\hbar\,\mathbf{k})^2}{2m} = \frac{\hbar^2}{2m}(\mathbf{k}_{\perp}{}^2 + \mathbf{k}_{\parallel}{}^2). \tag{2.18}$$

Consequently, due to the conservation of $\mathbf{k}_{\mathbf{f},\parallel}$, the parallel component of the wave vector outside the surface can be determined by Snell's law

$$k_{\parallel} = \sqrt{\frac{2m}{\hbar^2} E_{kin}} \sin\theta. \tag{2.19}$$

If an electric field is applied between the sample and the extractor, as in the case of the NanoESCA, the perpendicular component of the moment $\mathbf{k}_{\perp}$ will be increased, whereas the parallel component will be conserved. This means for k-space imaging with the EF-PEEM that the distribution of the parallel momenta of the primary electrons reflects the band structure of the crystal.

2.2.2 Two-Photon-Photoemission

The advances of pulsed tunable laser sources facilitated an additional possibility of accessing unoccupied states below the vacuum level. First two-photon-photoemission exper-

iments on metal surfaces [40] three decades ago promised a wide applicability of pulsed laser sources in photoemission spectroscopy. Today, 2PPE is a powerful tool not only as an alternative to inverse photoemission spectroscopy but also for unravelling electron dynamics at surfaces. Here, the elementary processes of 2PPE, basic considerations of electron dynamics at surfaces and the method of time-resolved 2PPE (TR-2PPE) are briefly discussed.

The elementary processes in 2PPE are introduced by using the qualitative considerations outlined in Ref. [41]. Fig. 2.12 illustrates the possible excitation pathways leading to the final photoelectron states. This schematic energy diagram consists of a bulk continuum with a localized surface state $|i\rangle$ below the Fermi energy E_F, an unoccupied image potential state $|j\rangle$ between E_F and the vacuum level E_{vac} and a final state $|p\rangle$ above E_{vac}. The two-photon excitation is carried out by providing pump and probe photons of energy $\hbar\omega_{pu}$ and $\hbar\omega_{pr}$, respectively, under the conditions

$$\hbar\omega_{pu} < \Phi \quad \text{and} \quad \hbar\omega_{pu} + \hbar\omega_{pr} > \Phi. \tag{2.20}$$

Considering a coherent two-photon excitation without any losses due to momentum mismatches $k_{\parallel} = 0$, the energy conservation can be written as

$$E_p = E_i + \hbar\omega_{pu} + \hbar\omega_{pr}. \tag{2.21}$$

In principle, the two-photon photo-excitation can be subdivided into a step-by-step one-photon process (a) and a direct two-photon ionization process (b). In the case of the incoherent step-by-step process, an intermediate state $|p\rangle$ is populated by an electron from $|i\rangle$ after absorbing the energy of the pump photon $\hbar\omega_{pu}$. Subsequently, this electron is excited by a probe photon with energy $\hbar\omega_{pr}$ into the final state $|p\rangle$. Moreover, the intermediate state does not have to coercively be populated by electrons from $|i\rangle$, also indirect excitations $k_{\parallel} \neq 0$ from the bulk continuum can occur, followed by intraband relaxation, leading to a population at $k_{\parallel} = 0$. The other pathway leading to the final state $|p\rangle$ is the direct two-photon ionization process in which the electron absorbs pump and probe photon coherently.

Before discussing the method of time-resolved two-photon photoemission (TR-2PPE), the chronology of the electronic responses in a metal to an external electromagnetic perturbation, shown in Fig. 2.13, are briefly summarized from Refs. [42–44]. As a fundamental response, the collectively excited conduction band electrons try to screen the external field. This dynamical screening proceeds on sub-femtosecond time scales in metals. Most of the energy carried by an external field is reflected; however, due to the decoherence of the collectively excited conduction electrons by elastic and inelastic processes a small fraction of the energy can be absorbed, possibly leading to an excitation into an intermediate state. Further scattering of these excited electron-hole pairs generates a hot-electron (hot-hole) distribution within a time scale of < 10 fs. This non-equilibrium system thermalizes through electron-electron scattering in the next hundreds of femtoseconds, until, finally, energy is transferred to phonons.

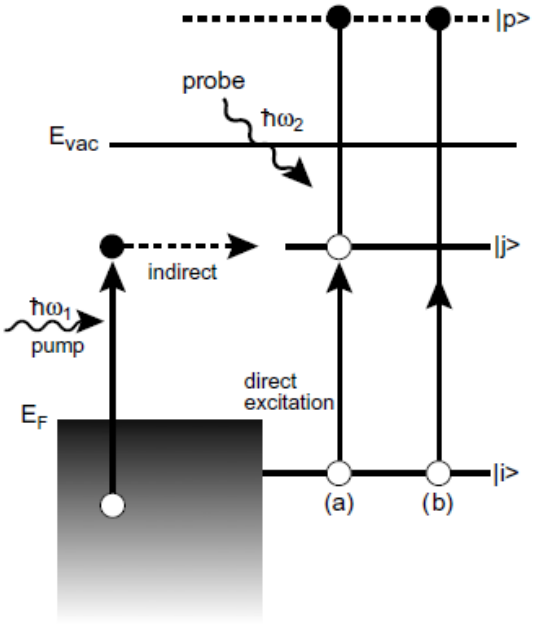

Figure 2.12: Elementary excitation processes in two-photon photoemission. (a) The step-by-step one-photon process: An electron is excited by pump photon $\hbar\omega_{pu}$ either directly from surface state $|i\rangle$ or indirectly from the bulk continuum and following scattering processes into an intermediated image potential state $|j\rangle$. Probe photon $\hbar\omega_{pr}$ facilitates then the transition into the final state $|p\rangle$ above the vacuum level. (b) Direct two-photon two-photon ionization process from $|i\rangle$ to $|p\rangle$. [41]

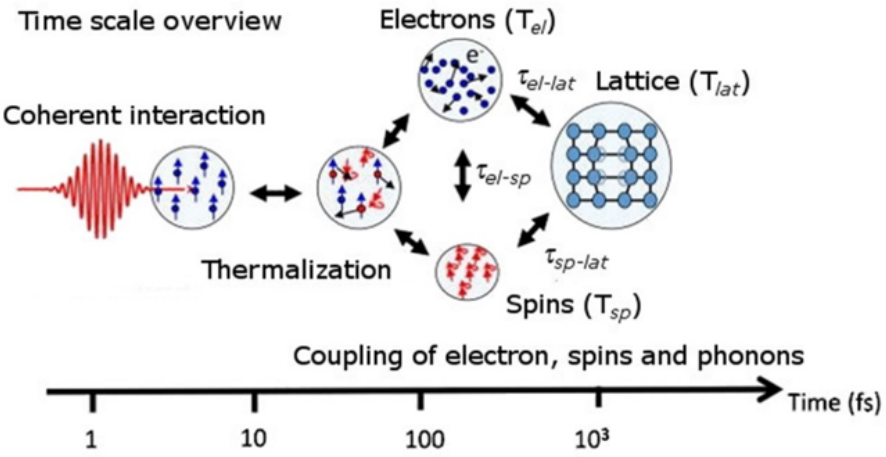

Figure 2.13: Overview of the time scales of laser driven excitation and relaxation processes. [45]

An experimental investigation of these dephasing rates or decaying processes requires time-resolved measurements enabled by laser systems with ultrafast pump and probe pulses. A controllable time delay between pump and probe pulses can be established by

introducing an interferometric set-up. By overlapping two laser pulses collinearly on the sample, photoelectrons can be recorded as a function of pump-probe delay.

Considering the energy diagram in Fig. 2.12, a first photon creates a population of electrons in the intermediate state $|j\rangle$. From this hot electron state a time-delayed second photon drives then the photoemission. The relevant relationship governing the physics of TR-2PPE can be expressed by the finite relaxation (decaying) time T_1 of the intermediate state, the dephasing time T_2 and the pulse duration t_p of pump and probe photons. By recording the photoemission signal at the corresponding energy of the intermediate state $|j\rangle$ in dependence of the time delay t_d, the so-called cross-correlation trace can be acquired. For $T_1 \gg t_p$ the lifetime can be directly determined by fitting the decaying tail of the cross-correlation trace at longer positive t_d. If T_1 is comparable or shorter than t_p the cross correlation trace has to be deduced by fitting, using proper starting values for T_1 and T_2 because the decay cannot be separated in time from the pump-probe cross-correlation reference. In the case of $T_1 \ll t_p$, the photoemission signal is equivalent to the pump-probe cross-correlation. [46]

Chapter 3

Experimental Setup

In 2005 Escher et al. [1] introduced a novel instrument for imaging the photoelectron distribution driven by the worldwide advance in nanoscience and the dramatic progress in the field of spectroscopy and microscopy. They combined a photoemission electron microscope with a tandem arrangement of two hemispherical energy analysers in order to establish electron spectroscopy for chemical analysis (ESCA) with lateral resolution in the nanometer regime. However, the photoelectrons which are analysed and detected by the microscope have to be generated in the first place. Therefore, an equally important part in the photoemission experiment has to be attributed to the light source. By using a variety of light sources, different electronic states and processes can be accessed. Classical photoemission spectroscopy configurations are usually equipped with X-ray sources and vacuum ultraviolet (VUV) sources for studying core level and valence states. Since the photon energy has to be higher than the material's work function, mercury discharge lamps evolved into the workhorse in UV-PEEM for many decades [31]. The strong interest in time-resolved studies led to utilization of pulsed laser sources at the expense of spatial and energy resolution due to space charge effects. Hence, high repetition rates and low intensities per pulse are essential in order to maintain the desired resolution. Furthermore, in terms of lateral resolution, CW lasers surpasses pulsed laser sources with the drawback of no time resolution as long as the photoemission process is linear, which can be achieved by reducing the work function with Cs deposition. [31]
Consequently, this chapter should give an overview, on the one hand, of the NanoESCA instrument, such as the electron optics, the imaging double energy analyser (IDEA), the detection units and the working principle. On the other hand, the light sources used in this master's thesis, such as the helium discharge lamp, the nanosecond laser system Indigo-S and the ultrafast laser setup for time resolved EF-PEEM measurements will be described.

3.1 Instrumental Aspects of the NanoESCA Microscope

As already mentioned, the so-called NanoESCA, introduced by Escher et al. [1], is a combination of an electrostatic photoemission electron microscope (PEEM) and a twin hemispherical energy analyser (HSA) revealing a relatively good energy resolution with an adequate lateral resolution. Fig. 3.1 shows a schematic layout of the NanoESCA instrument. As indicated, it can generally be distinguished between three modes of operation: (1) the direct non-energy filtered PEEM mode, (2) the spectroscopy mode for recording

photoemission spectra from selected areas and (3) the energy filtered imaging mode for

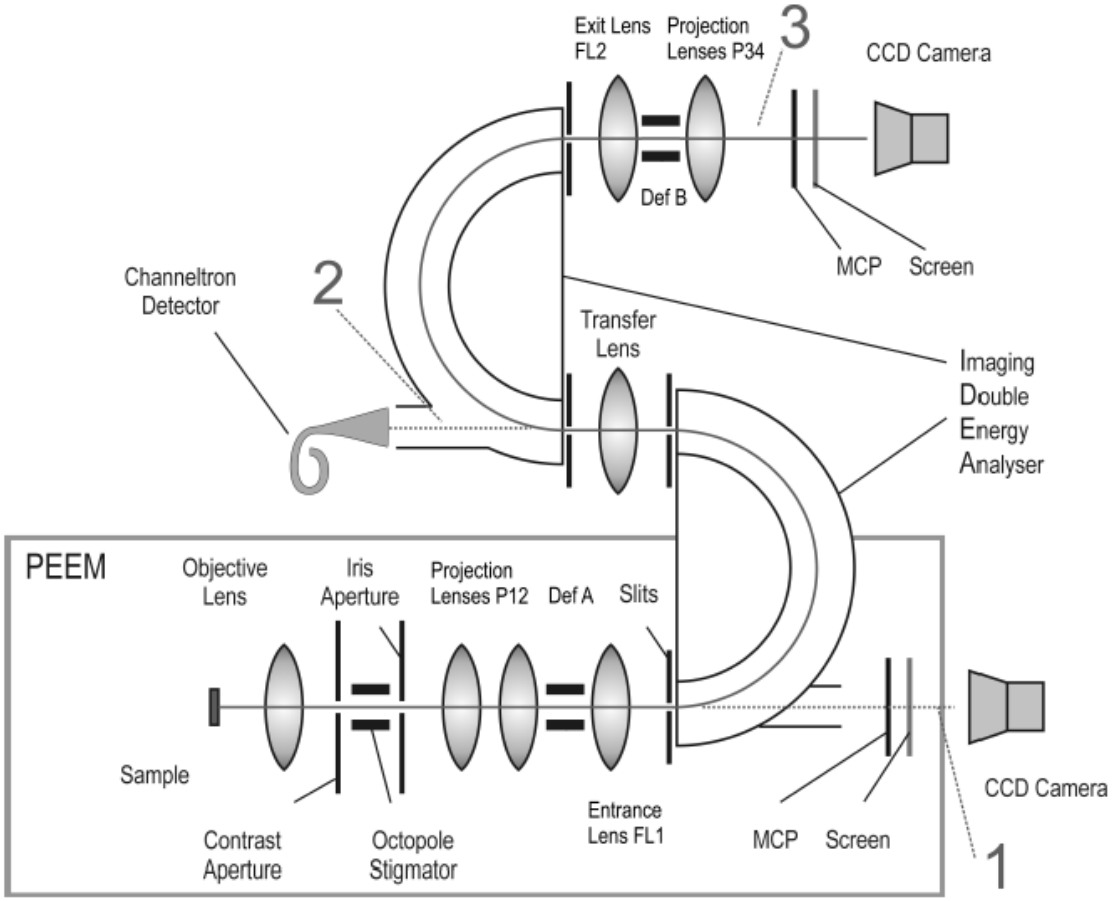

Figure 3.1: Schematic layout of the NanoESCA instrument. In principle, there are three operating modes: (1) PEEM mode, (2) spectroscopy mode and (3) energy filtered imaging mode. [1]

real and k-space imaging. In this section, the most relevant components of the instrument such as the electron optics, the imaging double energy analyser (IDEA) and the detection modes are discussed. For further information the reader is referred to refs. [1–3, 5, 47].

3.1.1 Electron Optics

In principle, the electron optics can be subdivided into the objective lens configuration, the projection column and the IDEA coupling lenses.

As in any microscope, the objective serves as the imaging and magnifying unit. In the case of the NanoESCA instrument, the objective lens is a tetrode consisting of four elements, namely the sample, the extractor, the focus and the column electrode. Between the sample and the extractor a strong electric field is applied, which draws photoelectrons into the microscope column. While usually the column electrode voltage U_{COL} is kept fixed, the focus voltage U_{FOC} is used to control the focal point of the objective. A first

intermediate image is generated at the position of the iris aperture, which can be closed to select a defined area of the photoelectron distribution. For maximum resolution and high magnification high extractor voltages U_{EXT} and a ratio of $U_{EXT}/U_{COL} = 12$ are recommended [2]. With the recommended settings, magnification factors of $M_{obj} = 35 - 40$ [2] are possible. Note that these stated values and ratios depend also on the sample distance, as shown in ref. [2]. Furthermore, applying such high extractor voltages can produce high leak currents which can strongly influence the image acquisition. If the leak current oscillates violently (~ 10 μA) the multichannel plate (MCP) can be damaged. This has to be considered when choosing the extractor voltage. Furthermore, the potential between extractor and sample also bends the trajectories of the photoelectrons towards the optical axis of the microscope. This leads to a reduction of the angular photoelectron spread and, further, to a reduction of the aberration of the electron optics. Consequently, the resolution of the microscope is improved. An additional limit of the angular photoelectron distribution can be set by the contrast aperture (CA), which is located in the back focal plane of the objective lens. This results in a further improvement of the spatial resolution but also in a reduction of the transmission. For a specific contrast aperture, the maximum starting angle of the photoelectrons originating from the sample can be calculated as

$$\alpha_{0,max} = \arcsin\left(\frac{r_{CA}M}{l_{CA-Iris}} \cdot \sqrt{\frac{E_i}{E_0}}\right) \tag{3.1}$$

with r_{CA} as the radius of the contrast aperture, M as the magnification at the iris aperture, $l_{CA-Iris}$ as the distance between contrast and iris aperture, $E_0 \approx eU_{EXT}$ as the starting electron energy and E_i as the electron energy at the image plane ($E_0 + eU_{COL}$). However, the entrance slit of the energy analysers and its pass energy, which are not considered in Eq. 3.1, finally determine the acceptable angular phase space. For most of the standard settings the contrast aperture serves as the restricting element, but in the case of small entrance slits and small pass energies together with a large contrast aperture the situation is contrary [5].

Between contrast and iris aperture a first deflector/stigmator unit, realized by an electrostatic octupole, is installed to compensate for imperfections, such as misalignments of the optical axis and axial astigmatisms, introduced by the objective lens. The deflector (V_x and V_y) is used to align the the optical axis of the objective lens with that of the following projection lenses. Remaining astigmatisms can then be corrected by the stigmator which is subdivided into two parts: The x/y stigmator (S_x), whose axes are those of the deflector and the xy/-xy stigmator (S_y), whose axes are tilted 45° to the deflector axes. By wobbling the focus voltage, both imperfections can be compensated for by following an iterative procedure given by the manuals [2, 3].

The projection column is subdivided into two projection elements. In the energy filtered mode, the first projection lenses P12 behind the objective are used to retard the electrons towards the analyser's pass energy E_{pass} and to project the first intermediated image onto the entrance plane of the IDEA, whereas in the direct PEEM mode, P12 projects and magnifies the final image onto the imaging unit. The second projection element P34 placed behind IDEA images the energy filtered electrons onto the second imaging unit. Combining the magnification factors of the objective and the projection

column gives a total magnification of about 4000 [5] in both modes.

The last unit of electron optics is covered by the IDEA coupling lenses consisting of two Fourier lenses at the entrance and the exit of the hemispheres. The first Fourier lens FL1 forms a reciprocal image at the entrance slit. Additionally, a deflector DEF A is located in front of the Fourier lens in order to optimize the position of the electron bundle in the entrance slit of the IDEA. At the exit of the second hemisphere a Fourier lens FL2 transforms the reciprocal image back and a deflector DEF B aligns the electron beam towards the optical axis of the projective lenses P34. Between the first and second hemisphere of the IDEA a transfer lens either images the electrons leaving the first hemisphere onto the entrance of the second hemisphere or focuses the electrons into the channeltron detector for selected area spectroscopy. Furthermore, this transfer lens can also correct defocussed images, uniaxial distortions and energy dependent image shifts. [3]

The spatial and momentum resolution of the NanoESCA microscope is primarily determined by spherical and chromatic aberrations of the objective lens and the size of the contrast aperture due to diffraction. Although these factors can be optimized by appropriate instrumental settings, in the end, the resolution is intrinsically restricted by the used lenses. By introducing additional electron mirrors [48, 49] aberrations can be reduced, leading to a spatial resolution of less than 10 nm. However, the NanoESCA microscope is specified for 40 nm resolution without any additional aberration correcting elements. A detailed description together with a calculation of the spatial resolution is outlined in Ref. [5].

3.1.2 The Imaging Double Energy Analyser (IDEA)

The analyser of the NanoESCA is the so-called imaging double energy analyser (IDEA) introduced as a new development by Escher *et al.* [1] in 2005. It consists of two electrostatic hemispherical sector analyser. The first hemisphere separates the photoelectrons by their kinetic energy, whereas the second hemisphere compensates the dispersive imaging errors of the first hemisphere in order to avoid chromatic aberrations in the PEEM image. A schematic illustration of the IDEA with representative electron trajectories are depicted in Fig. 3.2(a).

As already described above, the photoelectrons accelerated by the objective lens configuration are retarded by the projection column towards the analyser's pass energy E_{pass}. While scanning through the kinetic energies of the photoelectrons by varying the sample voltage U_{SPL}, E_{pass} is kept constant. This results in a fixed energy resolution ΔE, which can be expressed as follows

$$\Delta E = E_{pass} \cdot \left(\frac{d}{2R_0} + \alpha^2 \right) \tag{3.2}$$

with d as the entrance slit width, R_0 as the mean radius of the hemispheres and α as the maximum angle of the electron with respect to the optical axis (see Fig. 3.2(b)) representing the spherical aberration of the analyser's dispersion. If the α^2-term is small enough the energy resolution can be improved either by a small pass energy or a small

slit width. Typical operating parameters (E_{pass} and d) for different light sources can be found in ref. [3].

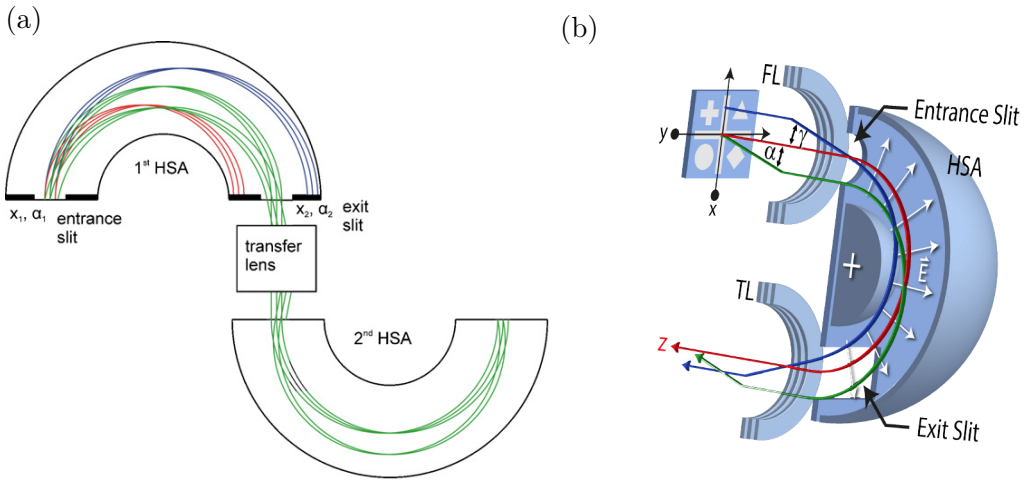

Figure 3.2: (a) Scheme of the Imaging Double Energy Analyser (IDEA) showing the two hemispheres and electron trajectories. [47] (b) Sketch of the first half of the NanoESCA energy filter system. [5]

Although the second hemisphere tries to neutralize the dispersive imaging errors of the first hemisphere, a non-isochromaticity of the EF-PEEM images is introduced, which means that different points in the image represent photoelectrons with different kinetic energies. This energy shift causes a change in intensity, which can be corrected by post data evaluation of an energy filtered image stack.

3.1.3 Detection Units

The NanoESCA provides two detection systems, the channeltron and the image detection. The former is used for single electron counting in the spectroscopy mode, the latter for detecting the two dimensional photoelectron distribution in the PEEM modes. In this subsection, the assembly and the working principle of these detection devices are briefly discussed.

Considering a schematic of a channeltron, as shown in Fig. 3.3, photoelectrons (primary electrons) coming from the microscope column and the first hemispherical analyser strike the inside wall of the channeltron and generate secondary electrons, which are accelerated through the channel, producing additional electrons progressively towards the output. The amount of counted electrons is linear proportional to the amount of the incoming electrons, which allows for a quantitative analysis [5]. By selecting a region of interest on the sample with the image detector and the iris aperture, the channeltron detection can be used for quasi spatial resolved measurements. Note that the iris aperture can not be closed symmetrically due to its construction. Furthermore, the operating plateau voltage can not be changed manually, consequently, the total amount of counts

can only be decreased by lowering the selected area via the iris aperture or by lowering the intensity of the light source. As in any measurement technique relying on counting statistics, the channeltron detection also exhibits a dead time (approx. $\tau = 100$ ns), representing the time after each counting event during which the system is not able to record another event. The true number N_{true} of electrons entering the channeltron can be expressed as

$$N_{true} = \frac{N_{obs}}{1 - N_{obs}\tau} \tag{3.3}$$

with N_{obs} as the observed count rate.

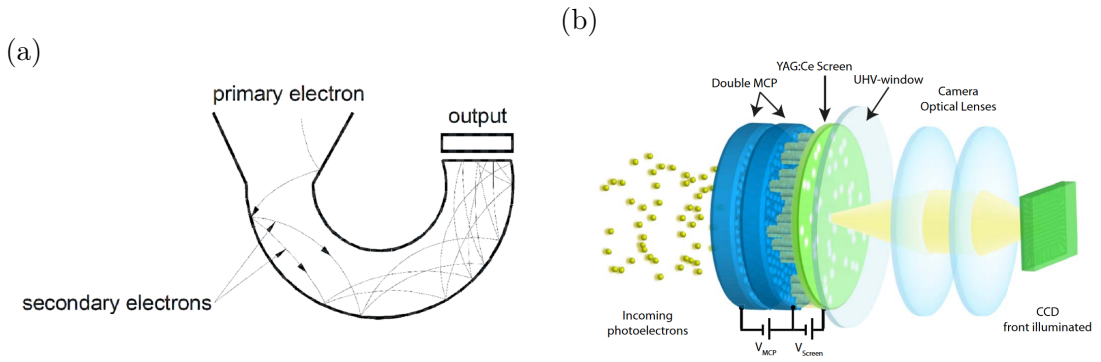

Figure 3.3: (a) Schematic of a channeltron and its working principle. [3] (b) Schematic of the imaging unit consisting of a double microchannel plate, a YAG:Ce screen and digital-fast-acquisition camera. [50]

The imaging unit basically consists of a microchannel plate (MCP) and a fluorescent screen (SCR), as depicted in Fig. 3.3(b). A microchannel plate is an array of hexagonally packed miniature electron multipliers. After leaving the microscope column and the energy-filter, the photoelectrons are projected by the projective columns onto the MCP, which multiplies single electrons to electron bundles. The amplification can be regulated by the MCP voltage. Note that the lifetime of the MCP can significantly be lowered by applying excessively high voltages. Hence, the saturation region indicated by the appearance of bright spots should be avoided and the applied voltage should always be as low as possible. The electron bunches are then accelerated towards a fluorescent screen where Gaussian shaped light signals are generated. In regular operation the voltage between the MCP and the screen is kept constant. The produced light signal is further directed through a tandem objective and focused onto a camera with a charged couple device (CCD).

3.1.4 Principles of Operation

In this subsection the principles of operation for spectroscopy, photoemission microscopy and momentum microscopy are briefly discussed.

Considering a photoemission experiment with an x-ray source (energy $h\nu$), electrons are ejected from core level states with different binding energies E_{bin}, leading to an energy

distribution of photoemitted electrons by analysing their kinetic energies E_{kin}. The corresponding energy relation can be expressed as

$$E_{kin} = h\nu - E_{bin} - \Phi_S \tag{3.4}$$

with Φ_S as the work function of the sample. The true kinetic energy scale, however, can not be measured directly because Φ_S, which varies from sample to sample, is not known. Therefore, the NanoESCA software measures the energy with respect to the Fermi level $E - E_F$, which can be determined by calibrating the analyser work function Φ_a performing an experiment with known photon energy $h\nu$ and measuring the position of the Fermi cut-off. [3] The corresponding energy relation can be expressed as

$$E - E_F = E_{kin} + \Phi_S \tag{3.5}$$

An energy scheme of a photoemission experiment is depicted in Fig. 3.4, emphasizing the energy relation between E_{kin} and $E - E_F$.

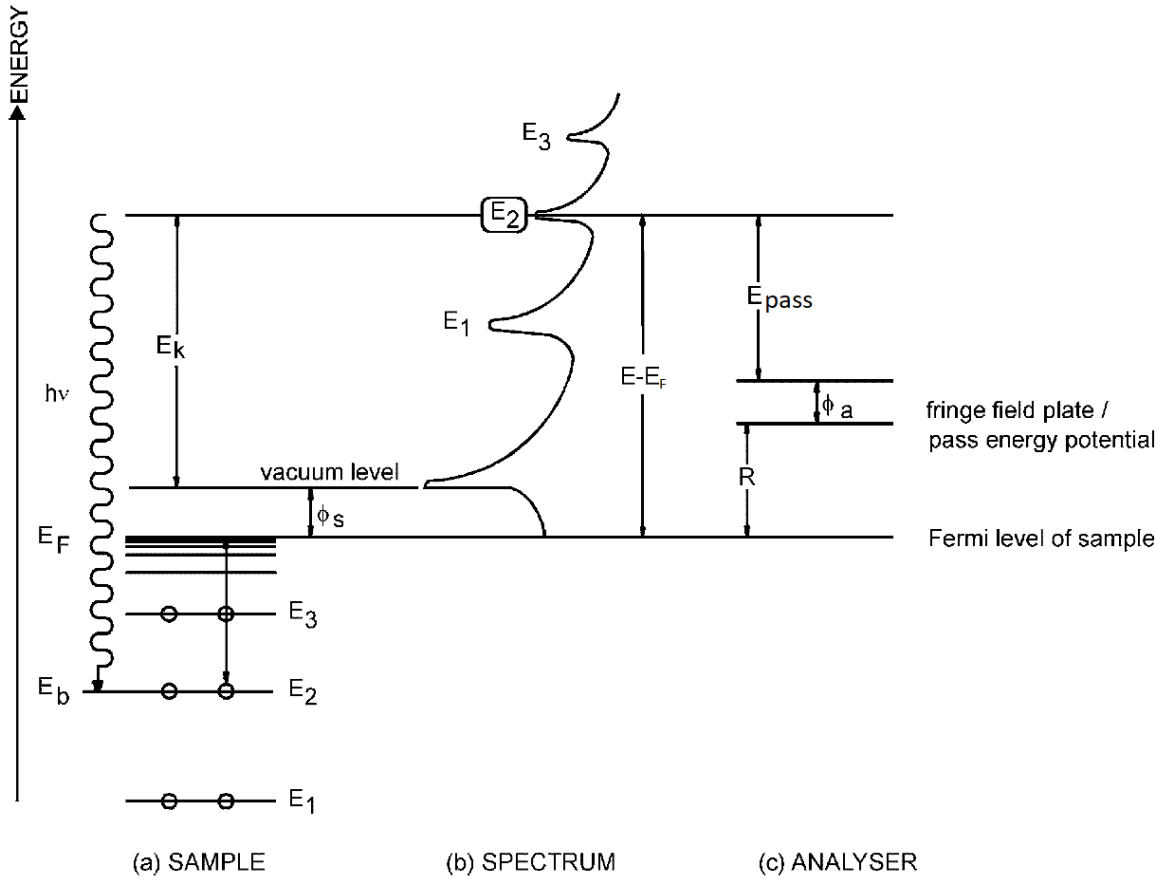

Figure 3.4: Energy scheme of a photoemeission experiment with x-ray radiation. Electrons are ejected from core level states with different binding energies, which can be determined from the photoemission spectrum, the corresponding kinetic energies and the work function of the sample. [3]

As already mentioned in chapter 2, the photoemission exhibits the following characteristics: The low energy cut off at $E - E_F = \Phi_S$, a large peak at low kinetic energy due to

the true secondary electrons, peaks corresponding to the discrete core level states and the Fermi edge at $E - E_F = h\nu$. In the case of the NanoESCA, photoelectrons are accelerated by the objective lens configuration at first and then retarded by the projective column towards the pass energy E_{pass}. The analyser works as a band pass filter, only transmitting electrons very near to the pass energy. An electron with a specific kinetic energy will only pass the analyser if it is overall accelerated or decelerated by an amount of R towards the pass energy E_{pass}. In order to set R correctly for a specific kinetic energy the sample voltage can be varied. Considering also the analyser work function Φ_A, the energy relative to the Fermi level of the transmitted electrons can be written as

$$E - E_F = R + E_{pass} + \Phi_A = h\nu - E_{bin} \tag{3.6}$$

which is independent of the sample work function Φ_S.

As already mentioned above, by changing the settings in the objective lens configuration and the projection column the microscope can either acquire a spatially resolved image of the sample while integrating over all emission angles in each point (real-space microscopy) or map the momentum (angular) distribution while integrating over the selected sample area (momentum microscopy). A good overview of the different lens settings and the corresponding electron trajectories taken from ref. [5] is depicted in Fig. 3.5.

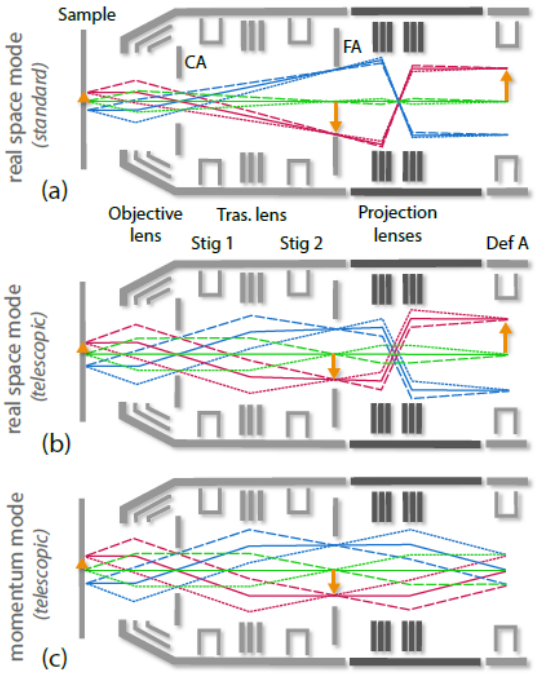

Figure 3.5: The three main operating modes of the NanoESCA: standard real space, telescopic real space and momentum space. [5]

For the standard imaging mode (a), a first intermediate image of the spatial photoelectron distribution is created by the objective lens in the position of the field (iris) aperture (FA), which can limit the spatial field of view, whereas the contrast aperture (CA) located in the

back focal plane of the objective can limit the angular phase space. The first intermediate image is then transferred by the projection column onto the second intermediate image. In order to image the angular photoelectron distribution a transfer lens is used behind the objective, c.f. (c). At the first intermediate image plane a telescopic image is created, i.e. the correct angular distribution is maintained in all image points because the objective lens is focused to infinity and the transfer lens forms an intermediate image in the iris aperture. The telescopic image is then mapped onto the second intermediate image plane. Here, the projection column serves as a Fourier lens, converting the real space telescopic image into a momentum image. For real space mode (b), the telescopic image can also be projected as a real space image, facilitating an easy switching between real and k-space imaging. The disadvantages of using the transfer lens in real space mode are the lower magnification of the objective lens and a worse resolution due to spherical aberration effects caused by a broader angular spread [3, 5].

3.2 Light Sources

On the one hand, analysing and detecting photoelectrons is an essential part in photoemission experiments, however, on the other hand, generating the photoelectrons plays an equally important role. By using a variety of light sources, different electronic states and processes can be accessed. For instance, x-ray radiation can unveil the elemental composition and the chemical environment by interpreting the core level states, ultraviolet light gives information about the valence bands and, furthermore, ultrafast laser pulses allow for time-resolved measurements. Strictly speaking, the employed light source determines the type of photoemission experiment. In this section the relevant features of the sources used in the course of this thesis, encompassing the helium discharge lamp, the nanosecond and femtosecond laser systems are described.

3.2.1 The Helium Discharge Lamp

In order to investigate the valence bands in photoemission experiments photon energies of about 10 to 100 eV are needed. Due to the insufficient transmission of optical elements in this wavelength regime, the photon source has to be directly connected to the UHV chamber. Hence, this photon energy regime is also called vacuum ultraviolet regime (VUV). Such photon energies are commonly produced by gas discharge lamps in which an inert gas is excited and partially ionized. In the case of helium, the electronic transition from the 2p into the 1s state of the excited atom (He I) or the ion (He II) generates monochromatic UV-light (He I: 21.21 eV; He II: 40.81 eV).

The high intensity VUV source mounted at the NanoESCA is a cold cathode capillary discharge lamp [51,52], the so-called HIS 13 [53]. The schematic layout of the VUV source is depicted in Fig. 3.6. The VUV source can, in principal, be subdivided into the gas inlet, lamp body, differential pumping stages and the light capillary. The operation and ignition pressure of the discharge gas can be controlled by a leak valve. In order to reduce the partial pressure of the discharge gas in the main chamber, the VUV source is differentially pumped by two pumping stages. The first pumping stage consists of an oilfree scroll pump to avoid oil back streaming and a Pirani gauge for maintaining the right

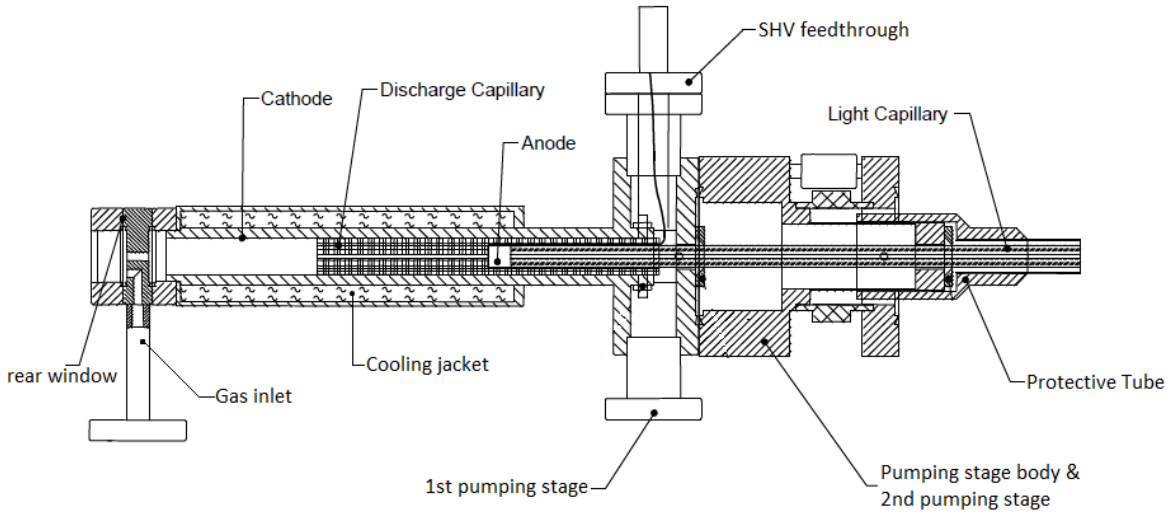

Figure 3.6: Schematic layout of the VUV source HIS 13. Modified from ref. [53]

pressure regime of the discharge gas. The second differential pumping stage incorporates a small turbo molecular pump (60 l/s) backed by a rotary vene roughing pump to improve the vacuum in the analysis chamber. After filling the lamp body with gas at the desired pressure (approx. $5 \cdot 10^{-2} - 5 \cdot 10^{-1}$ mbar [53]) an ignition potential (700 V) can be applied to the anode and cathode. Short high voltage pulses in regular intervals try to start the discharge. If the gas ignites, a continuous discharge will be maintained by an operating discharge voltage and current, typically 450 V and 100 mA for HeI at $6 \cdot 10^{-2}$ mbar. In order to allow for high discharge currents and to reduce electrode degradation the lamp is additionally water cooled.

By adjusting the gas pressure and the discharge current the nature and the intensity of the radiation can be influenced and two modes of operation can be accessed with the right settings [51]: Lines of neutral atoms (e.g. HeI etc.), a quasi-continuum of diatomics and lines of singly charged ions (e.g. HeII) and also lines of dissociated diatomics. According to the manual [53] the optimum operational pressure of the VUV source has to be determined experimentally by slowly passing through the relevant pressure range and displaying the total electron count rate. Note that when operating with one optimized resonant line there is always some radiation with low intensity originating from the other line.

The performance and the characteristics of the VUV source, such as the spot diameter, the photon intensity and the chamber pressure, are strongly influenced by the dimensions of the light capillary. The spot size depends on the inner diameter of the light capillary and the working distance. Furthermore, the spot profile slightly varies for different photon energies, e.g. the spot profile of He I, as shown in Fig. 3.7, exhibits shoulders besides the geometrically expected beam profile due to multiple reflections inside the light capillary, whereas for higher photon energies (e.g. He II) these reflections are more suppressed.

The photon intensity also depends on the cross section of the inner diameter and the

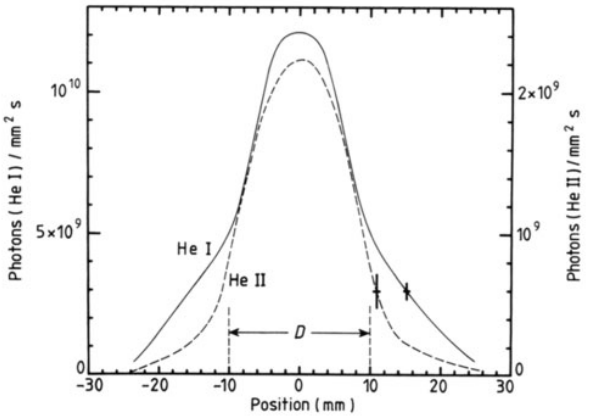

Figure 3.7: Spatial beam profiles for He I (left ordinate) and He II (right ordinate) resonance radiation. The widths of the spot profiles at half maximum show good aggreement with the geometrical diameter of the light capillary. Due to scattering events in the lamp, the profiles deviate from a Gaussian, depending on the energy. [52]

length of the capillary. A longer light capillary gives a slightly reduced intensity. The dimensions of the light capillary also effect the pressure of the analysis chamber, besides the pumping system. Hence, the background pressure in the analysis chamber increases with the capillary cross-section and decreases with capillary length. [52, 53]

3.2.2 The Nanosecond Pulsed Ti:Sapphire Laser

Within the scope of this thesis it was also planned to investigate the applicability of different laser systems for photoemission experiments. The Indigo-S laser system, an all-solid-state pulsed laser, revealed, therefore, as a reliable and quickly accessible light source for 2PPE, capable of producing narrow linewidth laser light in the near infrared, the blue and the ultraviolet wavelength regime at repetition rates of 5 kHz. In principle, the laser system incorporates the Coherent Evolution-15 pump laser, a Ti:sapphire oscillator, a harmonics package for second and third harmonic generation, a controlling unit and a closed loop chiller. In this subsection, the relevant components and the main characterisitcs of the laser system are briefly discussed based on refs. [54–56].

The optical layout of the Evolution-15 pump laser is depicted in Fig. 3.8. An array of twelve AlGaAs laser diodes pumps a Nd:YLF crystal, which emits light at a wavelength of about 1053 nm. In order to produce a pulsed laser beam, Q-switching is applied. By keeping artificially the resonator losses high, a higher population inversion can be generated. Hence, more energy can be stored in the active medium, which can be liberated in a more powerful laser pulse if the quality(Q)-factor of the resonator is abruptly increased. In the case of the Evolution-15 laser, this Q-switching is realized by two acousto-optic modulators, which deflect the laser beam when applying a radio-frequency due to their piezoelectric properties. If the radio-frequency source is turned off, the laser pulses can pass the acousto-optic modulators unperturbed. In order to ensure efficient pumping of the Ti:sapphire crystal the Nd:YLF laser has to be frequency-doubled, which is achieved

by a LBO crystal mounted in a crystal oven housing, maintaining temperature of 340°F. A dichroic mirror serves as an output coupler for laser pulses at 527 nm.

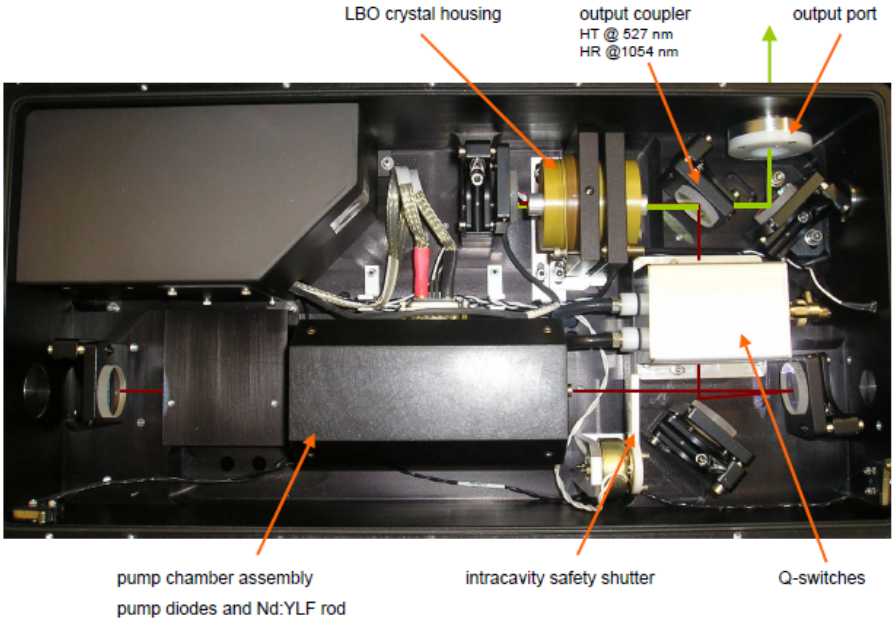

Figure 3.8: Optical layout of the Evolution-15. Laser diodes pump a Nd:YLF crystal emitting light at a wavelength of around 1053 nm (indicated by the dark-red line). Q-switches produce nanosecond pulses, which are then frequency-doubled by an LBO crystal. The second harmonic of the Nd:YLF laser (indicated by the green line) leaves the laser bench via an output coupler and serves as the pumping light for the Ti:sapphire laser (see Fig. 3.9). Taken from Ref. [54]

The optical layout of the Indigo-S Ti:sapphire oscillator is shown in Fig. 3.9. The second harmonic of the pulsed Nd:YLF pump laser is initially expanded by a set of two lenses, folded by two mirrors and then focused into the Ti:sapphire rod. Due to the excess heat from the pumping process the Ti:sapphire rod assembly is water cooled. Besides the high-reflective (HR), plane-parallel rear cavity mirror and the partially reflective plane-parallel output coupler, the Ti:sapphire resonator comprises an intracavity high-dispersion prism for wavelength selection and an etalon for suppressing closely spaced modes. A motorized tuning of the wavelength is established by piezo actuators attached to the rear cavity mirror and the etalon. Furthermore, a spectrometer mounted to an optical fiber analyses the wavelength of scattered laser light. By using four sets of HR mirrors and etalons a desired output wavelength can be chosen between the 750-850 nm or the 840-930 nm regimes.

Before describing the optical components of the harmonic package, a brief consideration about non-linear optics and harmonics generation should not be omitted in this context. Considering the interaction of an electromagnetic wave with matter, the corresponding electric field $\mathbf{E} = \mathbf{E_0}\cos(\omega t)$ causes a displacement of the bound electrons resulting in dipole moments. The density of the induced dipole moments per unit volume is defined

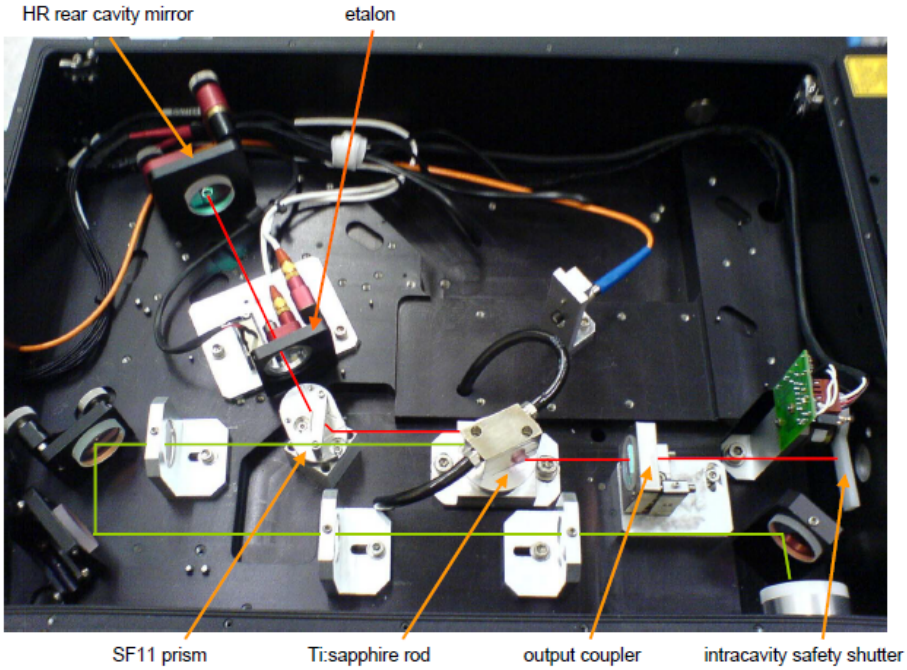

Figure 3.9: Optical layout of the Ti:sapphire oscillator. The second harmonic of the pulsed Nd:YLF (indicated by the green line) pumps the Ti:sapphire crystal after passing a sequence of lenses and mirrors. By using an intracavity high-dispersion prism, a motorized high-reflective, plane-parallel rear cavity mirror and an etalon an output wavelength can be set between 750-920 nm (indicated by the red line). Taken from Ref. [54]

by the dielectric polarization $\mathbf{P}(\mathbf{E})$, which can be expressed as

$$\mathbf{P}(\mathbf{E}) = \epsilon_0 \left[\chi^{(1)}\mathbf{E} + \chi^{(2)}\mathbf{E}^2 + \chi^{(3)}\mathbf{E}^3 + ...\right], \tag{3.7}$$

where the susceptibility χ describes the polarization ability of the material. When dealing with very intense electric fields, higher-order terms beyond the linear component have to be taken into account. For second harmonic generation, the second order term can be written as

$$\mathbf{P}^{(2)}(\omega) = \epsilon_0 \chi^{(2)} {\mathbf{E_0}}^2 \cos^2(\omega t) \tag{3.8}$$

$$= \frac{1}{2}\epsilon_0 \chi^{(2)} {\mathbf{E_0}}^2 \left[1 + \cos^2(2\omega t)\right]. \tag{3.9}$$

This can be interpreted as a frequency-independent polarization term plus a component at twice the frequency of the incoming radiation. However, for successful generation of the second harmonic the phase-matching condition has to be fulfilled implying that the microscopic waves created at different positions in the medium have to be in phase in order to overlap. Consequently, the phase velocity of the incident wave and the generated waves has to coincide. The phase-matching condition is also consistent with the conservation of momentum of the engaged photons:

$$\mathbf{k}(2\omega) = 2\mathbf{k}(\omega) \tag{3.10}$$

in terms of wavevectors or in terms of the refractive index

$$n(2\omega) = n(\omega). \tag{3.11}$$

By using an anisotropic, thus birefringent, material at the correct angle of incidence the phase-matching condition can be fulfilled.
The optical layout of the production and extraction of the second harmonic is depicted in Fig. 3.10. Following the beam path, by a sequence of mirrors and a focusing lens the horizontally polarized (s-polarized) output of the Ti:sapphire oscillator is guided to the SHG-crystal. A half-wave plate rotates the polarization into p-polarized light and, in order to meet the phase-matching condition, the SHG-crystal has to be adjusted manually or computer controlled by a piezo actuator. The fundamental and the s-polarized second harmonic are then separated by a dichroic mirror and the second harmonic is extracted from the laser bench. Furthermore, the harmonics package can be extended by packages for third and fourth harmonics generation.

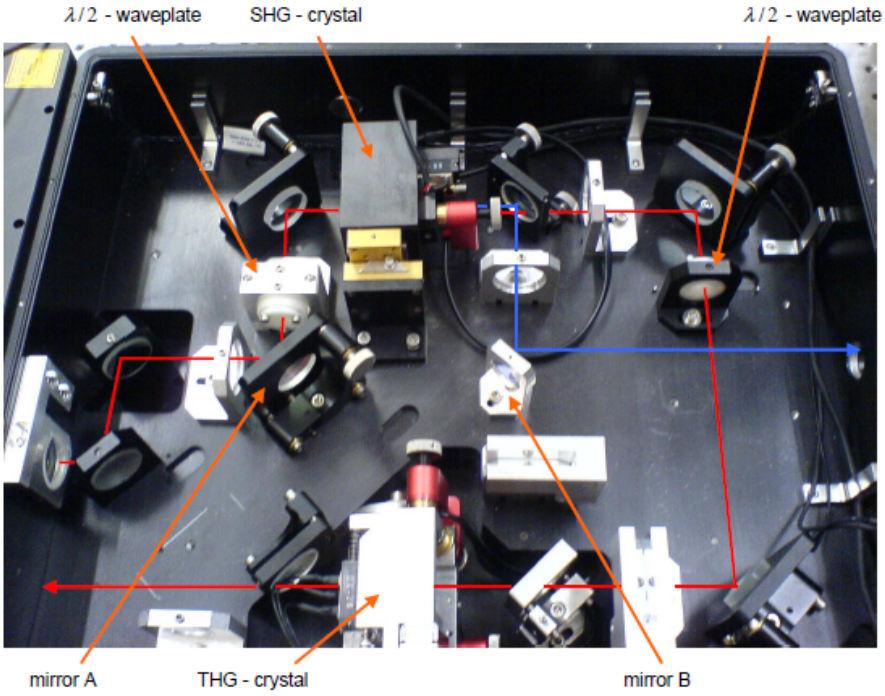

Figure 3.10: Optical layout of the second harmonic generation and extraction of the second harmonic of the Ti:sapphire laser. Via a set of mirrors, a lens, a half-wave plate and the SHG crystal with its adjustable housing the phase-matching condition and an efficient conversion can be achieved. The second harmonic (indicated by the blue line) is then extracted from the laser bench and guided to the EF-PEEM. Taken from Ref. [54]

3.2.3 The Femtosecond Laser Setup

A major part of this thesis has been the implementation of an ultrafast laser setup, paving the way for time-resolved EF-PEEM studies. Femtosecond laser pulses generated by a

modelocked Ti:sapphire oscillator are guided from the neighbouring laboratory to the optical table in the PEEM laboratory. There, a SHG unit and a pump-probe setup have been built for one and two color time-resolved 2PPE measurements. In this subsection the main optical and optomechanic components, such as the Coherent Vitara modelocked Ti:sapphire oscillator [57] and the ultrafast laser setup in the PEEM laboratory, are introduced.

Many techniques have been developed for creating ultrashort pulses. In the case of the Vitara, passive mode locking is performed in form of the optical Kerr effect. A typical cavity design of a self-mode-locked Ti:sapphire laser using the Kerr lens mode-locking process is depicted in Fig. 3.11. By using this classical configuration the mode-locking process is

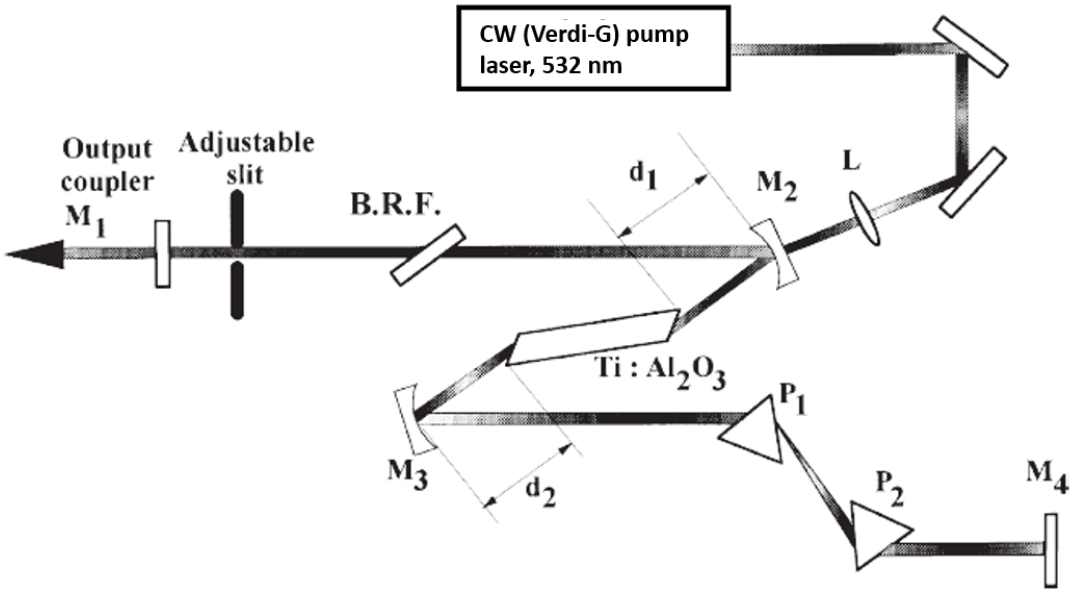

Figure 3.11: A typical cavity design of a self-mode-locked Ti:sapphire laser using the Kerr lens mode-locking process. A cw (Verdi-G) pump laser at 532 nm provides the population inversion in the Ti:Al_2O_3 crystal which emitts light at wavelengths around 800 nm. A bire refringent filter (B.R.F.) serves as an additional wavelength-selective element. The passive-modelocking process is established by the Kerr lens effect in Ti:sapphire crystal and an adjustable slit for a further discrimination between the continuous wave and pulsed modes. A prism compressor compensates the positive chirp generated by the dispersive elements within the cavity. [58]

described based on ref. [57,58]. A cw laser (Verdi-G) at a wavelength of 532 nm pumps a Ti:Al_2O_3 crystal emitting light at wavelengths around 800 nm. Each lasing wavelength or mode has to be an integer number of half wavelengths fitting into the cavity. Beside the restriction determined by the cavity dimensions, a birefringent filter (B.R.F.) serves as an additional wavelength-selective component. Considering several modes lasing simultaneously, they constructively or destructively interfere with each other. Although the laser is operating in a continuous wave (CW) mode within the cavity, at certain points a large number of modes adds together to form an intense pulse. Since the Ti:sapphire crystal is

a non-linear medium and, thus, the refractive index depends on the intensity (Kerr effect): $n = n_1 + n_2 \cdot I$, the amplifying medium behaves like a focusing lens (Kerr lens). This self-focusing process implies that strong intensity maxima of the laser cavity are much more strongly focused than the weaker ones, the CW modes. In order to discriminate further between a continuous and a pulsed regime an adjustable slit is placed inside the cavity. However, for initiating the Kerr lens effect some mechanism has to be introduced to create a sufficiently high peak power. By changing the cavity length at proper speed very high-power fluctuations can be induced which trigger off the process of self-focusing. Furthermore, an additional non-linear process, called self-phase modulation, is introduced due to the strong dependence of the intensity on time $I(t)$ resulting in $n = n_1 + n_2 \cdot I(t)$ and, consequently, in a rapid change of the phase of the wave as a function of time. As a consequence of this self-phase modulation, the spectrum of the wave is broadened leading to a shortening of the pulse duration in the time domain until an equilibrium between the self-phase modulation and the dispersion of the group velocity is reached. In order to keep control of the group velocity inside the cavity a prism compressor is placed in the system. Considering a material with normal dispersion $n(\lambda)$, the group velocity is determined by the slope of the refractive index curve $\frac{dn(\lambda)}{d\lambda}$. The second derivative of the curve, $\frac{d^2n(\lambda)}{d\lambda^2}$, defines the group velocity dispersion governing the rate at which the frequency components of a wave packet change their relative phases. Due to this group velocity dispersion (GVD) a frequency dependent delay of the different spectral components of a pulse, a so-called chirp, is introduced when propagating through a medium. This means that shorter pulses are more susceptible to the effects of dispersion because of their broader range in wavelength. As shown in Fig. 3.11, for compensating the positive chirp caused by dispersive elements within the laser cavity a prism compressor is used. By a proper choice of the prism materials and the distance between the prism a negative chirp can be introduced either to compensate, as already mentioned, the positive chirp originating from the cavity elements, or to provide negative chirp deliberately with respect to dispersive elements outside the oscillator, which would introduce a positive chirp.
The output of the Vitara Ti:sapphire oscillator is specified by a pulse duration of approx. 15 fs, a repetition rate of 80 MHz, a bandwidth of approx. 70 nm and an average power of approx. 325 mW measured in the PEEM laboratory.

The laser setup in the PEEM laboratory is depicted in Fig. 3.12. By using three mirrors, the output of the Vitara oscillator is guided from the neighbouring laboratory to the optical table in the PEEM laboratory. An 1 mm thick window is mounted for compensating the different pressures in the rooms. In order to frequency-double the fundamental of the Vitara a SHG unit is implemented consisting of a half-wave plate, two quartz lenses ($f_1 = 75$ mm and $f_2 = 100$ mm) and a BBO-crystal. The half-wave plate and the SHG-crystal are attached to rotation mounts for fulfilling the phase-matching condition and one of the lenses is placed on a moveable base plate for an efficient light conversion process. The second lens transforms the divergent beam to a parallel one again. A harmonic separator splits the 800 nm and the 400 nm (indicated by the red and blue lines) into different pathways with approximately equal lengths, allowing for one- and two-colour time-resolved energy-filtered PEEM measurements. Considering the blue pathway first, a beam-splitter separates the beam into a static and a moveable branch for introducing a time delay between the pulses. A motorized actuator (LTA-HS [59]), which is controlled

by a single axis motion controller (SMC100 [60]), provides a travel range of 50 mm and a minimum incremental motion of 50 nm, corresponding to 167 as. The delay stage can directly be accessed by the ProNanoESCA software via a Python program which establishes the communication between the ProNanoESCA software and the SMC100 motion controller. By using a second beam-splitter the time-delayed pulses are colinearly overlapped again. Note that this setup corresponds to a classical Michelson-Interferometer. The power of the fundamental is adjusted by a half-wave plate and a thin-film polariser. When photo-exciting with two colours, the static branch of the blue pathway is blocked and instead of a low group delay dispersion mirror a harmonic separator is used to combine the two beams colinearly. With the help of a periscope the laser is coupled into the EF-PEEM. An additional lens ($f_3 = 250$ mm) focuses the ultrafast laser pulses onto the sample under an angle of 24°.

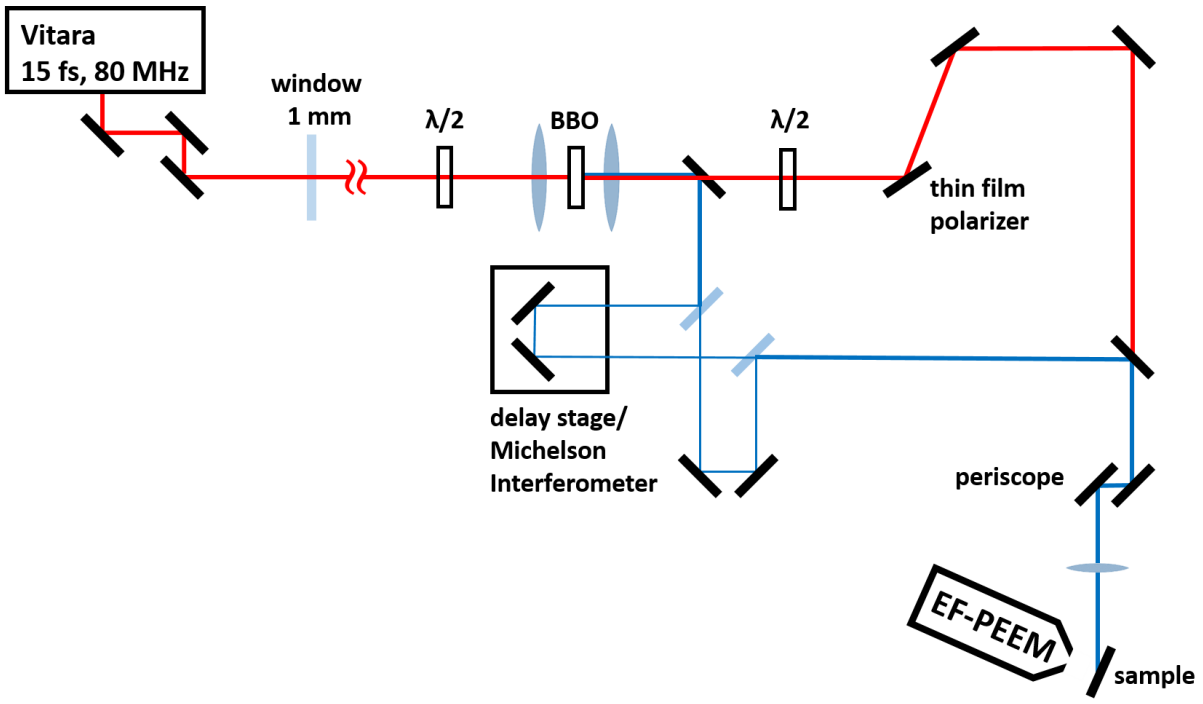

Figure 3.12: The ultrafast laser setup in the PEEM laboratory. The 800 nm output of the Vitara Ti:sapphire oscillator is guided from the neighbouring laboratory to the optical table of the PEEM laboratory. A SHG unit consisting of a half-wave plate, two quartz lenses and a BBO-crystal is used to frequency-double the fundamental laser pulses. A harmonic separator splits the two wavelengths into different pathways allowing for one- and two-colour time-resolved energy-filtered PEEM measurements. A motorized controlled delay stage introduces the desired time delay between the pulses. The power of the fundamental pulses can be adjusted by using a half-wave plate and a thin film polariser. By using a periscope and a further lens the laser is coupled into the EF-PEEM.

Chapter 4

Experimental Results

In the course of the Master's thesis several systems, which exhibit different physical phenomena, have been investigated with the NanoESCA instrument, exploring on one hand the versatility of the microscope and, on the other hand, paving the way for future publications and collaborations. From the mapping of surface plasmon polaritons over photoemission tomography of molecular orbitals adsorbed at single crystalline surfaces to time-resolved studies in the femtosecond regime, the possibilities of energy-filtered photoemission electron microscopy (EF-PEEM) are extensive. However, exploiting this great capability requires a broad knowledge about the strengths and also weaknesses of the instrument, which can only be acquired by a long learning process and, moreover, by hard pioneering work.

The first section of this chapter covers instrumental characterization measurements carried out on various surfaces, introducing the relevant operating modes, the information which can be extracted, and, furthermore, first aspects of limitations in space, energy and momentum measurements. The second section summarizes the first attempts of studies on nanoparticles synthesized by the helium droplet approach and gives an outlook about further important steps in this research field. The third section contains a comparison between the nanosecond and femtosecond laser systems for (EF-)PEEM in terms of the capability of launching and detecting surface plasmon polaritons and an outlook towards momentum-related phenomena of nanostructures prepared by lithography. The last section introduces first time-resolved measurements and shows the current obstacles which have to be overcome in the near future in order to carry out competitive research.

4.1 Instrumental Characterization Measurements

Based on a chapter in Ref. [5], in this section the relevant operating modes of the NanoESCA instrument are briefly introduced by using the helium discharge lamp and a variety of different samples ranging from single crystals to structured surfaces fabricated by electron beam lithography. Beside the great versatility enabled by employing various light sources and measuring electronic phenomena in multiple dimensions, the NanoESCA microscope allows for photoelectron spectroscopy with spatial resolution at the nanoscale surpassing, thereby, comparable systems. Consequently, a discussion about the limitations, such as spatial, energy and momentum resolution, is given, providing a good basis for promising experiments in the near future. However, this section does not only focus on the instrumental specifications but also gives an overview of the data evaluation and

the information which can be extracted in each mode. Note that detailed characterization measurements of the NanoESCA instrument carried out on well-defined systems can be found in the test book provided by Focus GmbH. Finally, important facts about the microscope, neglected by the following paragraphs are reported in other sections within this chapter.

4.1.1 The Real Space Imaging Mode

In principle, the real space imaging mode can be subdivided into ordinary photoemission electron microscopy (PEEM) and the energy-filtered photoemission electron microscopy PEEM (EF-PEEM). While the PEEM mode is characterized by a better spatial resolution and a higher electron transmission, the energy-filtered mode facilitates a variety of different measuring possibilities, to name just a few: energy dependent contrast imaging, work function mapping, spectro-microscopy etc.. In this subsection, the preparing steps of image acquisition and their characteristics depending on the work function and topography and a comparison of the spatial resolution between PEEM and EF-PEEM real space imaging mode are described.

First, the preparational steps when starting with measurements on a new sample are briefly discussed: After insertion of the sample into the main chamber and turning on of the helium discharge lamp, the largest possible field of view is set by applying an extractor voltage of 50 V in order to image the spot of the light source. If the distance between sample and the extractor deviates from the recommended value of 1.830 mm, the light spot of the helium discharge lamp has to be repositioned by adjusting the port aligner. Then, the extractor voltage has to be increased in steps of 100 V per six seconds up to 13 kV while watching the extractor current, which should not exceed 15 μA. If the extractor current seems to be unproblematic, the voltage is set to 12 kV. Subsequently, the iterative process of focusing and adapting the stigmator can be conducted via zooming-in, using focus wobbling and changing to smaller contrast apertures. Note that if the image looks truncated or blurred on one side after adjusting the focus and stigmator settings the deflector has to be adapted in order to guide the entire bunch of electrons through the slit into the first hemisphere.

In Fig. 4.1(a,b,c), a set of EF-PEEM images of a Cu(110) surface are depicted at three different FoVs. In principle, variations of the contrast in the EF-PEEM imaging mode result from lateral work function differences and the surface topography. Considering that Fig. 4.1(a) represents a large field of view, the kinetic energy was chosen at the low energy cut-off of the photoemission spectrum (see Fig. 4.3) in order to strongly enhance the work function contrast. At a first view, a gradient in intensity from left to right can be seen, caused probably by bad lamp alignment or an insufficient adjustment of the deflector. However, work function differences on a single crystal can only appear due to adsorption of residuals such as water, carbon monoxide or remaining molecules from previous deposition experiments, which could not be removed by argon sputtering and annealing. Large bright spots in the right side of Fig. 4.1(a) could possibly indicate such an adsorption induced intensity contrast. The other variations of the electron yield occur mainly from topographic effects. A good overview of different geometric features and their

corresponding PEEM images is given by the schematic in Fig. 4.1(d) taken from Ref. [61]. Considering this simple sketch, the lines covering the surfaces in Fig. 4.1(b,c) could be attributed to scratches and bright spots with shadows (see Fig. 4.1(b,c)) could be small spikes or ridges. From the shadows one can deduce the direction of the incoming light and, moreover, by knowing the angle under which the light falls onto the sample, the height of such spike-like structures can be deduced. As shown by these few selected examples, the interpretation of an EF-PEEM image is more or less difficult depending strongly on the surface preparation. Samples which are directly inserted from ambient conditions may exhibit a severe contamination by water, hydrocarbons or residuals of organic solvents. This could drastically influence the surface and, consequently, the resulting photoemission image, complicating the interpretation.

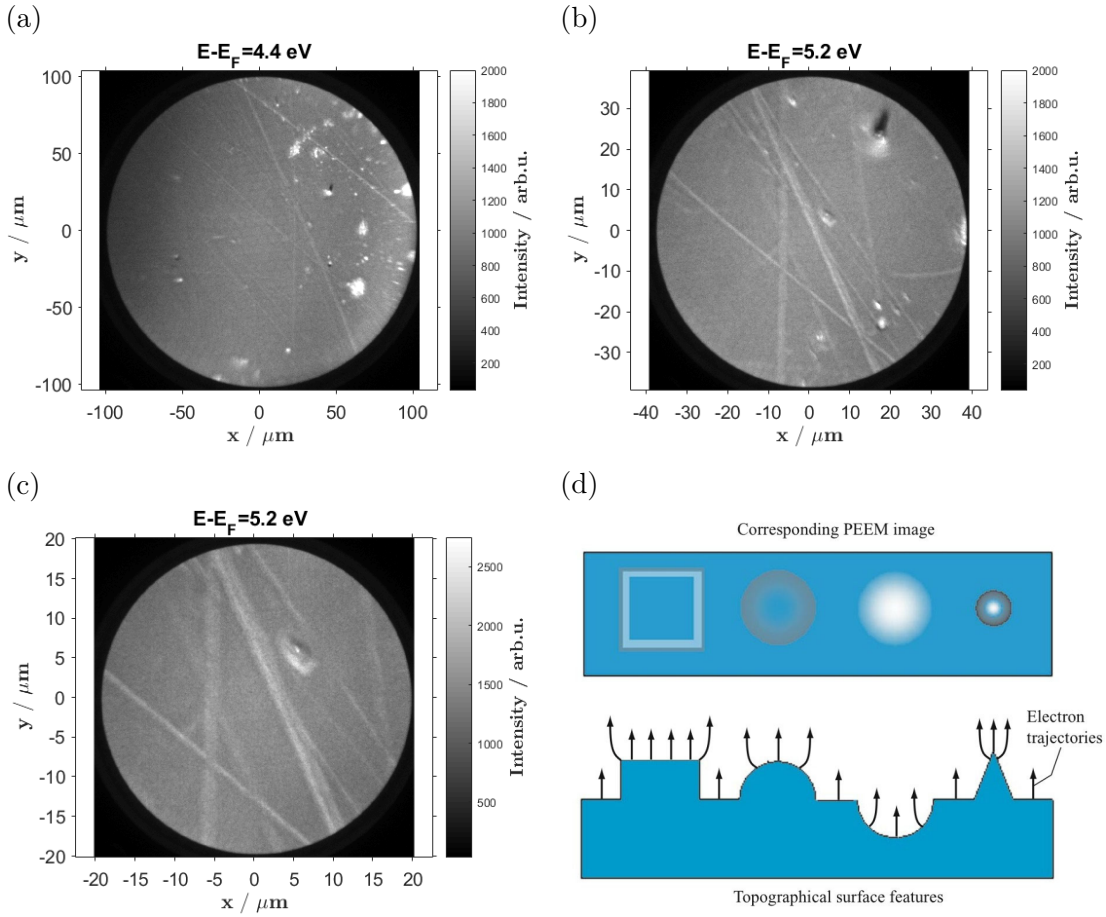

Figure 4.1: (a,b,c) EF-PEEM images of the Cu(110) surface for different magnifications and (d) a schematic showing the impact of topographical surface features on the PEEM image (taken from Ref. [61]).

As already mentioned briefly in the introduction to this subsection, a hot topic in the course of this Master's thesis was the spatial resolution of the NanoESCA instrument, which is specified experimentally as 40 nm [2,3] and theoretically as approximately 10 nm [1]. The restricting factor is mainly the chromatic aberration of the PEEM lenses, such as the objective and projective electron optics, whereas the spherical aberration, which is mostly compensated by the tandem hemisphere configuration, plays a minor role in terms

of lateral resolution. [1] Note that the best possible resolutions that have been reported in literature, e.g. by the H.J. Freund group in Berlin, have been obtained by special aberration corrected systems, i.e. instruments that can correct the chromatic aberration by adaptive optics. These instruments are typically combined LEEM/PEEM setups. [62] Due to ongoing interest in improving the lateral resolution, this topic is discussed several times in the scope of the thesis on the basis of different experimental results. Note also that it is not advisable to speak about the resolution of the NanoESCA instrument as this depends strongly on the sample and the light source but also on the way the resolution is determined. In particular, values for resolutions represent best case scenarios where a clear contrast at an edge, for example, has been observed. Thus, it is recommended to always state the sample material and structure as well as, the light source for which a certain resolution was achieved deduced by a certain criterion such as the 16%/84% edge contrast method. Here, a comparison of the ordinary PEEM with the EF-PEEM mode is given with respect to the spatial resolution.

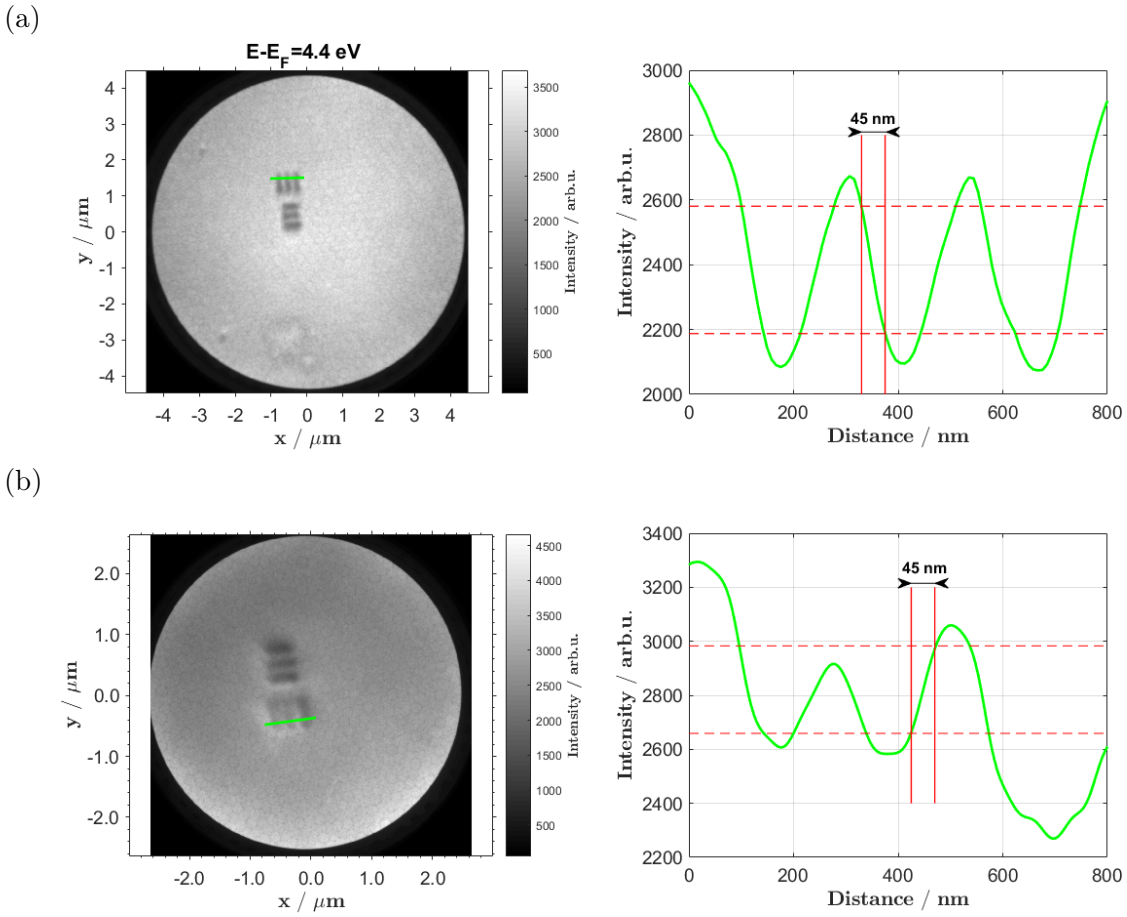

Figure 4.2: (a) EF-PEEM image of Ag bar structures for determining the lateral resolution with a line profile and the standard 16%/84% criterion using the He lamp. (b) PEEM image of the same Ag bar structure and the corresponding line profile leading to a similar result of the lateral resolution as for (a).

According to the manuals [2, 3] the PEEM mode is often characterized by its better resolution due to the higher transmission and less electron lenses, hence smaller aberration effects. However, measurements carried out with the He lamp in the course of this Master's thesis could not prove this statement and, moreover, showed even a contrary behaviour. In many cases the topographic effect in the photoemission signal turns out to be not sufficient for a good contrast. At the expense of the electron transmission through the photoemission setup a much better contrast could be achieved by applying the energy-filtered imaging mode, as shown by a lithographed Ag bar structure on an ITO (indium tin oxide) substrate in Fig. 4.2. Nevertheless, in both cases the resulting spatial resolution obtained from the line profiles and the 16%/84% criterion barely distinguishes from each other. Note that, although this rather simple determination of resolution is the standard method, one has to be careful in interpreting the results due to its subjective nature. Furthermore, it has to be mentioned that in Fig. 4.2(a) the telescopic lens setting and, thus, a larger field of view was used, further complicating this comparison.

4.1.2 The Spectroscopy Mode

The spectroscopy mode uses the classical photoemission setup consisting of electron optics, an hemispherical analyser and a counting device (channeltron). The NanoESCA instrument allows for selecting a region of interest by using different FoVs and the variable iris aperture in the real space mode. Beside the area selection, the angular acceptance of the emitted photoelectrons can also be controlled by five different contrast apertures. In real space mode, a smaller contrast aperture improves the spatial resolution by restricting the angular phase space to normal emission. The spectroscopy mode, however, usually calls for a large contrast aperture in order to access electrons from the vicinity of the Brillouin zone boundaries, except in the case of measuring the work function, which should preferably be done with normal emitting photoelectrons. Furthermore, the energy resolution of the photoemission setup is mainly determined by the pass energy and the entrance slit width, expressed in Eq. 3.2. Here, the relevant aspects of the spectroscopy mode are discussed by considering the key elements of a classical UPS spectrum.

In Fig. 4.3, for example, the ultraviolet photoemission spectrum (UPS) of a Cu(110) surface is shown. Besides the energy scale relative to the Fermi energy $E - E_F$ the x-axis is also labelled with binding E_{bin} and kinetic E_{kin} energy. The energy relations are given in Eq. 3.5 and Eq. 3.6. From such a spectrum several information about the electronic structure can be extracted. Starting at low kinetic energies, the photoemission onset provides information about the work function, the necessary energy in order to eject an electron from the surface. The onset is followed by the so-called secondary electron peak and a continuous decrease of the photoemission signal forming the background consisting mainly of secondary electrons, i.e. electrons which scattered inelastically on their way to the surface. On top of the secondary electron background, characteristic features associated with the valence band of a material appear, strongly depending on adsorbed molecules and crystalline orientation. Here in Fig. 4.3, the dominant feature of the spectrum, the peak-like structure ranging from -2 eV to -5 eV binding energies, can be attributed to the 3d-band of a Cu(110) surface. Above the 3d-band, a linear decrease towards the Fermi cut-off (Fermi edge) can be seen, originating from the sp-bands and the

surface states. Furthermore, at higher binding energies (-6 eV to -10 eV) some artifacts appear corresponding, likely, to adsorption of CO, water or residuals from previous experiments. The last prominent feature towards increasing kinetic energies is the already mentioned sharp Fermi edge, indicating the metallic character of the sample. The Fermi cut-off represents the electrons which are ejected from the Fermi level where E_bin is defined to be zero and, consequently, $E - E_F$ to be the photon energy of the light source $h\nu$ (HeI 21.22 eV). In case of a semiconductor material, the photoemission signal decreases continuously towards zero binding energy, revealing information about the position of the valence band maximum. In the case of an intrinsic semiconductor, one can determine the energy difference between the top of the valence band and the bottom of the conduction band, as the Fermi level is located in the middle of the band gap. However, for an extrinsic semiconductor, in general, the position of the Fermi level depends strongly on the doping, thus, additional measurements, such as inverse photoemisssion spectroscopy (IPES) [30] or common absorption spectroscopy techniques, are required in order to fully unveil the band structure around the Fermi level.

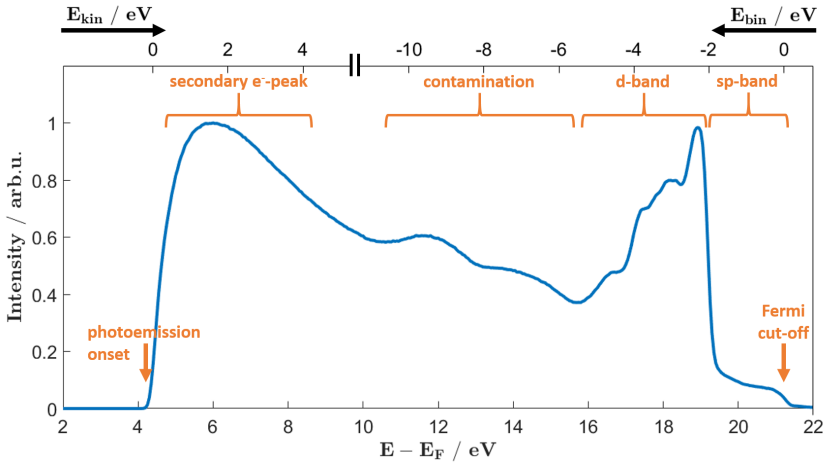

Figure 4.3: UPS spectrum of a Cu(110) surface. The main features of such a spectrum are the photoemission onset for identifying the work function, the secondary electron peak followed by continuous decrease of the signal, the Fermi cut-off (Fermi edge) indicating the metallic character and the electronic structure of the valence band, here the 3d-band of Cu(110) ranging from -2 eV to -5 eV binding energies. The linear decrease above the 3d-band can be attributed to the sp-band and the surface states of Cu (110). At higher binding energies (-6 eV to -10 eV) adsorption of CO, water or organic residuals from previous experiments can be observed.

As depicted in Fig. 4.4(a), the work function is determined by the photoemission onset, the so-called low energy cut off. In a first approximation the work function can be evaluated by a simple linear fitting procedure. A tangent is applied to the data point of inflection (i.e. maximum of the first derivative) and the point of intersection between the baseline and the tangent serves as a preliminary result of the work function. Additionally, a correcting factor [5] given by the energy resolution of the analyser (see Eq. 3.2) is added to the preceding value. For the Cu(110) surface, therefore, a work function of approx. $\Phi = 4.5\ eV$ can be deduced, which agrees well with literature ($\Phi = 4.4 - 4.5\ eV$) [21,63].

The total energy resolution of the photoemission setup, depending on temperature, spectral bandwidth of the HeI emission line and the hemispherical analysers, can be estimated from the Fermi edge. Using the 16%/84% criterion, as shown in Fig. 4.4(b), the energy resolution results in $\Delta E = 0.5$ eV, clearly exceeding the energy resolution given by the analyser ($\Delta E = 0.2$ eV, corresponding to a pass energy of 50 V and a slit width of 1 mm). This can be explained by the linear descent towards the Fermi edge due to the secondary electrons, the sp-bands and the surface states of Cu(110). Furthermore, this negative linear slope is also observable above the Fermi energy created primarily by the background of the omnipresent weak HeII line (42 eV).

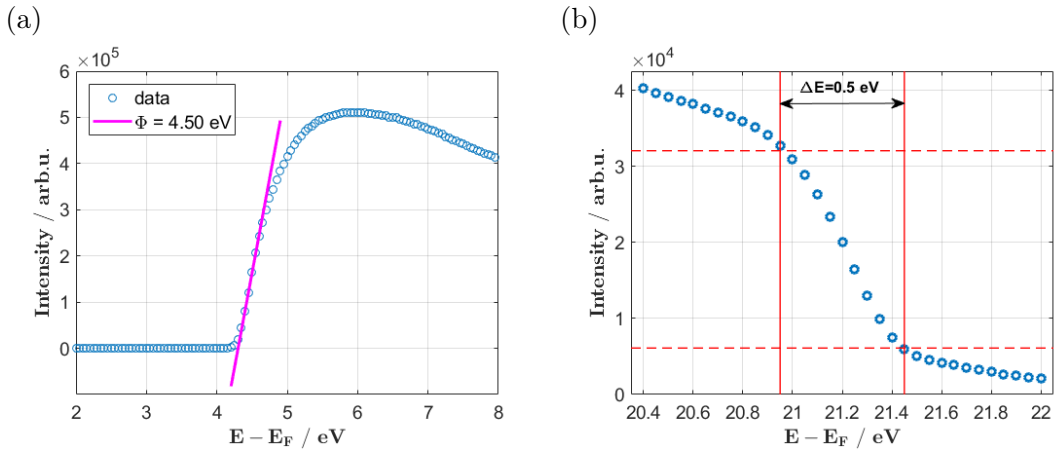

Figure 4.4: Determination of (a) the work function of a Cu(110) surface and (b) the total energy resolution of the photoemission setup by using simple models.

A more sophisticated fit model for calculating the work function and the energy resolution is introduced by Ref. [5]. It comprises, on the one hand, the rough shape of the measured photoemission spectrum (PES-model) described by a descending error-function and, on the other hand, the work function edge represented by a convolution of a Gaussian function and a step-function, resulting also in an error-function. The overall fit model for the photoemission intensity $I(\xi = E - E_F)$ can be written as

$$I(\xi) = \frac{1}{2} \cdot \left(1 + erf\left(\frac{\xi - c_{wf}}{\sqrt{2}\sigma_{wf}}\right)\right) \cdot \frac{I_0}{2}\left(1 - erf\left(\frac{\xi - c_{pes}}{\sqrt{2}\sigma_{pes}}\right)\right) \tag{4.1}$$

with the maximum intensity I_0, the center of the descending error-function c_{pes} and its standard deviation σ_{pes}, the work function c_{wf} (the center of the ascending error-function) and its standard deviation σ_{wf}. The energy resolution ΔE, however, can be determined by fitting the Fermi edge with the descending error-function (PES-model) and by calculating the full width at half maximum (FWHM) of the Gaussian contribution

$$\Delta E = 2\sqrt{\ln(2) \cdot 2} \cdot \sigma_{pes}. \tag{4.2}$$

To show the applicability of this sophisticated fit model, UPS spectra of a monolayer H_2TPP evaporated on Ag(100) were recorded using a contrast aperture of 150 μm. The secondary electron peak and the Fermi edge are depicted in Fig. 4.5. As shown in

Fig. 4.5(a), the photoemission onset is described appropriately by the ascending error-function. However, for the secondary electron peak and the following descent the used PES-model does not perfectly reproduce the data points. Thus, another model may be more reasonable for the investigated system. The Fermi energy, however, can be well modelled by the descending error-function, as depicted in Fig. 4.5(b). An experimental energy resolution of 210 meV can be deduced which agrees with the energy resolution of the analyser given by the pass energy and the slit width.

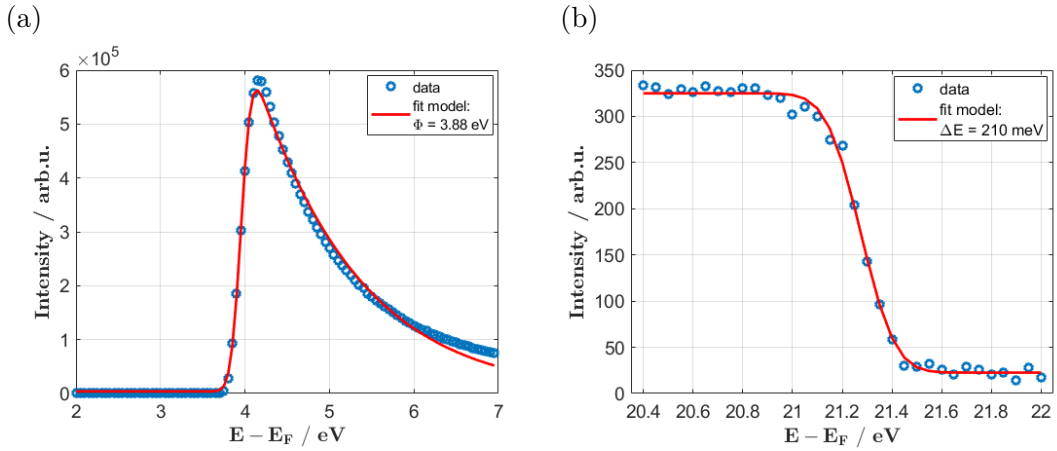

Figure 4.5: Determination of (a) the work function of a monolayer H_2TPP on a Ag(100) surface and (b) the total energy resolution of the photoemission setup by using the sophisticated fit model provided by Ref. [5].

4.1.3 The k-Space Imaging Mode

ARPES (angular resolved photoemission spectroscopy) is a direct experimental technique to observe the distribution of the photoelectrons in the reciprocal space in solids. By using a conventional light source, supporting a one photon photoemission (1PPE) process, the filled states in a material can be probed and, due to the momentum sensitivity of the ARPES technique, the electronic band structure can directly be measured allowing for a determination of important material characteristics such as electron effective mass, Fermi velocity, the valence band maximum (VBM) energy and its position, doping, and many-body effects. [64] For ARPES measurements the sample has to fulfill a few requirements beside the fact of a clean surface: The sample has to be crystalline to possess an ordered band structure and its surface has to be smooth in order to conserve the k-parallel component of the photoexcited electron from the crystal to the vacuum. [64, 65]
Typical ARPES setups equipped with a 1D or 2D detector employ a number of sample rotation mechanisms in order to discriminate between the emission angles, whereas the NanoESCA instrument or in general an EF-PEEM can simply map for a range of kinetic energies the full-wavevector landscape without moving or rotating the sample, creating a great advantage over competing systems. In particular, for the NanoESCA instrument, by applying different settings on the two subsequent projective lenses in the telescopic mode, either the spatial or angular photoelectron distribution can be mapped onto the detector, see section 3.1.4. If the focus and the stigmator are well adjusted for a specific

region of interest in the real space telescopic mode, one can easily switch to k-space mode. The k-space image or PAD (photoemission angular distribution) pattern of the selected region of interest can then be optimized by using the second stigmator, following a similar procedure as for the objective lens in the real space mode. In Fig. 4.6(a), a set of energy filtered k-space images is shown, featuring the 3d-band of the Cu(110) surface.

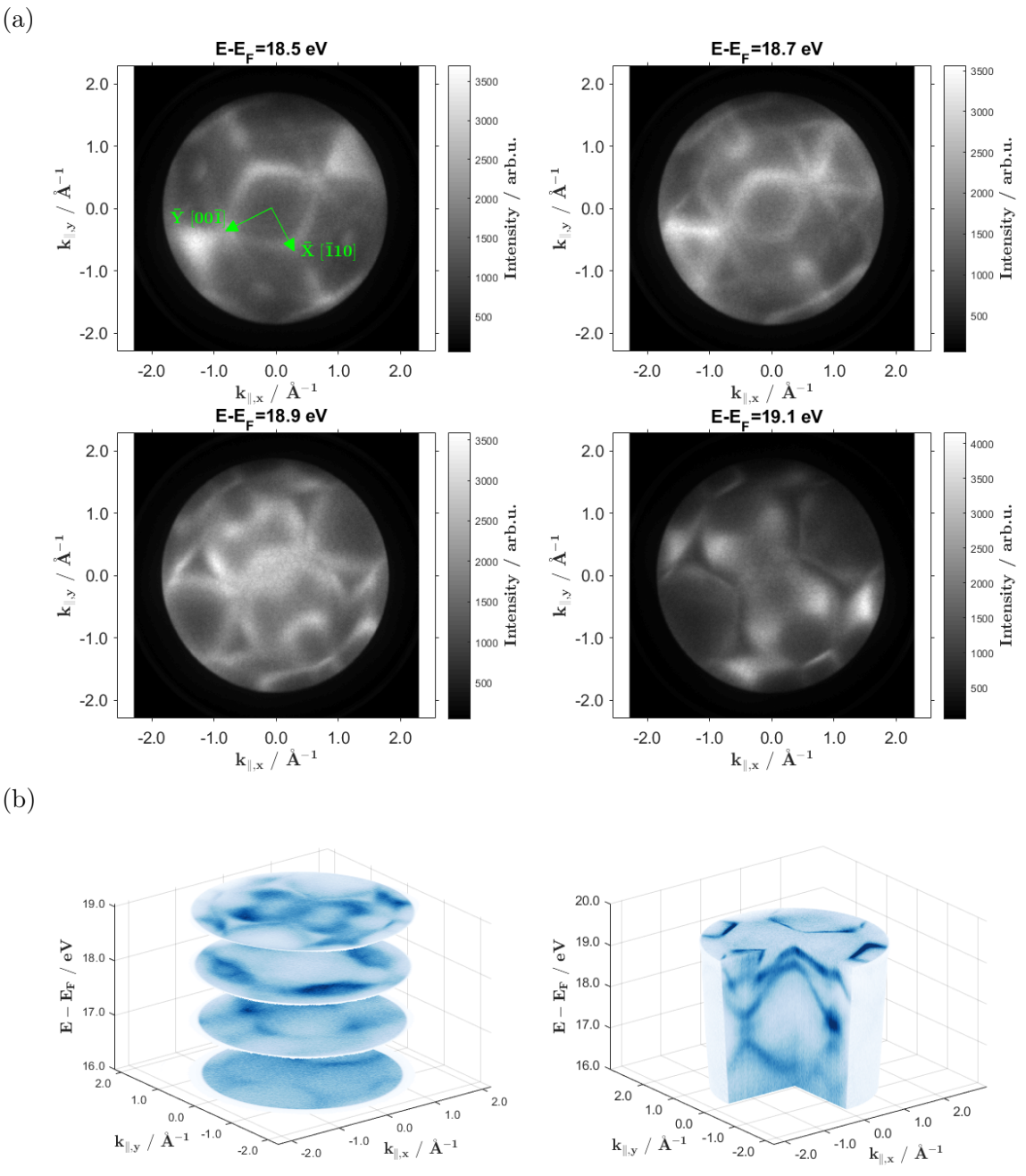

Figure 4.6: (a) Set of EF-PEEM k-space images of the Cu(110) 3d-band. (b) Stack of the energy-filtered k-space images and the corresponding data cube showing an overview of the band structure of the Cu(110) 3d-band.

The energy- filtered momentum maps are labeled by $k_{\parallel}$, the momentum direction parallel to the surface, see Fig. 2.11. Furthermore, green arrows indicate the $\bar{\mathrm{X}}$ $[\bar{1}10]$ and $\bar{\mathrm{Y}}$ $[00\bar{1}]$ direction for Cu(110) according to Ref. [66]. By stacking the images and cutting off a quarter of the data cube an overview of the band structure can be extracted as depicted in Fig. 4.6(b).

For monitoring the band structure along a specific direction an additional program package was developed providing a 2D image of the energy-momentum band dispersion originating from the Γ-point. By applying this program to the Cu(110) image stack, considering the energy region just below the Fermi edge, one can extract the band dispersion along the Y [001] direction showing the surface states in the projected bulk band gap and the sp-band, see Fig. 4.7.

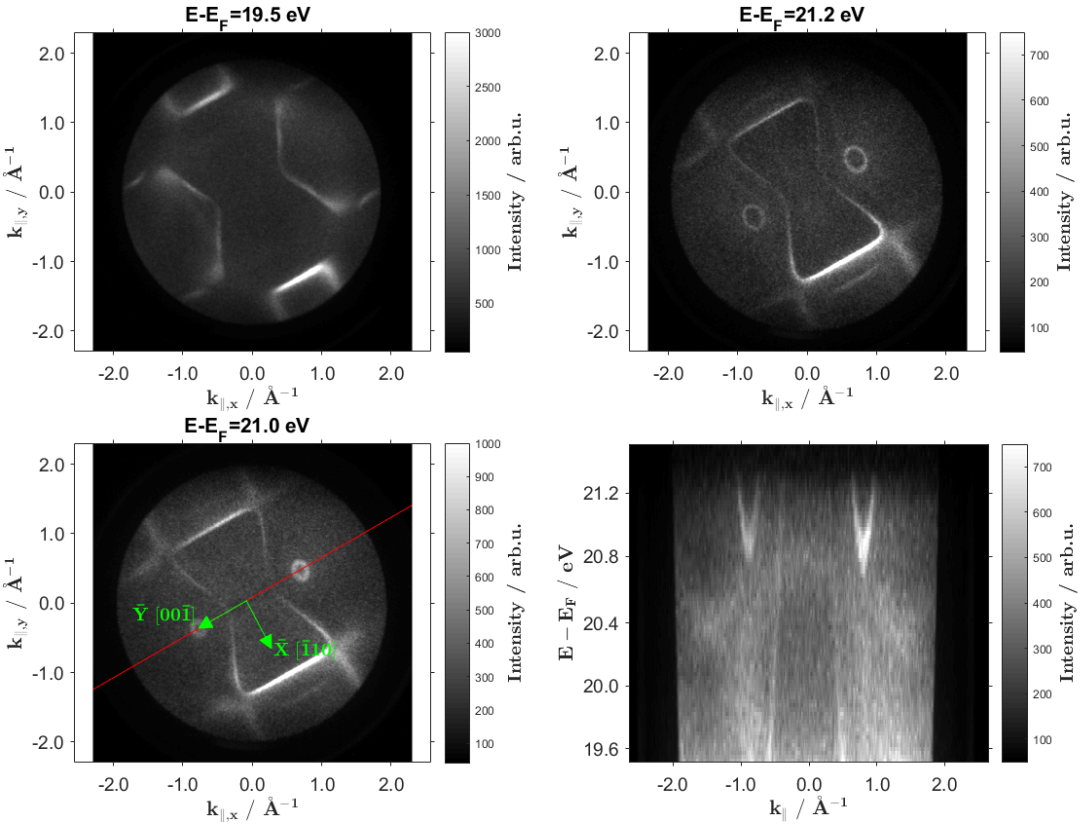

Figure 4.7: EF-PEEM k-space images and the band dispersion along the Y [001] direction of the Cu(110) surface showing the sp-band and the surface states.

From such image stacks also angle resolved photoemission spectra can be created by selecting a specific region of interest in the PAD and reading out the intensities as a function of the kinetic energy. Fig. 4.8(a) presents the momentum map at 20.4 eV of a Bi_2Se_3 crystal with selected regions and in (b) the corresponding photoemission spectra are depicted, showing the angular dependence. In particular, the region around the Γ-point (red) exhibits two small peaks in the vicinity of the Fermi energy which are associated with a characteristic feature of this topological insulator, namely the Dirac cone [11]. By plotting the full recorded data set and, particularly, the interesting region just below the Fermi edge, Fig. 4.8(c,d), one can observe the Bi_2Se_3 surface state. Note that the entire

image stack (c) shows a kink at 20 eV originating from separate image acquisition series with different stigmator settings, which could have experimentally been avoided. Furthermore, since the photoemission signal decreases rapidly towards the Fermi energy (see (b)), the grey scale of the data set was calibrated by the total angle-integrated spectrum ((a,b) blue) in order to enhance the relatively small photoemission signal above 20 eV. This spectroscopy tool can also be applied to image stacks acquired in the real space mode visualizing local variations in the photoemission spectra depending on material, crystallography or adsorption. Employing element-specific mapping requires, however, characteristic core level states, which are located at larger binding energies. With commercial discharge lamps such energy regions cannot be accessed, one would need either, in the best case, synchrotron radiation or at least an x-ray tube at the expanse of spatial resolution.

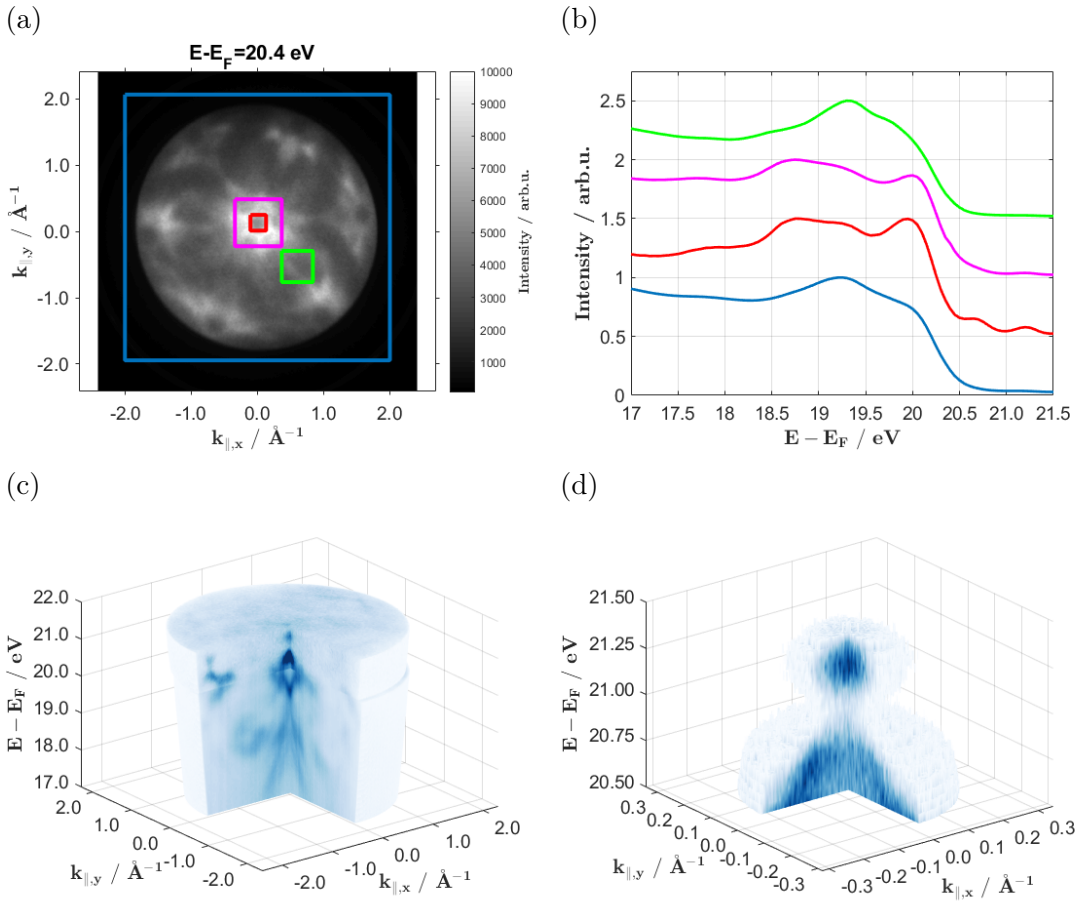

Figure 4.8: (a)Momentum map acquired from a Bi_2Se_3 surface with marked regions for further investigation. (b) Corresponding spectra extracted from the entire image stack. (c) Full set of data of energy filtered momentum distributions of a Bi_2Se_3 crystal. (d) The Dirac cone at the Γ-point showing origin of the two peaks of the red curve in (b) in the vicinity of the Fermi energy.

While in real space the field aperture restricts the area from where the photoexcited electrons are gathered, the contrast aperture serves as the limiting tool for the angular acceptance in momentum space. Accessing electrons from the vicinity of the Brillouin

zone boundaries calls for a large contrast aperture (e.g. $CA = 1750\ \mu$m), whereas for determining work functions, improving spatial resolution and avoiding space charge effects [67] a small contrast aperture (e.g. $CA = 30,\ 70$ or $150\ \mu$m) is more appropriate, restricting the angular acceptance to normal emission of the photoexcited electrons. Furthermore, considering the free electron dispersion, the energy increases with the square of the absolute value of the momentum vector $E(\mathbf{k}) = \hbar^2 k^2 / 2m$, as shown in Fig. 4.9, which represents the so-called photoemission horizon recorded from a highly oriented pyrolytic graphite (HOPG) sample. This means that not only the contrast aperture limits the angular acceptance but also the kinetic energy of the photoexcited electrons and, consequently, the photon energy of the light source. If one wants to investigate dynamic processes on a surface, such as, for example, the charge transfer from a metal or an oxide surface to a molecular orbital, one has to assure that the observable k-range can be accessed with the photon energy. [68–70]

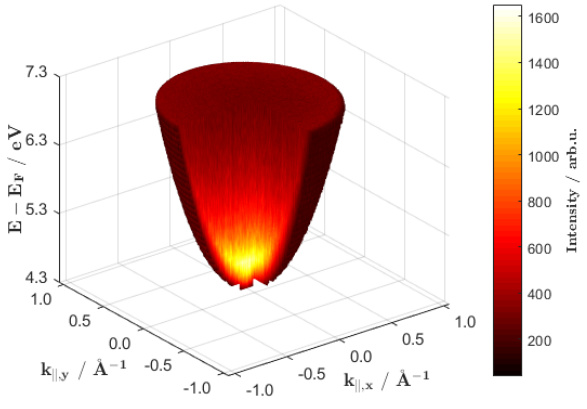

Figure 4.9: The so-called photoemission horizon from a highly oriented pyrolytic graphite (HOPG) surface demonstrating the constraint in momentum of photoexcited electrons with low kinetic energy.

4.2 A new Investigation Method for Nanoparticles Synthesized with the Helium Droplet Approach

The enormous progress in the fabrication of nanoparticles in the last decades has pushed the frontier of science. This has enabled applications in various fields such as catalysis [71], photovoltaics [72], optoelectronics [73] and medicine [74]. All of these mentioned applications have something in common, namely the exploitation of the plasmonic properties of nano-sized structures. The research field of plasmonics deals with the study of the interaction between free electrons in a metal and an electromagnetic field. Approaching sizes smaller than the wavelength of incoming light, plasmonic materials can confine the collective oscillation of electrons within the nanoparticle as a response to a resonant photoexcitation. This is then called localized surface plasmon resonance (LSPR).
Tackling the challenge of emerging new or improving existing applications calls for novel synthesis methods and sophisticated analysing tools. The Institute of Experimental Pysics at Graz University of Technology satisfies both conditions. The helium nanodroplet synthesis method can produce functional hybrid nanoparticles with tailored plasmonic properties [75, 76] utilizing its advantages over other synthesis approaches: the intrinsic inertness of the synthesis environment, the large variety of dopant combinations and the cold environment [77, 78]. In the last years, photoelectron emission microscopy proved to be a successful experimental method for investigating plasmonic properties of metal nanoparticles with energy, spatial and temporal resolution [79–82]. Consequently, the NanoESCA instrument with its aberration corrected hemispherical analysers could contribute significantly to the exploration of plasmonic phenomena, such as field enhancement and dynamic effects. Within the course of this Master's thesis, first experiments have been performed, showing that it is feasible to investigate plasmonic nanoparticles, formed by the helium nanodroplet synthesis approach, with the NanoESCA instrument.

4.2.1 Ag Clusters - A Spectro-microscopic Analysis

A simple and well known system has been chosen as a first step towards new plasmonic materials. The controlled formation of silver clusters within helium nanodroplets and their characterization with electron microscopy have been subject to prior research at the institute [83–85]. Furthermore, coinage metals exhibit a localized surface plasmon resonance in the visible region, especially Ag clusters show a strong absorption around 400 nm [86]. Hence, the second harmonic of a Ti:sapphire laser is a proper choice for photoexciting the LSPR in silver nanoparticles.

Before introducing details about the cluster synthesis, a few words about the substrate preparation should not be omitted. Three important facts have to be considered when preparing a new sample. First, *ex-situ* cleaning can be done with organic chemicals, however, for photoemission experiments additional UHV-cleaning procedures, such as Ar-ion sputtering and annealing, are essential in order to remove undesired residuals, which could influence the measurement and complicate the interpretation of the results. Second, the distance between extractor and the sample surface has to be between 1.63 mm and 2.13 mm for focussing and lamp aligning issues. Third, since a voltage is applied to the sample holder, the surface has to be conductive and in contact with the sample holder.

In the case of the Ag cluster deposition, a p-type Si-wafer was used as a substrate cleaned with isopropanol, aceton and methanol. The Si-wafer was glued with a silver adhesive on an aluminium platform, which is glued itself to a commercial sample holder from Ferrovac, meeting the condition of the distance between extractor and surface. However, for this substrate assembly the extractor voltage could not be increased to 12 kV due to large current fluctuations. For future experiments, either the original sample holder from Scienta Omicron or the self-made one from the workshop at KFU should be used.

Details of the employed helium droplet apparatus can be found in Ref. [87]. In the source chamber, the helium droplet beam is generated by a supersonic jet expansion of highly purified helium gas through a small nozzle (5 μm) into vacuum at cryogenic temperatures. By varying the nozzle temperature and the stagnation pressure of the helium gas a wide range of droplet sizes can be accessed. In the pickup chamber, the helium droplets are doped with foreign species in resistively heated pickup cells. Upon contact, the helium droplets capture the evaporated atoms, which agglomerate inside the droplets and form clusters. The binding process of the embedded particles releases energy, which leads to an evaporation of He-atoms. [84, 88] This attenuation of the helium droplet beam or, moreover, the dopant pickup can be controlled by monitoring the ^{4}He yield with a quadrupole mass spectrometer at the end of the apparatus. The setup with two consecutive pickup cells enables the fabrication of core–shell clusters by sequential doping with two materials. The deposition of the metal clusters, enclosed in He droplets, on the desired substrate takes place under so-called 'soft' landing conditions, where the nanoparticles do not break up and do not get implanted into the surface, whereas the helium droplets, disintegrate and evaporate upon impact. [89–91]

For the Ag cluster experiment, helium at a stagnation pressure of 20 bar was cooled down to 8 K resulting in a mean droplet radius of about 40 nm [88]. The Ag clusters, agglomerated inside the helium droplet, were deposited on a p-type Si-wafer for approx. 45 min. The sample was then transferred from the helium droplet apparatus to the NanoESCA instrument under UHV conditions. As already mentioned above, for the glued substrate assembly the extractor voltage could not be increased to the recommended voltage of 12 kV due to large current fluctuations. Therefore, the extractor voltage was set to 8 kV leading to an acceptable extractor current. For the EF-PEEM experiments, pre-characterization measurements were performed with the helium discharge lamp and possible plasmonic activity was investigated by illuminating the sample with the second harmonic of the nanosecond laser system Ingigo-S. Unfortunately, the settings for the contrast aperture were not chosen wisely. For the imaging mode the $CA = 500$ μm was used and UPS-spectra were recorded with the $CA = 30$ μm restricting the photoemission signal to normal emitting electrons. As described in section 4.1, in case of the spectroscopy mode the largest contrast aperture ($CA = 1750$ μm) would be the better choice enhancing the valence band signal and in case of the imaging mode a smaller contrast aperture (e.g. $CA = 150$ μm) would improve the lateral resolution.

The EF-PEEM image in Fig. 4.10 shows a clear difference in contrast between the regions of the pristine p-type Si-wafer and the Ag cluster deposition. Considering the corresponding UPS spectra of the two areas, the low kinetic energy cut-off of the Ag cluster regime

is slightly shifted to lower kinetic energies in comparison to the p-type Si-wafer initiating the strong contrast mechanism in the EF-PEEM image. As described in previous sections, the work function can be determined from the secondary-electron cut-off. Since the position of the contrast aperture ($CA = 30\ \mu$m) was not checked in the k-space mode, a

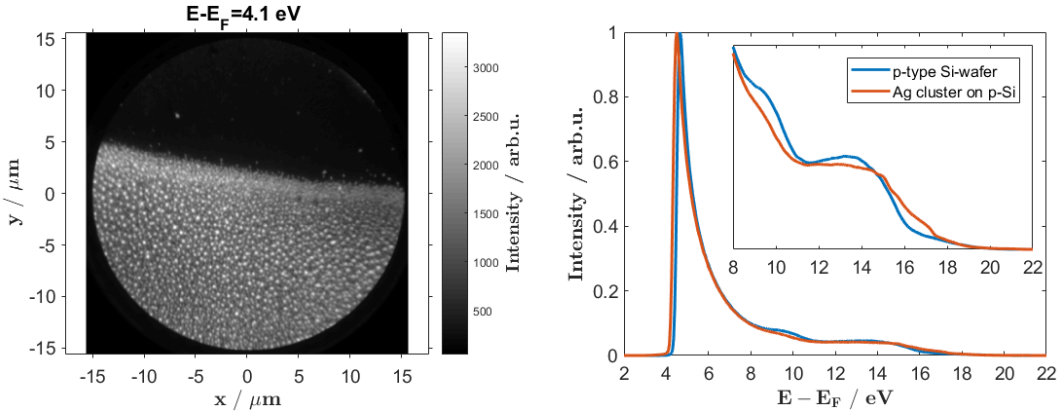

Figure 4.10: EF-PEEM image and the corresponding UPS-spectra of the pristine p-type Si-wafer region and the Ag cluster deposited region. A clear difference in contrast originates from a shift of the low kinetic energy cut-off towards smaller energy for the Ag cluster area. The insert in the UPS-spectra shows a small deviation in the valence band regime, which can be assigned to the Ag d-band.

precise statement about the work function could not be made. However, the EF-PEEM image indicates an obvious difference in work function which could be caused either by the bulk property of silver (polycrystalline Ag $\Phi = 4.26$ eV [92]) or by the interplay between dipole inducing mechanisms and size related effects [93]. Furthermore, the UPS-spectra in the valence band regime (insert) also support the allegation that Ag clusters were deposited on the p-type Si-wafer. First, the UPS-signal of the pristine wafer material is suppressed due to deposition of some material. Secondly, additional features beyond 14 eV appear originating from the valence d-band of silver [94].

Zooming in on the deposited cluster region, in Fig. 4.11 two EF-PEEM images are depicted for different magnifications. Additionally, a size distribution and a line profile were created giving information about the statistics of the deposited nanoparticles and the spatial resolution of the NanoESCA instrument. For the EF-PEEM with the larger field of view (top-left), a mean cluster diameter of about 110 nm can be determined exceeding clearly the dimensions deduced from the results of transmission electron microscopy experiments [83]. One possible reason for this could be the single crystalline substrate on which the Ag nanoparticles were deposited. The 'perfect' surface allows for a high mobility and thus, for a higher probability of agglomeration processes after deposition. The next aspect which has to be considered is that the spatial resolution of the NanoESCA instrument also contributes to the imaging process, consequently the observed images are always a convolution of the lateral resolution and the real size of the particle. According to *Focus GmbH* [2, 3] a lateral resolution of less than 40 nm can be achieved. The line profile extracted from the EF-PEEM image with the largest magnification (bottom-left)

in Fig. 4.11 clearly reveals that the specified resolution limit can be reached. Nevertheless, the spatial resolution of the NanoESCA instrument is still restricted by chromatic and spherical aberration issues. For a lateral resolution on the order of a few nanometers, a more sophisticated aberration correction of the electron optics design is inevitable as, for example, realized by the so-called SMART microscope (Spectro-Microscopy with Aberration correction for many relevant Techniques) at BESSY II [62, 95]. This new type of spectromicroscope combines an improved ordinary LEEM/PEEM instrument compensating simultaneously chromatic and spherical aberration and an imaging energy analyzer delivering a lateral resolution of 2.6 nm and an energy resolution of 180 meV. [62, 95]

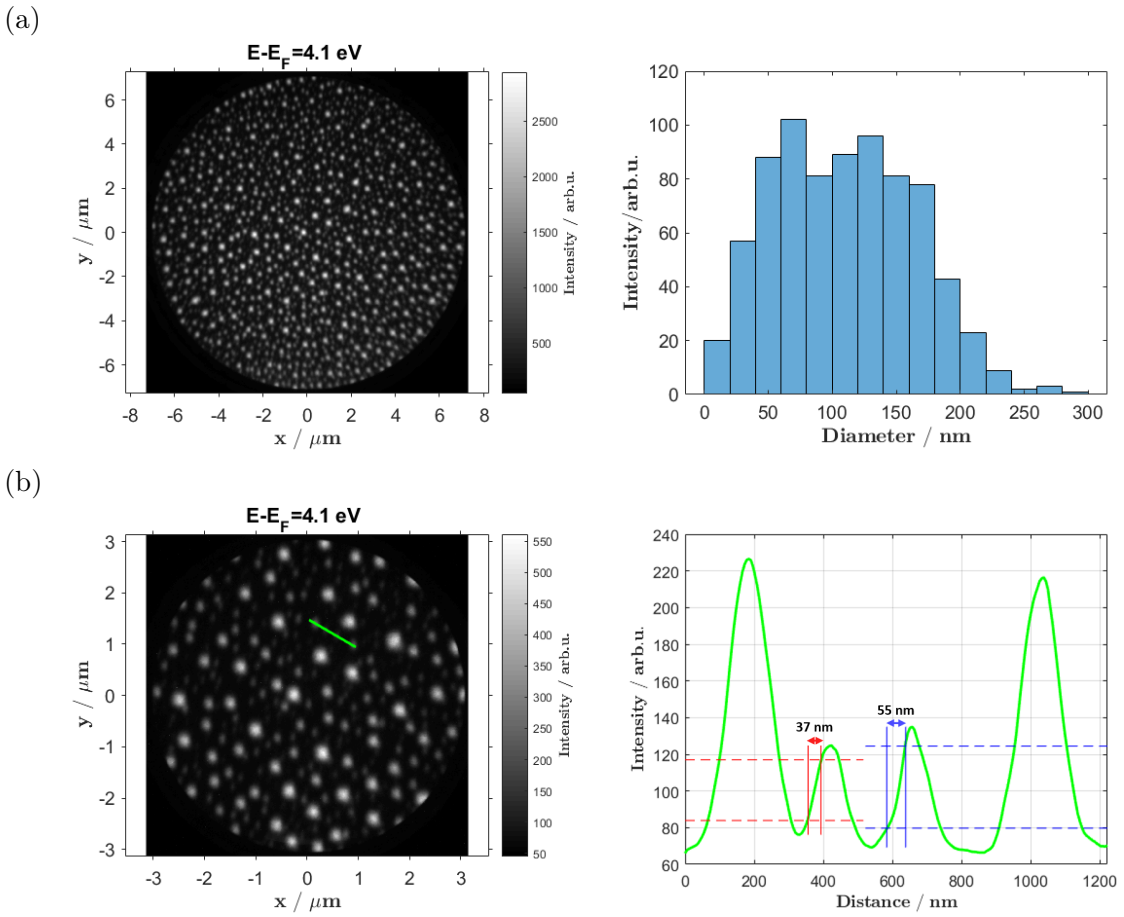

Figure 4.11: (a) EF-PEEM image and the corresponding size distribution of Ag clusters deposited on a p-type Si-wafer. (b) EF-PEEM image with a larger magnification and an indicated line profile showing the lateral resolution of the NanoESCA instrument, according to the 16%/84% criterion.

As already mentioned above, coinage metals exhibit a localized surface plasmon resonance in the UV or visible region. For silver nanoparticles, this collective electron oscillation can be resonantly excited by light at a wavelength around 400 nm. In a first attempt, the second harmonic (approx. 385 nm) of the nanosecond laser system Indigo-S was used as photon source in order to observe plasmonic activity. The average power was

set to 25 mW, the diameter of the laser spot at the sample surface was determined to approx. 150 μm and, by considering the repetition rate (5 kHz) and the pulse duration (20 ns), this results in a peak power density of approx. $8 \cdot 10^8$ mW/cm^2. Fig. 4.12 shows a set of EF-PEEM images of the Ag cluster region for various magnifications. Note that these images do not correspond to the same sample position as in Fig. 4.10 and 4.11. In contrast to the helium discharge lamp the EF-PEEM images recorded with the nanosecond laser feature hot spots, preventing an appropriate MCP voltage for high quality imaging. Furthermore, the particles deviate from the circular shape as observed in the HIS recordings and appear more blurred. Considering these facts, one can interpret these as field enhancement effects originating from localized surface plasmon resonances. However, in the case of photoexcitation with a laser the aspect of space charge effects must not be neglected, which can lead to hot spots and to an image blur [67]. Consequently, in order to assure that the nanoparticles exhibit a plasmonic activity as a response to a resonant laser excitation one has to determine, in a first step, the critical laser fluence threshold which describes the onset of space charge effects. This can be done by recording energy spectra as a function of the average laser power, c.f. Ref. [67]. In case of a resonant LSPR excitation and the absence of space charge effects, the 2PPE spectra should unveil an enhancement of the photoemission yield in comparison to the pristine substrate surface, a difference in spectral shape, e.g. a clear edge at the Fermi energy due to the metal nanoparticles, and a polarization dependence. [96]

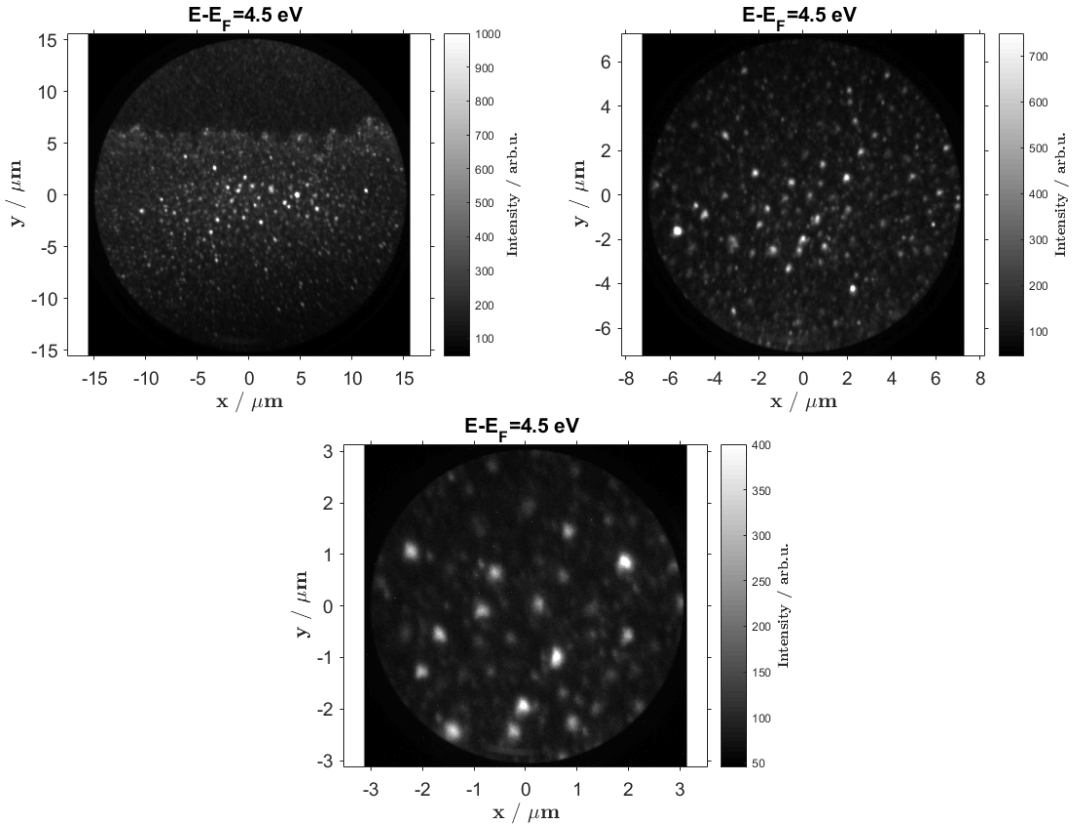

Figure 4.12: Set of EF-PEEM images of Ag clusters recorded with the second harmonic of the nanosecond laser system Indigo-S.

4.2.2 Various Nanoparticles under Investigation

Due to the successful spectro-microscopic detection of Ag clusters, several nanoparticles, such as gold (Au), zinc-oxide (ZnO) and even vanadium pentoxide (V_2O_5), were synthesized with the helium droplet approach and investigated by the NanoESCA instrument. However, reliable microscopic evidence could not be provided for all of those mentioned materials. In this subsection, the relevant experiments carried out in the course of the master's thesis are briefly summarized in a didactic way explaining the improvements in sample preparation or in the operation of the instrument.

As an additional well understood cluster system, gold nanoparticles were fabricated and deposited on a p-type Si-wafer. This time the original sample holder from Scienta Omicron was used, facilitating the ideal extractor voltage of 12 kV and the recommended distance of 1.830 mm between extractor and surface. Furthermore, on the basis of previous measurements, the function and the implementation of the contrast aperture was reconsidered. For the spectroscopy mode, a large contrast aperture is preferable accessing a broad regime in reciprocal space. On the other hand, a small contrast aperture is more favourable for determining work functions due to the restriction of the momentum space to normal emission. For the real space imaging mode, a small contrast aperture can improve the spatial resolution. When applying a small contrast aperture, its position in the electron optic system has to be checked by using the k-space mode in order to assure an optimal transmission of the photoexcited electrons through the electron optics. In the case of the Ag clusters, a clear deposition edge was found whereas for the Au deposition such a segregation could not be imaged. One possible reason, as shown in the PEEM image of Fig. 4.13(a), could be the contamination of the surface by the *ex-situ* cleaning procedure which also influenced the work function of the bare Si-wafer, as indicated by the UPS-spectra in Fig. 4.13(b). Hence, the *ex-situ* cleaning procedure with organic solvents, such as aceton, isopropanol and methanol, has to be reconsidered in order to assure trouble-free measurements. This implies again the necessity of UHV-cleaning. While the installation of the preparation chamber is not yet complete, alternatives have to be found such as preliminary analysis of the bare substrate before depositing the nanoparticles or

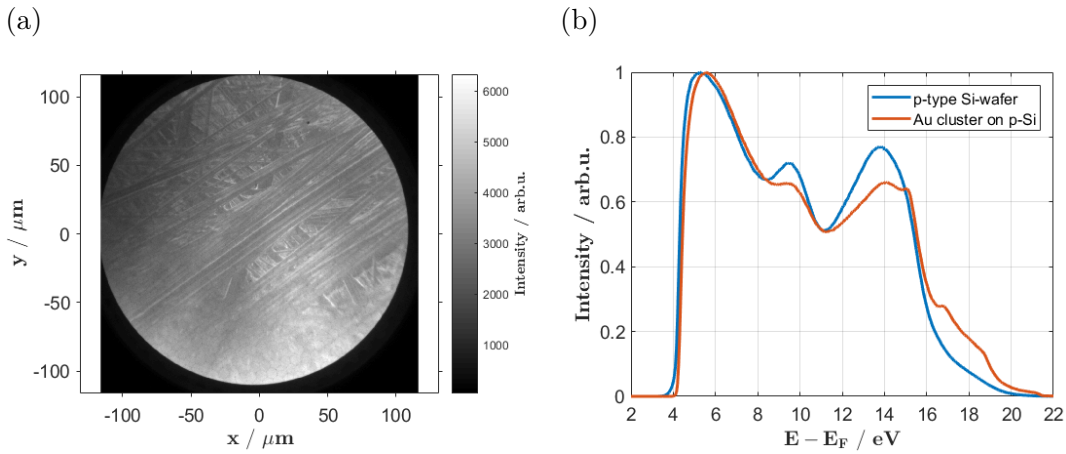

Figure 4.13: (a) PEEM image of the contaminated p-type Si-wafer. (b) UPS spectra of the pristine p-type Si-wafer and the deposited Au cluster region.

plasma cleaning, which was done for the ITO (indium tin oxide) samples later on. However, the UPS spectra reveal an unambiguous sign of Au cluster presence, especially the significant features in the UPS-signal above 15 eV can be assigned to the 5d valence band of gold. A further prominent sign of Au cluster deposition and the metallic character of the surface is the visible Fermi edge at 21.21 eV. Nevertheless, neither the nanoparticles nor an apparent contrast between the deposition and the Au cluster could be detected in the real space imaging mode.

The next step towards new plasmonic nanoparticles was to investigate ZnO clusters because of recent successful TEM (transmission electron microscope) results on Ag@ZnO core-shell particles fabricated with the helium synthesis approach. ZnO particles were again deposited on the p-type Si-wafer. The sample preparation was done in the same way as for the Au cluster deposition, but the surface revealed to be cleaner. Furthermore, no clear difference in contrast due to the deposition could be found. UPS-spectra were recorded at different sample positions and they show a clear sign of a ZnO deposition as shown in Fig. 4.14(a).

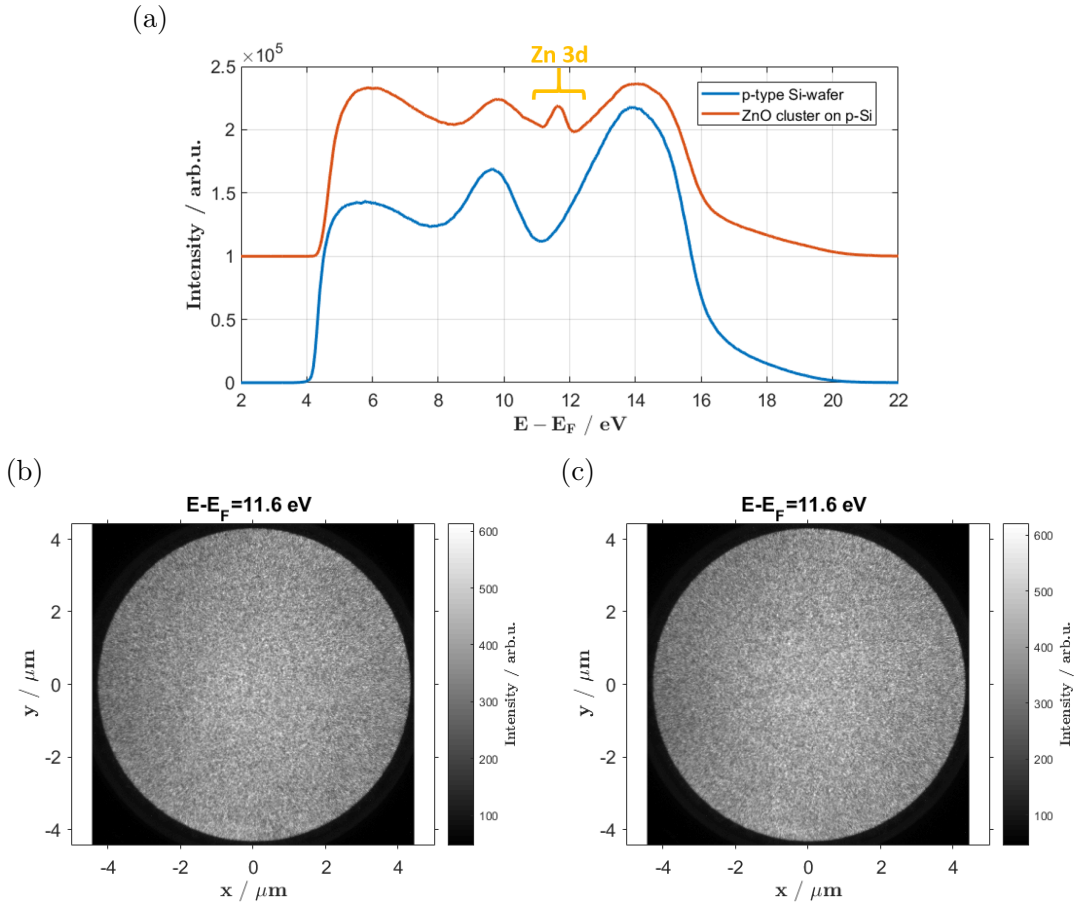

Figure 4.14: (a) UPS spectra of a pristine p-type Si-wafer and deposited ZnO cluster region. (b) EF-PEEM image of the corresponding ZnO region recorded at the binding energy of the Zn 3d core level. (c) EF-PEEM image of the corresponding pristine p-type Si-wafer region recorded also at the same energy showing no significant difference compared to (b).

The significant peak at 11.6 eV (corresponding to a binding energy of 9.6 eV) can be assigned to Zn 3d core level electrons according to the NIST XPS database [97]. However, the oxygen environment of the zinc atoms causes a core level shift, leading to a binding energy of approx. 10.5 eV according to the NIST XPS database. The difference between the expected and observed peak position may be explained by partial oxidation of the Zn with still some metallic Zn present, or the interference of the substrate [98]. Furthermore, EF-PEEM images were recorded at the energy of the Zn 3d core level in order to investigate the sample for a possible element specific contrast. Unfortunately, no significant difference between ZnO deposited regions and the pristine p-type Si-wafer could be detected, as depicted in Fig. 4.14(b) & (c). Considering the low kinetic energy cut-offs of the two UPS-spectra in Fig. 4.14(a), it seems that the pristine Si-wafer has a smaller work function than the ZnO region. However, according to Ref. [5], the determination of the work function calls for a small contrast aperture in order to obtain a sharp secondary electron peak. Therefore, the UPS-spectra around the cut-off region were also recorded using the contrast aperture of 150 μm (see Fig. 4.15(a)) showing a completely different behaviour of the two regions at low kinetic energies. Apparently, the cluster deposition causes a decrease in the work function by an order of approx. 0.2 eV, demonstrating, again, the importance of the contrast aperture. As for the Ag cluster deposition, this difference in work function can be used in the real space imaging mode in order to enhance the contrast between the ZnO and the substrate and, actually, Fig. 4.15(b) shows unambiguously a slight texture, which could possibly be attributed to the ZnO particles. In contrast to the bare Ag cluster, the ZnO particles do not agglomerate to such large structures, suggesting that ZnO is not as mobile as Ag on the silicon wafer. However, work function measurements on ZnO/silicon heterojunctions, fabricated by magnetron sputtering, showed values between 4.45 and 4.5 eV [99], which are in good agreement with the measurements Fig. 4.15(a) taken on ZnO clusters synthesized with the helium droplet approach.

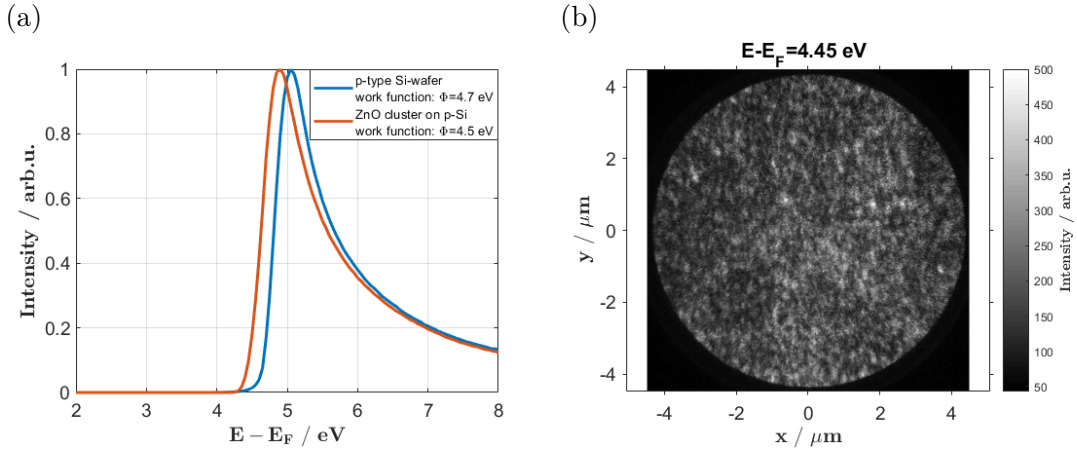

Figure 4.15: (a) The work function difference between the ZnO cluster region and the pristine p-type Si-wafer. (b) EF-PEEM image of the ZnO cluster region utilizing the work function contrast mechanism deduced from (a).

Furthermore, the NanoESCA instrument offers the possibility of creating work function maps. By recording images for energies around the cut-off region, stacking them on top of each other and fitting the secondary electron peak for each pixel with the sophisticated

fit model introduced by Ref. [5] and described in subsection 4.1.2 a work function map can be extracted from the EF-PEEM image sequence. For the same positions as in Fig. 4.15 such energy-scan experiments were carried out and the work function maps corresponding to the ZnO region (a) and the pristine p-type Si-wafer (b) are depicted in Fig. 4.16. Here, a considerable reduction of the work function due to high surface coverage of ZnO nanoparticles is visible. The regions with a low work function in Fig. 4.16(a) corresponds to the bright regions in the EF-PEEM image of Fig. 4.15(b). In Fig. 4.16(b) an unwanted characteristic of the energy-filtered mode can be seen, namely the so-called non-isochromaticity of the images, which means that different points in the image represent photoelectrons with different kinetic energies. [5] The tandem configuration of the hemispheres neutralizes the α^2-aberration term, which would otherwise deteriorate the lateral resolution [1, 5, 47]. However, the energy-filter still introduces a significant non-isochromaticity into an energy-filtered PEEM-image, which can be visualized and analyzed with the work function map. Hence, the work function mapping proved to be a valuable method not only for imaging the work function differences on the nanoscale but also for correcting possible energy shifts within an image as described in detail by Ref. [5].

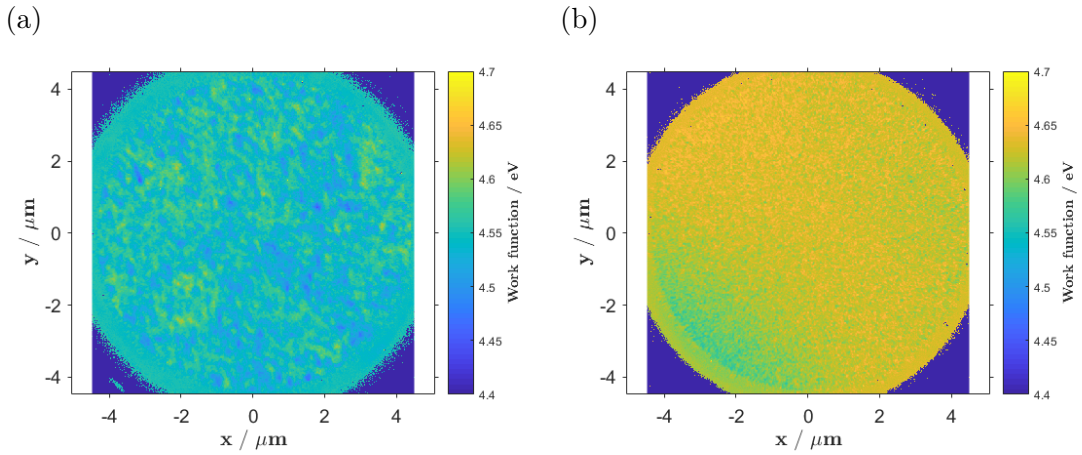

Figure 4.16: Work function maps of (a) the ZnO region and (b) the pristine p-type Si-wafer extracted from the same position as in Fig. 4.15.

Recent research at the institute has unveiled the applicability of the synthesis of novel oxide nanoparticles, such as vanadium pentoxide (V_2O_5), inside helium droplets. Mass spectroscopy measurements already demonstrated the preservation of the bulk stoichiometric ratio of vanadium to oxygen in He-grown nanoparticles. [100] A following publication [101] shows the preference of the pentoxide state for the deposited clusters by employing transmission electron microscopy and UV-VIS absorption spectroscopy. In order to evidence the pentoxide state for the deposited nanoparticles, several measuring techniques have been utilized including photoemission electron microscopy. The goal of the photoemission experiments was to provide a qualitative detection of the V_2O_5 by considering the electronic structure, such as the work function, the valence band maximum and the band gap. Indium tin oxide (ITO), a transparent conducting oxide surface, was used as the substrate material. Before depositing the clusters on the ITO, the surface was pre-characterized by the EF-PEEM in order to assure a reliable interpretation of the differences in the UPS-spectrum after deposition of V_2O_5. Six UPS-spectra of the exact same

positions were recorded before and after the synthesis of V_2O_5. This measurement procedure, consisting of a pre-characterization of the substrate and the following investigation of the deposited clusters, guarantees a qualitative comparison and is highly recommended if a UHV-cleaning of the substrate is not possible. The averaged UPS-spectra of the pristine ITO and V_2O_5 on ITO are depicted in Fig. 4.17(a). A slight work function shift towards higher energy can be seen for the ITO surface with vanadium pentoxide nanoparticles. Such an increase in work function was already demonstrated for V_2O_5 layers on ITO with increasing film thickness by Ref. [102]. For small amounts of deposited V_2O_5 the shift of the photoemission onset is associated with the formation of interface dipoles. The two spectra show hardly any differences, however in a more detailed examination one can observe for the V_2O_5 deposition a suppressed ITO signal around 17 eV and a slightly enhanced signal towards lower binding energies. Furthermore, by subtracting 80% of the

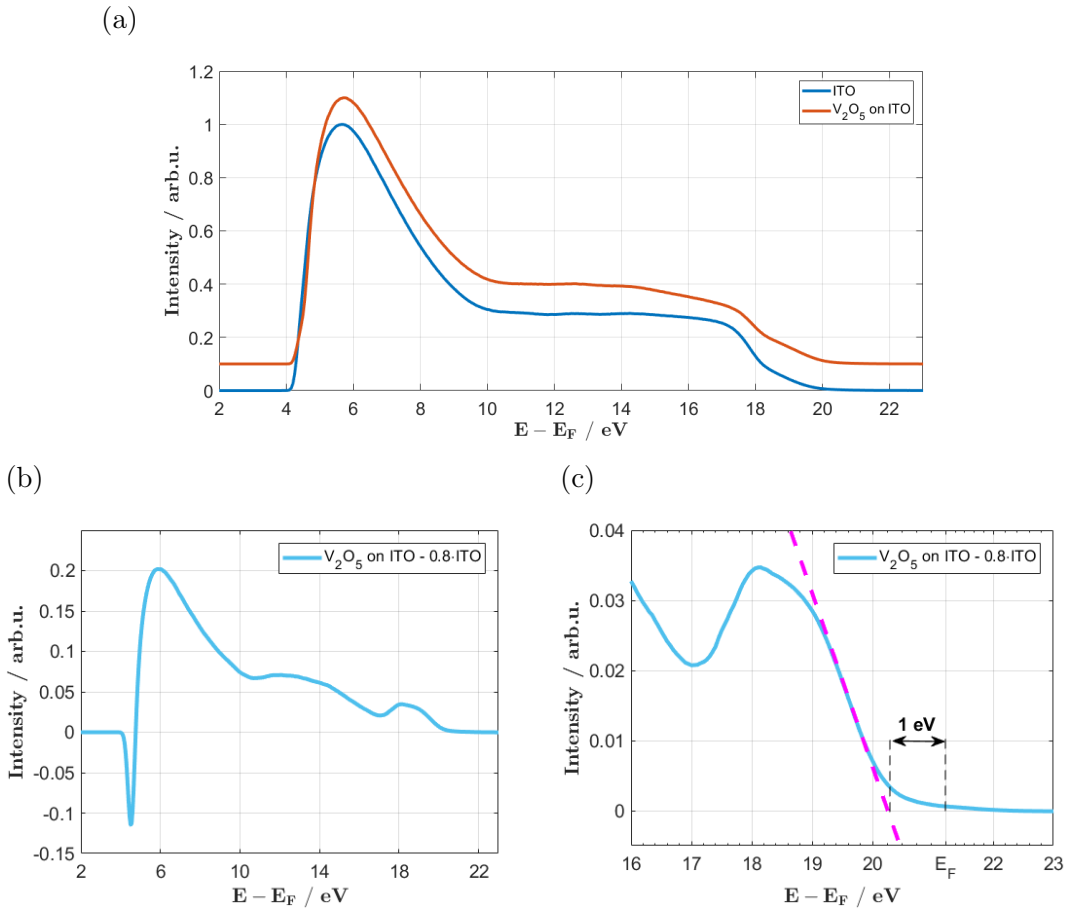

Figure 4.17: (a) Averaged UPS spectra of ITO and V_2O_5 particles deposited on ITO. (b) Difference of the two averaged UPS spectra. Note that 80% of the ITO photoemission signal was subtracted from the V_2O_5-ITO assembly. (c) Enlarged valence band region below the Fermi energy showing the possible indication of vanadium pentoxide (peak at 18.1 eV) and location of the valence band maximum (approx. 20.2 eV).

photoemission signal of the pristine ITO substrate from the V_2O_5-ITO assembly, these changes become clearer, see Fig. 4.17(b). Beside the already mentioned shift of the photoemission onset, a characteristic peak at around 18.1 eV can be seen, possibly indicating the occurrence of V_2O_5. [102, 103]. In Fig. 4.17(c) the region below the Fermi energy is shown enlarged for a closer inspection. According to DFT calculations (density functional theory) the peak at a binding energy of 3.1 eV is dominated by O 2p-derived band states with some V 3d contributions. [103] By applying a tangent at the descent of the valence band and locating its crossing with the baseline the valence band maximum can be determined to approximately 1 eV below the Fermi energy. Since V_2O_5 is proposed to be of p-type nature by density functional theory [103], the energetic distance between Fermi energy and the minimum of the conduction band has to be at least larger than 1 eV.

4.2.3 Conclusion and Outlook

In summary, this section shows the applicability of the NanoESCA instrument for the investigation of nanoparticles fabricated with the helium droplet synthesis approach and its major limitation in this context, the lateral resolution. In particular, one has to keep in mind that the observed PEEM images are always a convolution of the spatial resolution limit (approx. 40 nm) restricted by chromatic and spherical aberration, the real particle size and possible side effects, such as field enhancement. The substrate preparation also manifests as a drawback for the measuring technique. As long as the installation of the preparation chamber is unfinished and an UHV-cleaning of the substrate is infeasible, comprehensible interpretations about the electronic structure, such as work function, the valence band and band gaps, are difficult. However, throughout the series of experiments concerning nanoparticles many operating and preparing deficiencies were mostly eliminated, paving the way for future measurements with reasonable chances of success. ZnO and, moreover, Ag@ZnO core-shell particles are subject of ongoing research. For instance, the 3d core level peak gives a clear indication of the cluster deposition and furthermore, the ITO substrate proved to be useful in demonstrating the degree of oxidation by considering the core level shift of Zn upon oxygen exposure. Recent measurements also show a response of the silver core to the photoexcitation with the second harmonic of the nanosecond laser system Indigo-S. This effect could apparently be associated with the localized surface plasmon resonance. Consequently, future experiments will focus on the interaction of the plasmonic activity of the silver core with its ZnO environment by studying the wavelength position and the lifetime of the LSPR.

4.3 Mapping of Surface Plasmon Polaritons

In section 4.2 a specific type of plasmon oscillations was introduced, related to the topic of localised surface plasmons (LSP), which were described as collective oscillations of electrons confined in a nanoparticle. Another class of plasmons are surface plasmon polaritons (SPP), which correspond to propagating hybrid modes at the interface between a metal and a surrounding dielectric. Thus, SPPs exhibit a mixed character of a surface charge oscillation and an electromagnetic wave. [104,105] Considering the SPP dispersion curve, an excitation by light is not possible unless the momentum mismatch is compensated by special coupling methods such as grating couplers or excitation edges. [104] The exploitation of these phase-matching techniques can pave the way for promising applications in science and industry, such as surface-plasmon based circuits, merging the fields of photonics and electronics at the nanoscale. [106] Furthermore, highly confined electromagnetic energy carried by the SPPs can be focused by appropriately fabricated nanostructures [107] and be utilized for photocatalysis [82, 108] or molecular sensing [109] at the nanoscale. However, investigating these plasmonic phenomena requires novel experimental methods, such as two photon photoemission microscopy (2PPE PEEM), which has already shown its applicability in imaging SPPs at the surface of Ag films [110,111] and at Ag triangular structures [112]. In this regard, the NanoESCA instrument can fundamentally contribute to the exploration of SPPs, utilizing its good lateral and energy resolution. Moreover, the implementation of an interferometric pump-probe setup allows for nano-femto spatiotemporal studies. Last but not least, momentum microscopy has recently revealed as a powerful tool in discriminating between multiphoton photoemission processes and optical field emission. [113, 114]

Within the course of this Master's thesis several test structures provided by the Nano Optics group at University of Graz were investigated with the NanoESCA instrument. During this process, aluminium was chosen as an interesting plasmonic material, promising for further investigation. The cleaning process was optimized by introducing a plasma cleaning step after the fabrication of the nanostructures to get rid off organic residuals. A variety of different test structures, ranging from triangles to wave guides, showed the applicability of the NanoESCA instrument in imaging SPPs and guided the focus of future research especially on momentum related phenomena as long as the time resolution can not be further improved with the current available resources.
In this section, selective results of surface plasmon polariton mapping experiments obtained with aluminium triangles fabricated on an Al thin film-ITO-glass substrate assembly are presented, providing a good starting point for promising future research in the field of plasmonics.

4.3.1 Launching SPPs - ns vs. fs Laser System

Before introducing a detailed analysis of SPP-patterns launched in arrays of triangles, the two Ti:sapphire laser systems used in the course of this Master's thesis are compared to each other with respect to SPP imaging, focussing and power density. For both systems, the second harmonic with an average power of 5 mW was used. Additionally, polarization dependent measurements were carried out by using a $\lambda/2$-wave plate, showing that

the coupling of light into a SPP requires an electric field component perpendicular to an edge-defect [112].

In Fig. 4.18 the EF-PEEM images of the laser spots of the nanosecond and femtosecond laser systems and their corresponding beam profiles are depicted. Due to the grazing incidence geometry, both spots unveil an elliptical shape. The most prominent difference between the two EF-PEEM images, however, is the spot size originating mainly from the different optical paths. The fundamental fs beam is guided through a SHG unit, which has been set up and aligned in the course of the thesis, consisting of a BBO crystal and two quartz lenses. The first lens focuses the light onto the crystal for an efficient conversion, whereas the second lens behind the crystal compensates the beam divergence introduced by the first lens. Due to a different focal length and a rough alignment, the beam profile before entering the SHG unit could not absolutely be restored. The position of the final lens before the PEEM chamber was the same for both laser systems and, thus, the fs laser spot could not be focused as well as for the Indigo Ti:sapphire system. Furthermore, plotting the corresponding line profiles reveals Gaussian beam profiles for both laser systems. Note that the tails of the ns beam profile also indicate a slight Lorentzian character. In order to determine the power density of a light pulse, the spot diameter at the surface has to be estimated by determining the full width at half maximum (FWHM) from a Gaussian fit applied to the line profile. Considering the average power P_{av}, pulse duration t_{pulse}, repetition rate f_{rep}, the spot diameter d and

$$PD = \frac{4 \cdot P_{av}}{t_{pulse} \cdot f_{rep} \cdot \pi \cdot d^2}, \tag{4.3}$$

the power densities PD per pulse can be evaluated in the case for the ns laser to $1 \cdot 10^9$ mW/cm^2 and for the fs laser $2 \cdot 10^9$ mW/cm^2. However, this procedure should only serve as a rough guess for the power densities because several influences have been neglected, such as the underlying photoemission process, the non-linear dependence of the photoemission intensity on the laser power and, furthermore, only one specific energy was considered.

In Fig. 4.19, 2PPE-EF-PEEM images of equilateral triangles with 30 μm side length are depicted, illuminated with different laser systems and polarization angles. Additionally, a schematic is shown in Fig. 4.19(a) explaining the definition of s- and p-polarization at the sample surface and the resulting in-plane components of the electric fields. Furthermore, the schematic subdivides the PEEM images into the corresponding polarization of the incoming laser light, i.e. the left half corresponds to illumination with p-polarized light and the right one with s-polarized light. The in-plane direction of the incoming laser light is indicated in Fig. 4.19(b). As already mentioned above, a detailed analysis of SPP-patterns launched in arrays of triangles is introduced in the following subsection 4.3.2. Here, a brief discussion about the formation of these interference patterns and their dependence on the light polarization is given, providing the basics for the upcoming analysis. According to Ref. [112], laser pulses excite an SPP wave at the edge of a triangle, while a second photon from the same laser pulse triggers the photoemission process. However, the launched SPP wave interferes with the light wave of the laser, creating the observed beat pattern, a so-called moiré pattern. Consequently, the resulting plasmon-enhanced

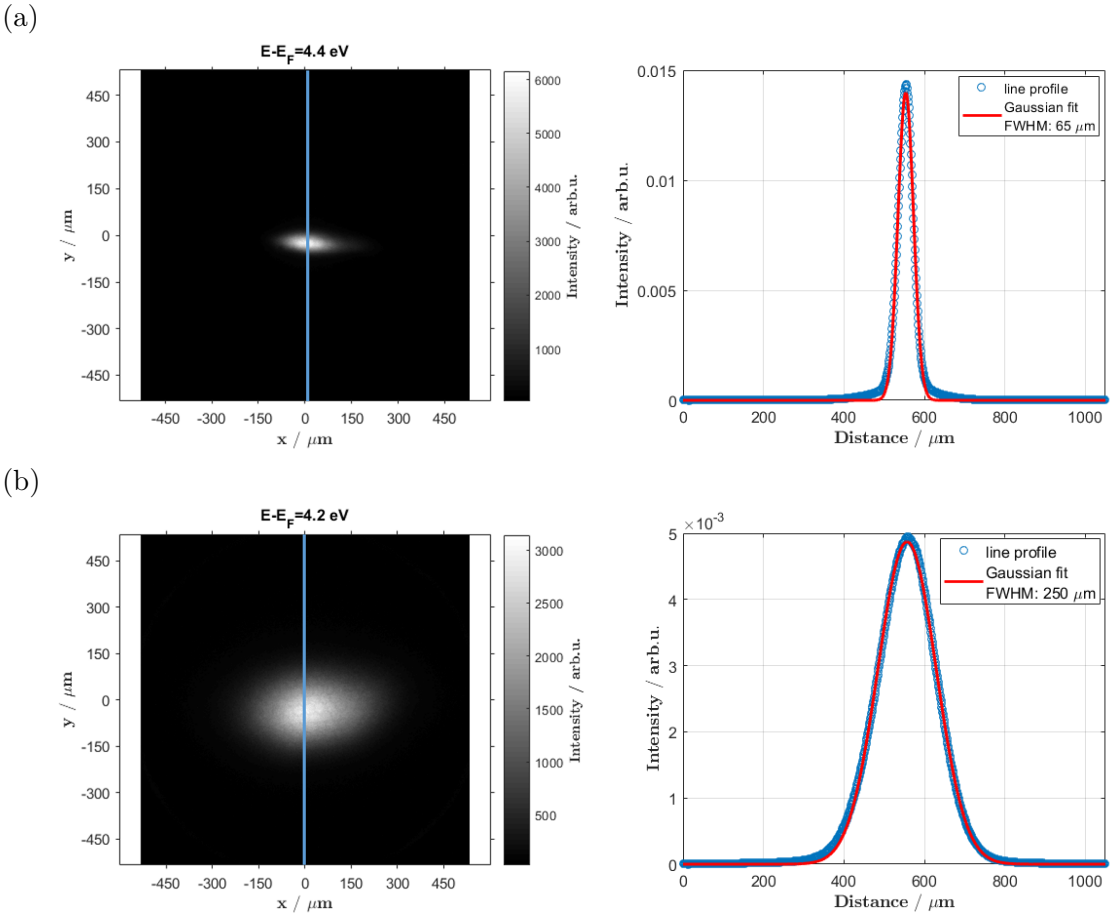

Figure 4.18: 2PPE-EF-PEEM images of the (a) nanosecond and (b) femtosecond laser spots and their corresponding Gaussian beam profiles. A power density of approx. (a) $1 \cdot 10^9$ mW/cm^2 and (b) $2 \cdot 10^9$ mW/cm^2 can be roughly deduced.

photoemission yield Y_{2PPE} can be described by the fourth power of the time-integrated superposition of the two electric fields:

$$Y_{2PPE} = \int \left(\mathbf{E_1}(\mathbf{x}, t) + \mathbf{E_2}(\mathbf{x}, t)\right)^4 dt. \tag{4.4}$$

Considering the 2PPE-EF-PEEM images for both laser systems recorded with p-polarized light in Fig. 4.19(b,c), at the front edge of the triangle (i.e. the part which is first hit by the laser pulses) a SPP wave is generated, propagating parallel to the in-plane component of the light wave vector, which interferes with the light wave and creates the moiré pattern observed in the 2PPE image. Furthermore, at the two other triangle sides also SPPs are launched, propagating on the Al thin film away from the triangle, which is hard to see in Fig. 4.19(b,c). For s-polarized light, however, the 2PPE-images do not exhibit such beat patterns, verifying that an in-plane electric field component perpendicular to an edge-defect is necessary to initiate an SPP wave. However, when properly adjusting the grey scale of the photoemission intensity one can see a weak pattern, possibly originating

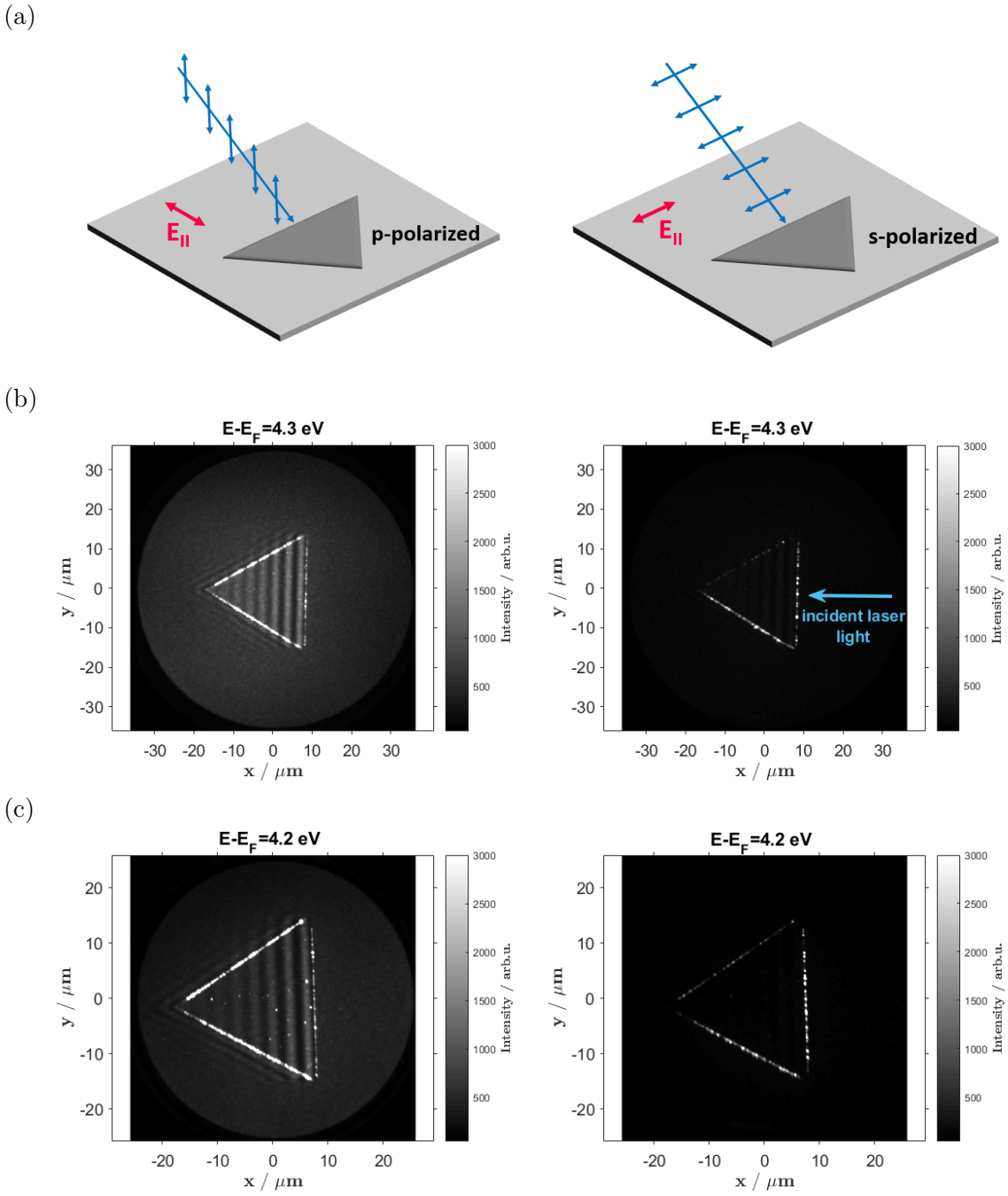

Figure 4.19: (a) Schematic showing the definition of p- and s-polarization for the present experimental setup and the resulting in-plane components of the electric field $\mathbf{E}_{\parallel}$. (b) 2PPE-EF-PEEM image of a 30 μm triangle acquired with the nanosecond laser Indigo-S for p- and s-polarized, respectively. (c) 2PPE-EF-PEEM image of a 30 μm triangle acquired with the femtosecond laser for p- and s-polarized, respectively. In the case of p-polarized light a superposition of SPP and light wave, called moiré pattern, can be observed. For a detailed description the reader is referred to the text.

from a slight deviation from the ideal polarization. Note that due to the grazing incidence configuration, it is hard to define a specific polarization angle, as the sample experiences always an electromagnetic field of mixed character between p- and s-polarization. Comparing the two different laser systems with respect to the image quality to each other, the image acquisition with the nanosecond laser Indigo-S takes only about 10 s, whereas with the femtosecond laser, as shown in Fig. 4.19(c), it takes 30 summed images with 10 s integration time each in order to gain a comparable quality. This is in contrast to the fact that according to channeltron measurements the counts per second at the maximum of the secondary electron peak obtained with the femtosecond laser exceeds the counts acquired with the Indigo-S. This dependence of the photoemission yield on the laser source has been observed for several sample systems and can mainly be associated with space charge effects. [67] High photon densities, confined on a small area on the sample surface (i.e. laser spot size), lead to the emission of a high density of photoelectrons. Due to Coulomb repulsion, the ejected electron cloud expands energetically and laterally, which results in a broadening of the kinetic energy distribution and an image blur, as illustrated in Fig. 4.20. Due to the low repetition rate of the nanosecond Ti:sapphire oscillator (5 kHz), space charge effects are very likely to occur already at low average powers since more photons are compressed into fewer pulses by maintaining the same average laser intensity.

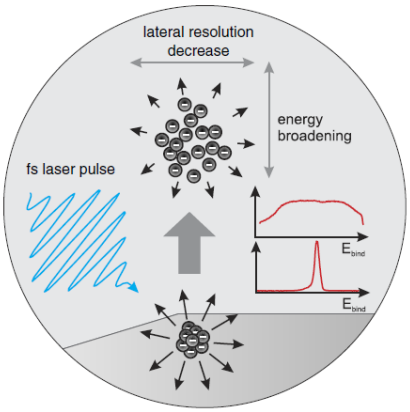

Figure 4.20: Illustration of space charge effects and their impact on PEEM measurements. The Coulomb repulsion of the photoelectron cloud leads to a broadening of the kinetic energy distribution of the photoelectrons and, thus, to an image blur. Taken from Ref. [67]

Thus, the analysis of the photoelectron's original kinetic energy is more or less impossible due to the broadening of the kinetic energy distribution. As already mentioned, the laser pulses of the Ti:sapphire laser Indigo-S causes this energy broadening in the spectroscopy mode, leading to a reduced number of counts at the secondary electron maximum since the photoelectrons are distributed over a broad range of the kinetic energy spectrum. In the energy-filtered microscopy mode, however, neither an image blur nor the energy spread can be observed, suggesting that the location, at which the most severe Coulomb repulsion takes place in the PEEM, has to be in the microscope column. This hypothesis has to be further investigated, as it could reveal a huge advantage of the NanoESCA over comparable PEEM systems, related to the topic of spectromicroscopy with amplified ultrafast laser systems.

4.3.2 Multiple SPP-Generation in Al Triangle Arrays

As already described above, the observed pattern in the 2PPE-EF-PEEM image corresponds to the superposition of an SPP wave launched at an edge defect and the light field of the laser pulse. This moiré effect was also investigated in arrays of 3 μm triangles with the nanosecond pulsed laser light at a wavelength of 385 nm. As the set of equally oriented triangles rotates, beating patterns of different directions and fringe spacings appear. Simple geometric considerations, exploiting the vectorial character of the waves according to Ref. [112], deliver an appropriate explanation and theoretically reproduce the experimental results of the beating wavelengths.
The following theoretical interpretation is based on Ref. [112], providing a plausible agreement between experimental observation (Fig. 4.21 - 4.23) and calculation (Fig. 4.24). Fig. 4.21 shows a first array of equally oriented 3 μm triangles. The 2PPE-PEEM images in (b) and (c) reveal two dominant beating patterns launched at the two front edges of the triangles.

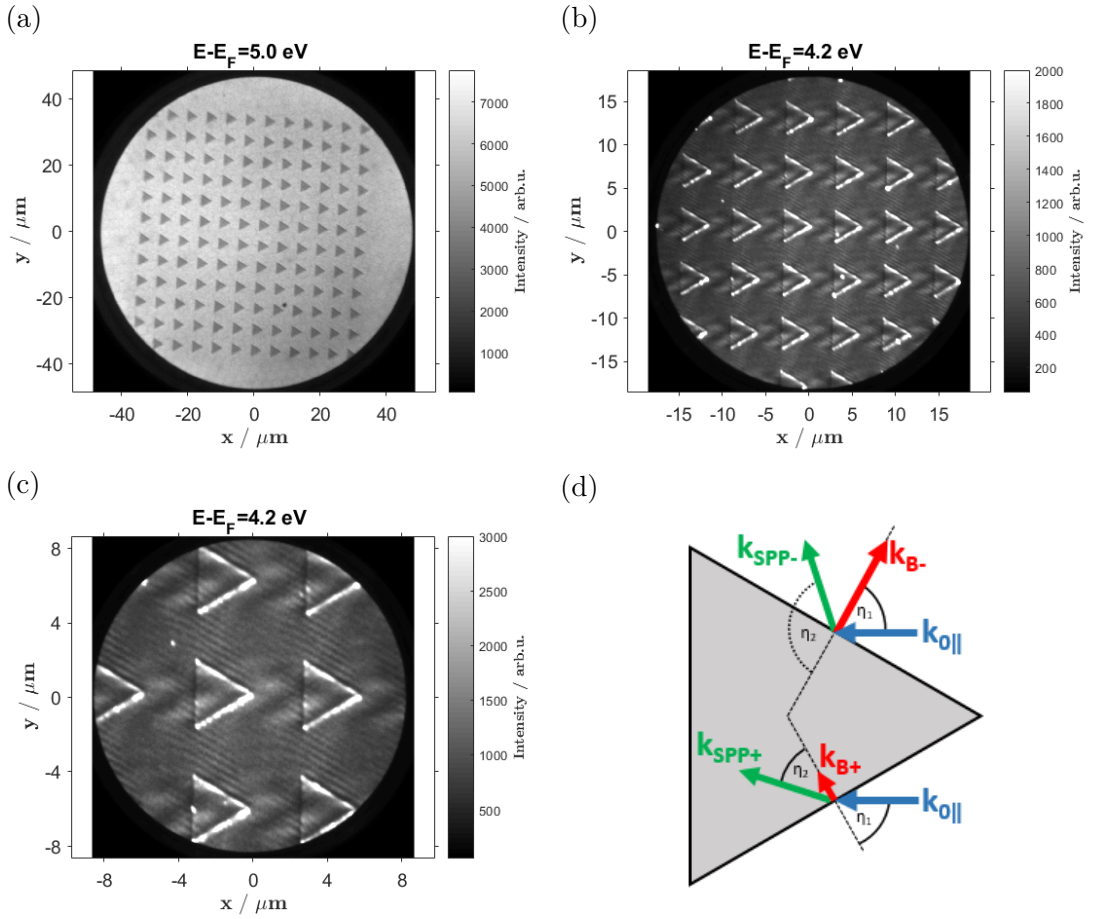

Figure 4.21: (a) EF-PEEM image of a 3 μm triangle array recorded with the helium discharge lamp. (b,c) The corresponding 2PPE-EF-PEEM and (d) a schematic explaining the observed patterns and their vectorial wave components. For a detailed description the reader is referred to the text.

In order to describe the periodicities, the in-plane components of the wave vectors have to be considered as indicated in (d). $\mathbf{k_{0\parallel}}$ is the wave vector of the exciting light wave, projected onto the surface plane, $\mathbf{k_{SPP}}$, the wave vector of the SPP and $\mathbf{k_B}$, the wave vector of the moiré pattern, which fulfil the condition

$$\mathbf{k_B} = \mathbf{k_{SPP}} - \mathbf{k_{0\parallel}}. \tag{4.5}$$

The wave number k_{SPP} is given by the wave number of the incident light k_0 and the dielectric functions of the interface between Al $\epsilon_1(385\ \mathrm{nm}) = -22$ [115] and vacuum $\epsilon_2 = 1$ according to Ref. [104] as

$$k_{\mathrm{SPP}} = k_0 \cdot \sqrt{\frac{\epsilon_1 \epsilon_2}{\epsilon_1 + \epsilon_2}} \approx 1.024 \cdot k_0. \tag{4.6}$$

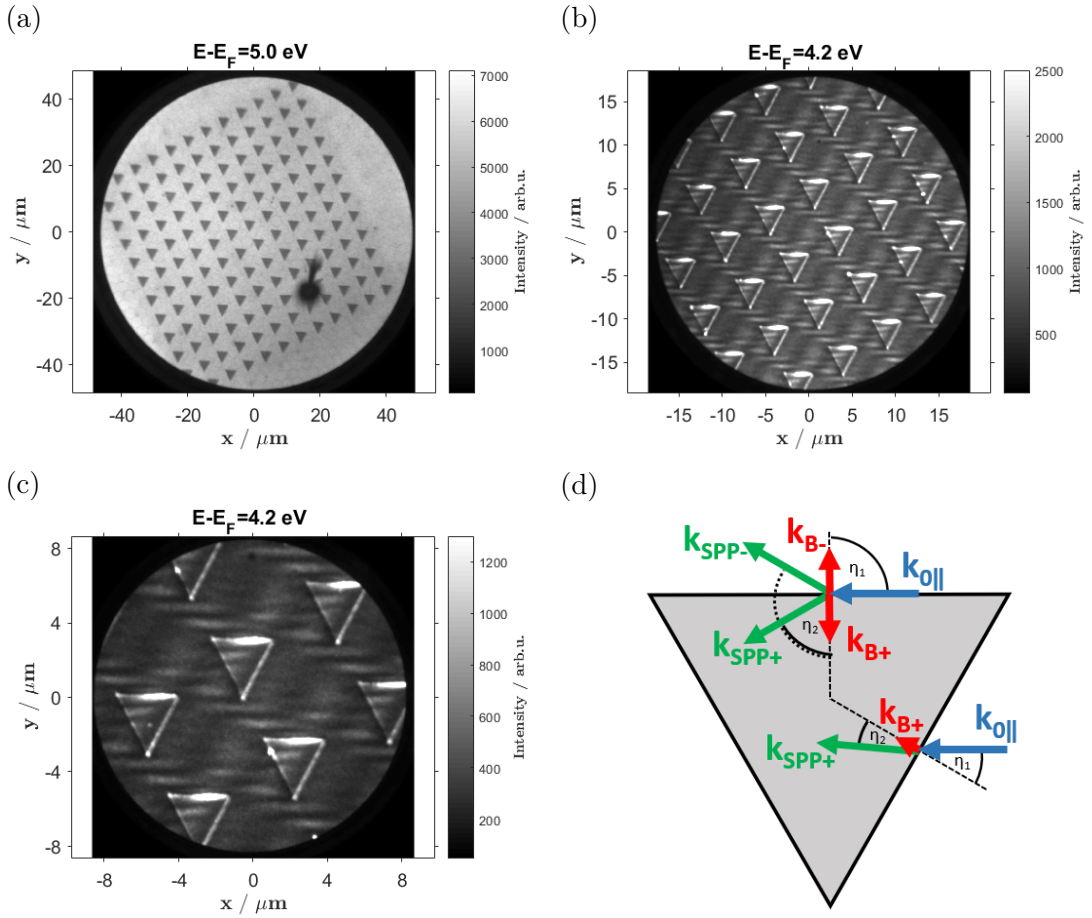

Figure 4.22: (a) EF-PEEM image of a 30° rotated 3 μm triangle array recorded with the helium discharge lamp. (b,c) The corresponding 2PPE-EF-PEEM and (d) a schematic explaining the observed patterns and their vectorial wave components. For a detailed description the reader is referred to the text.

Since $\mathbf{k_B}$ is obviously perpendicular to a triangle edge, a coordinate system can be chosen by aligning the x-axis along a triangle edge utilizing the disappearance of the x-component

of $\mathbf{k_B}$. Consequently, the direction of the SPP wave η_2 can easily be determined from the angle of incidence η_1 relating to Snell's law of refraction

$$k_{0\parallel} \cdot \sin \eta_1 = k_{\mathrm{SPP}} \cdot \sin \eta_2. \tag{4.7}$$

If $\eta_2 > 90°$, SPP waves and the resulting beating patterns are denominated as $\mathbf{k_{SPP-}}$ and $\mathbf{k_{B-}}$. Finally, the moiré fringe spacing $\lambda_{B+,-}$ can then be calculated either by directly solving eq. 4.5 or by

$$\lambda_B = \frac{\lambda_{0\parallel} \cdot \lambda_{\mathrm{SPP}}}{\sqrt{\lambda_{0\parallel}^2 + \lambda_{\mathrm{SPP}}^2 - 2\lambda_{0\parallel}\lambda_{\mathrm{SPP}} \cdot \cos(\eta_1 - \eta_2)}}. \tag{4.8}$$

As the azimuthal orientation of the triangles changes by 30° and 60°, new and already known beating patterns appear as depicted in Fig. 4.22 and Fig. 4.23. By examining the 2PPE-EF-PEEM images in detail, one might legitimately ask why only certain moiré patterns can be observed instead of six corresponding to two SPP waves launched at one triangle edge. One reason could be that some of the SPP waves do not propagate so far

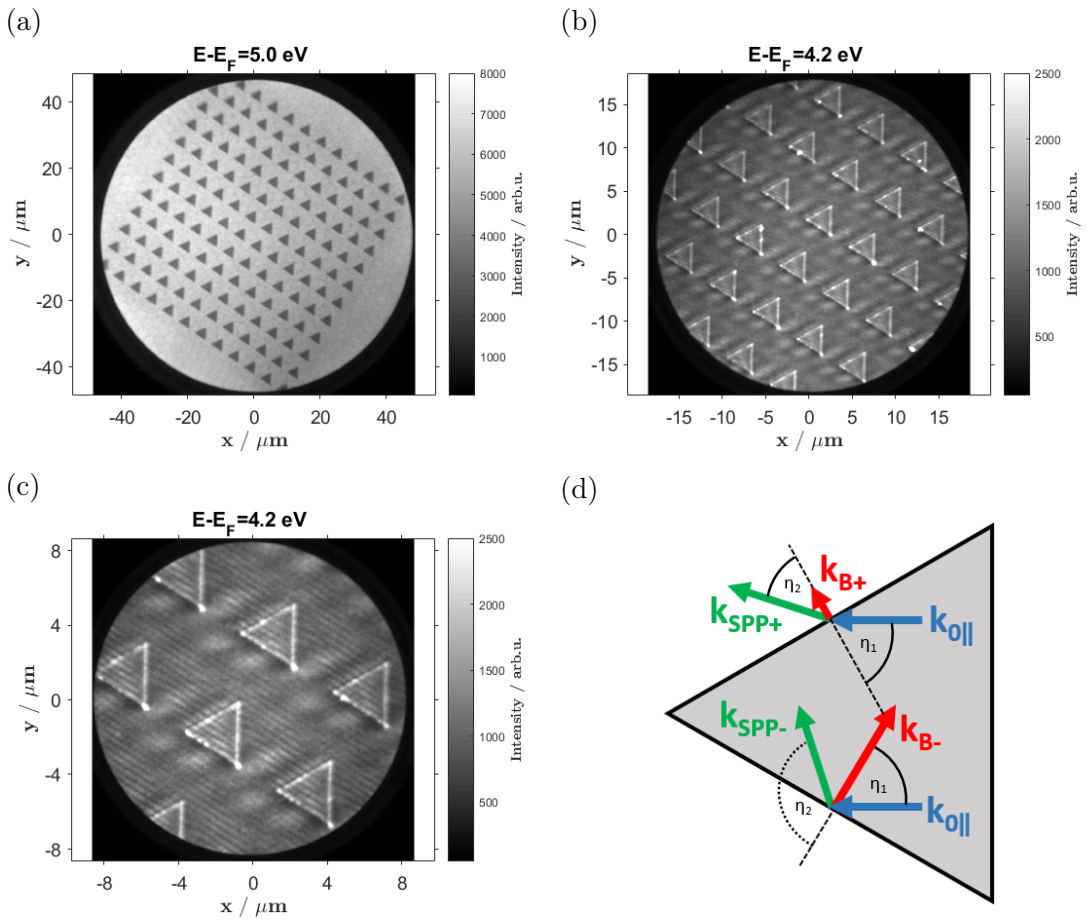

Figure 4.23: (a) EF-PEEM image of a 60° rotated 3 μm triangle array recorded with the helium discharge lamp. (b,c) The corresponding 2PPE-EF-PEEM and (d) a schematic explaining the observed patterns and their vectorial wave components. For a detailed description the reader is referred to the text.

as others due to a faster decay or, more unlikely, certain interferences of SPP and light wave do not result in a sufficiently high photoemission intensity in order to observe them. Smaller fringe spacings, possibly, could not be resolved due to insufficient adjustment of the electron optics. In the worst case, the beating patterns interfere with each other in such a way that a clear assignment is not possible any more. However, the wavelengths of the clearly assignable moiré patterns were roughly measured and plotted with the theoretical prediction for the Al-vacuum interface, see Fig. 4.24, showing a good agreement with the experiment. The beating wavelengths are separated according to the pre-described annotation of $\lambda_{B+} \; \forall \; \eta_2 \leq 90°$ and $\lambda_{B-} \; \forall \; \eta_2 > 90°$. A further aspect has been neglected throughout this section covering the influence of the oxidation of the Al thin film and triangles on their plasmonic activity. Since the sample was transported under ambient conditions, an Al_2O_3 thin film was very likely formed at the surface. However, the agreement of the experimental results with the calculated moiré fringe spacing based on an Al-vacuum interface unambiguously demonstrates an inferior impact of the oxidation layer on the generation and propagation of surface plasmon polaritons.

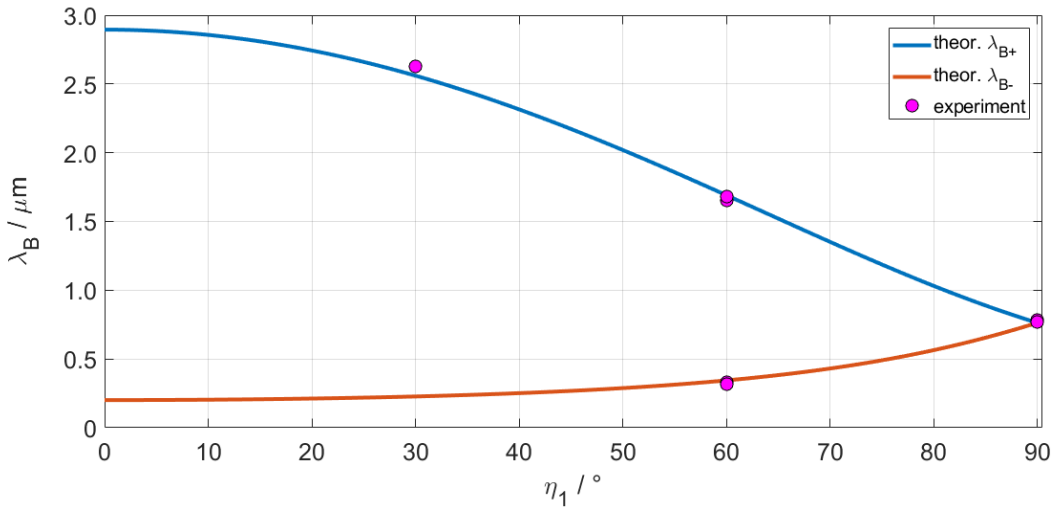

Figure 4.24: Moiré fringe spacing λ_B as a function of the incident angle η_1 and the experimental results extracted from the 2PPE-EF-PEEM images.

4.3.3 Momentum Microscopy on Lithographed Surfaces - An Outlook

Recent research revealed momentum microscopy as a powerful tool, not only in imaging the angular emission distribution of electrons excited from nanostructured surfaces, but also in discriminating between multiphoton photoemission processes and optical field emission [113, 114]. Consequently, a particular goal of the collaboration with the Nano Optics group was also to exploit the capability of the NanoESCA instrument in investigating momentum related phenomena of nanostructured surfaces. First promising results were thereby obtained by Al wave guides fabricated as horizontal converging stripes with a gap ranging from approx. 305 nm to 458 nm. EF-PEEM images of these wave guides recorded with the helium discharge lamp are depicted in Fig. 4.25(a).

By illuminating these wave guides with the s-polarized second harmonic (402.5 nm) of the Indigo-S laser system, light couples into the structure where the gap distance coincides with the wavelength of the light, producing an enhanced photoemission signal as shown in Fig. 4.25(b). It was also planned to build slightly rotated structures, unfortunately something went wrong in the lift-off process of the lithography fabrication and, hence, only the wave guide in the center of the images can be investigated. Furthermore, the failed structures turned out to be hot spots in the photoemission process, restricting the image quality, as seen in Fig. 4.25(b). In a future measurement, the light coupling process will be further studied by tuning the wavelength of the Indigo-S laser on the one hand to prove the working principle of the grating couplers and on the other hand, based on this result, to investigate the position dependence of the enhanced photoemission signal on the wavelength of the incident light.

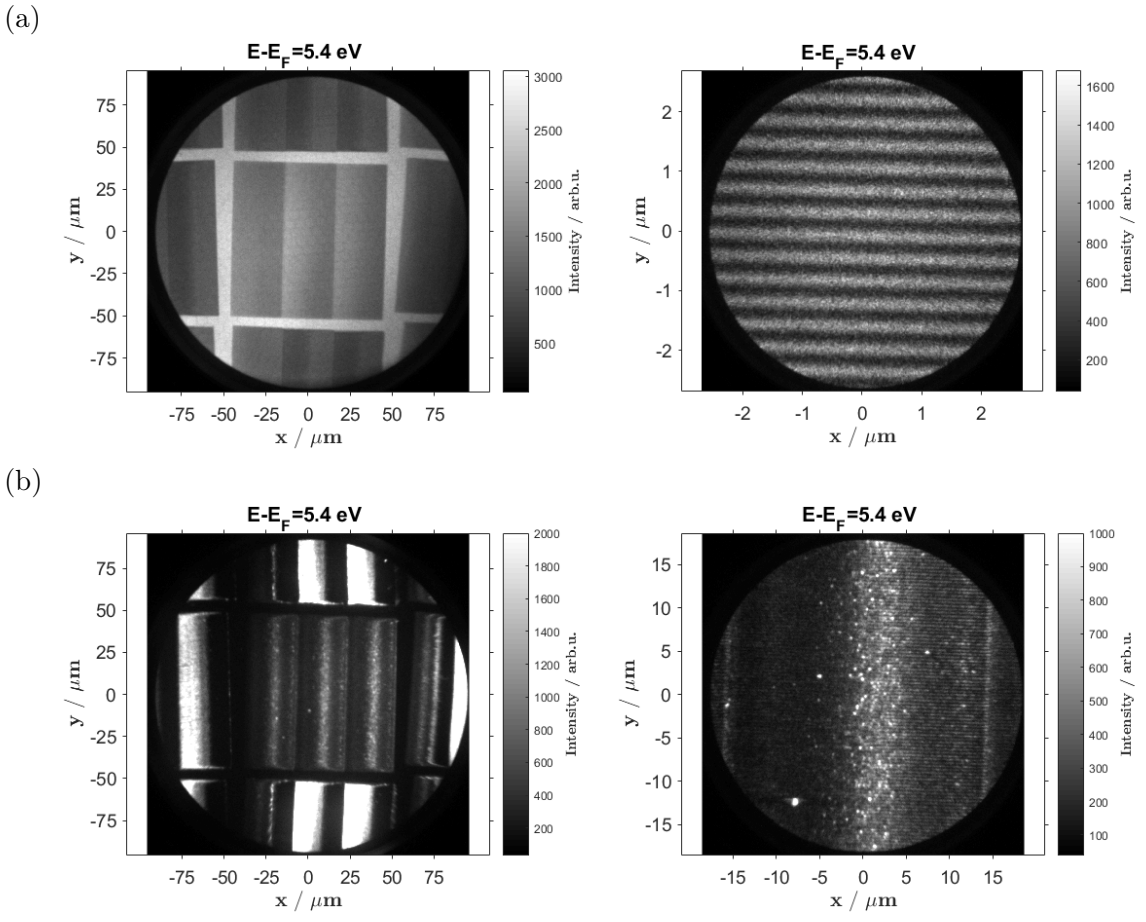

Figure 4.25: (a) EF-PEEM images of the Al wave guides for two different magnifications recorded with the helium discharge lamp. (b) 2PPE-EF-PEEM images of the Al wave guides showing an enhanced photoemission signal where the gap distance coincides with the wavelength of the s-polarized light of the Indigo-S laser system.

However, the more interesting characteristic of this grating coupling system appear in the momentum space, as depicted in Fig. 4.26. A distinct anisotropy of the photoemission horizon can be observed, showing a preferred angular direction of the photoexcited electrons. In particular, the normal emission signal is significantly decreased, whereas the majority of the electrons ejected from this structured surface form the two half shells, as seen in the PAD (photoemission angular distribution) patterns. Furthermore, the energy-momentum dispersion along the $k_{\parallel,y}$-direction reveals an increased photoemission intensity at the vicinity of the surface of the imagined free-electron parabola, see Fig. 4.26(b). The reason for this preferred angular emission can be explained by considering the electrical field of the s-polarized pulses. As illustrated in Fig. 4.26(c), the in-plane oscillating field induces a dipole between two ridges attracting the photoexcited electrons and, consequently, forcing them to leave the surface under this observed direction.

These wave guides are subject to current research and the investigation of these photoemission phenomena, briefly introduced here, is not complete yet. Further polarization and power dependent measurements will be carried out in the near future. However, this example shows the great potential of momentum microscopy with the NanoESCA instrument paving the way for promising research of photoemission processes of nanoscaled structures fabricated by electron beam lithography.

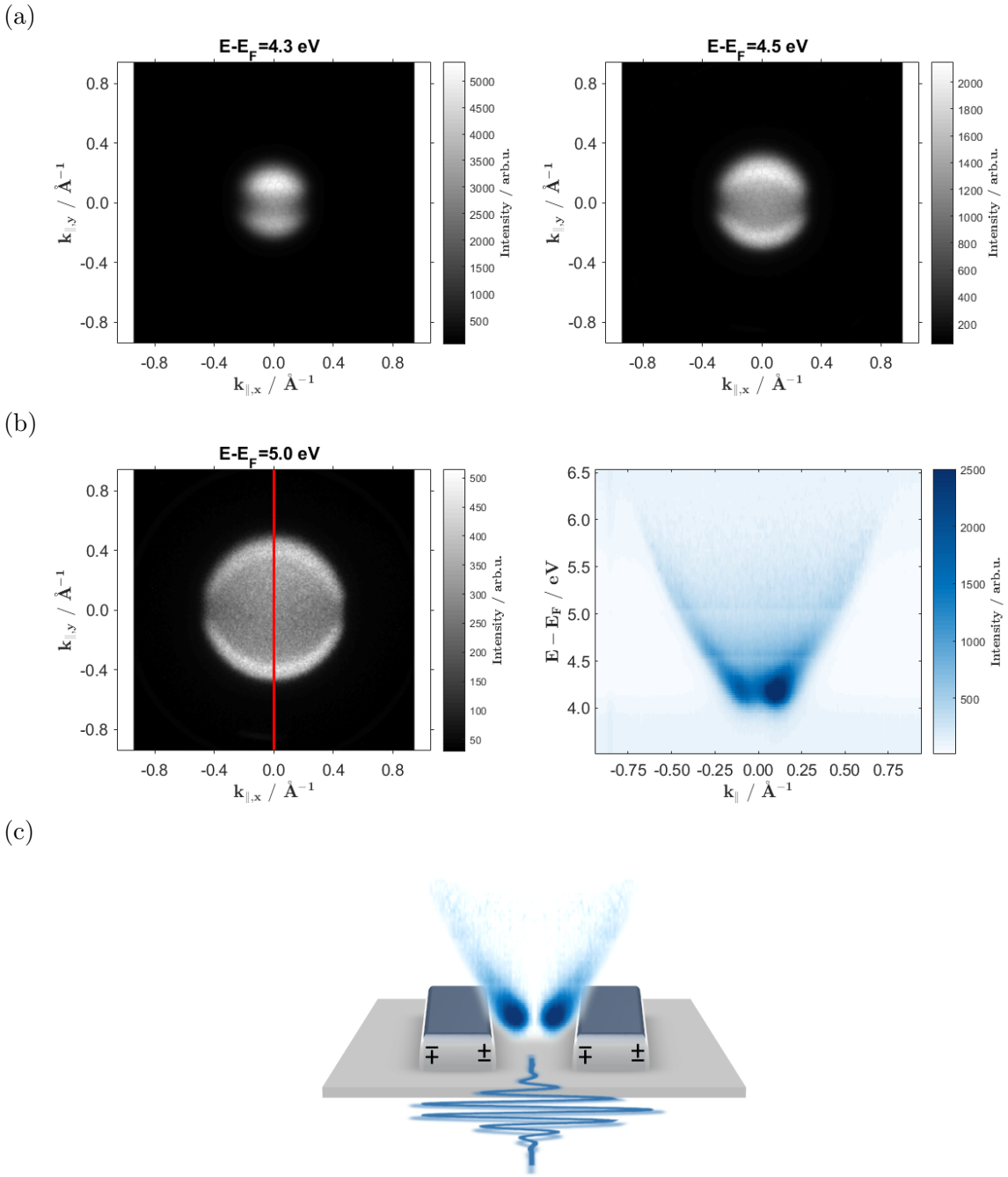

Figure 4.26: (a) 2PPE-EF-PEEM momentum images of the Al wave guides acquired with s-polarized light of the Indigo-S laser. (b) An additional PAD (photoemission angular distribution) pattern and the corresponding extracted energy-momentum dispersion along the indicated direction (red line) of the PAD pattern. (c) Schematic explaining the origin of the preferred angular emission. The s-polarized pulses induce dipoles between the ridges attracting the photoexcited electrons and, finally, forcing them to leave the surface under this observed direction.

4.4 Towards Time-Resolved Photoemission Electron Microscopy

Advances in ultrafast laser technology have driven science to develop experimental methods tackling the challenge of unravelling femtosecond dynamics in multiple dimensions, such as space, time, energy, momentum and spin. Among several methods for ultrafast microscopy, time-resolved photoemission electron microscopy emerges as a promising, versatile technique, capable of visualizing ultrafast electron dynamics at metal and semiconductor surfaces in a nanoscale spatial dimension [116]. Limited only by the duration of the laser pulses, the temporal resolution can in principle reach the attosecond domain [4], providing a further major advantage among other competing ultrafast microscopy techniques. As already mentioned in this thesis, the very first intention has been the introduction of a femtosecond laser setup, allowing for studies of dynamic processes in combination with the NanoESCA instrument. Towards implementation, however, several challenges arose, some of which proved to be intractable with the available resources. This section summarizes the achievements so far and, furthermore, shows the current obstacles which have to be overcome in the near future in order to do competitive research in the field of time-resolved photoemission electron microscopy.

At first, a brief introduction of the experimental approach in finding spatial and temporal overlap of the laser pulses is given by using a pristine region of the lithographed Al thin film sample and the second harmonic of the Ti:sapphire Vitara oscillator. In the employed interferometric pump-probe setup (Fig. 3.12), the second harmonic laser pulses are equally separated into a variable and a static path by a beam splitter and, finally, reunited collinearly with a second beam splitter. Before coupling the light into the NanoESCA instrument pre-adjustments of the interferometric setup are done on the optical table in order to assure the spatial overlap at the two terminal positions of the delay stage. After appropriate focusing of the laser pulses at the sample surface with the help of the channeltron and the real space mode, the spatial overlap can be further improved by refining the second beam splitter. An example for a good spatial overlap is shown in Fig. 4.27(a).

The next step is to locate the temporal overlap of pump and probe pulse. By using the spectroscopy mode one can record the area integrated counts depending on the delay stage position. If the travel range and the step increment is chosen properly, the autocorrelation trace can be obtained, giving the position of the temporal overlap, as depicted in Fig. 4.27(c) for a rather rough pump-probe delay scan. The autocorrelation trace carries information about the laser pulses and, furthermore, about coherent and incoherent processes, which will be discussed in more detail later on. However, the oscillating curve around the temporal overlap in Fig. 4.27(c) originates mainly from the interference between pump and probe pulse. As the pump-probe setup is not exactly collinear [117], a striped pattern of interference fringes can be observed in the real space mode, see Fig. 4.27(b). Note that in case of Fig. 4.27(c) a smaller field of view was used emphasizing additionally the dramatic variation of intensity since the fringe pattern moves through the selected area as the delay time changes.

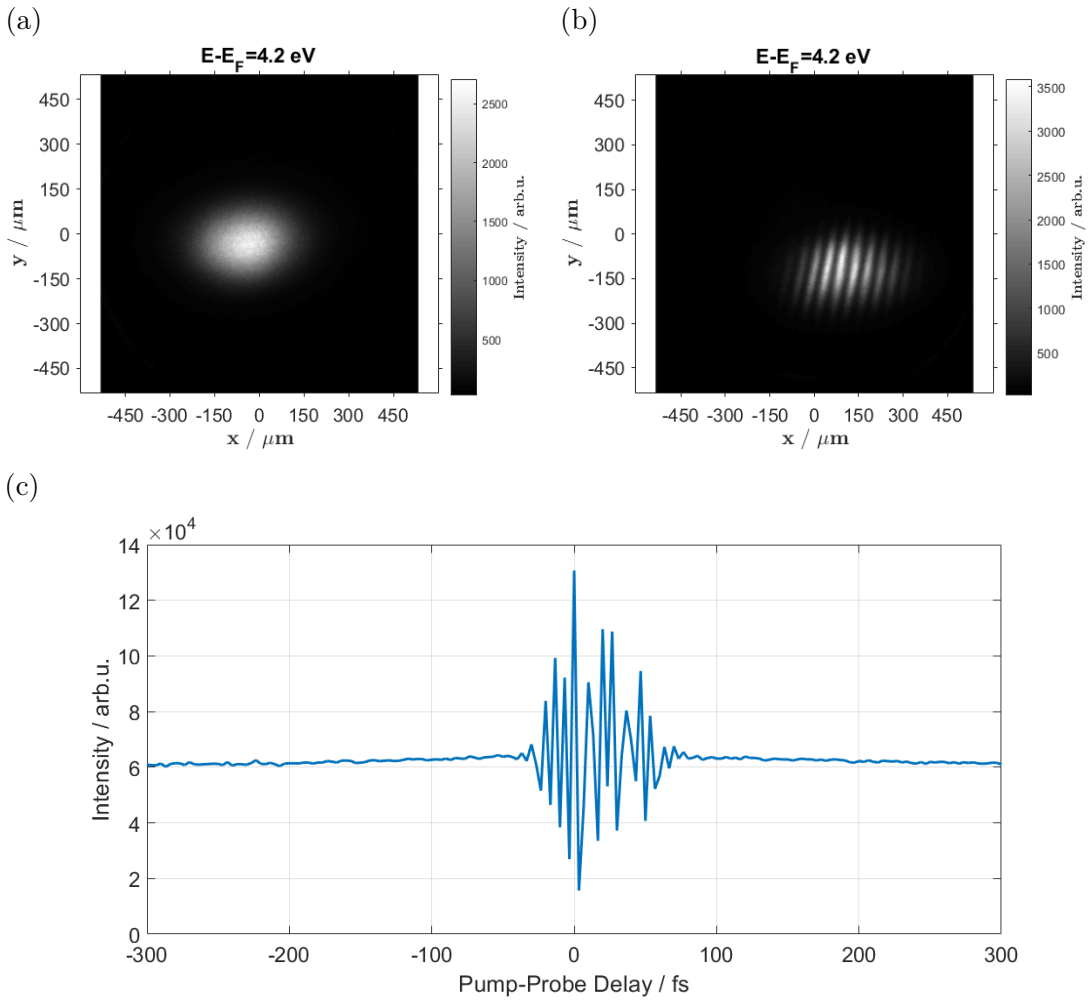

Figure 4.27: (a) 2PPE-EF-PEEM image of the spatially overlapped pump and probe pulses on an Al thin-film surface. (b) 2PPE-EF-PEEM image of the spatially and temporally overlapped pump and probe pulses. (c) Roughly measured autocorrelation trace, giving information about the delay stage position at the temporal pump-probe overlap.

As previously mentioned, the measured autocorrelation trace carries information about the laser pulses and dynamic processes at the surface. Strictly speaking, the so-called interferometric 2-pulse autocorrelation trace of photoemission, the finite material response, is a convolution of the interferometric autocorrelation trace of the laser pulses and the energy and phase relaxation mechanisms at the surface. [118]. The interferometric autocorrelation, often called phase-sensitive or fringe-resolved autocorrelation, was introduced by Jean-Claude Diels [119] and covers an intensity vs. delay measurement of the second harmonic light created by an SHG crystal placed at the output of a Michelson interferometer. [120]. By using collinear beams the second harmonic light generated by the interaction of the two different beams can combine coherently and, consequently, interference fringes, depending on the pulse delay, occur. The employed setup in Fig. 3.12 is also capable of performing such autocorrelation measurements since the two beams travel

through the same amount of refractive elements (beam splitters) maintaining the phase and, furthermore, the coherence, which is a requirement for interference to take place. The interferometric autocorrelation $I_{IAC}(\tau)$ can be expressed as

$$\begin{aligned} I_{IAC}(\tau) &= \int_{-\infty}^{\infty} |\left[E(t) + E(t-\tau)\right]^2|^2 dt \\ &= \int_{-\infty}^{\infty} |E(t)^2 + 2E(t)E(t-\tau) + E(t-\tau)^2|^2 dt, \end{aligned} \tag{4.9}$$

with $E(t)$ as the electric field of the laser pulses and τ as the time delay between the pulses introduced by the Michelson interferometer. Expanding this expression according to Ref. [120]:

$$\begin{aligned} I_{IAC}(\tau) = &\int_{-\infty}^{\infty} \{I(t)^2 + I(t-\tau)^2\} dt \\ &+ \int_{-\infty}^{\infty} \{I(t) + I(t-\tau)\} \,\mathrm{Re}\{E(t)E^*(t-\tau)\} dt \\ &+ \int_{-\infty}^{\infty} \mathrm{Re}\{E(t)^2 E^*(t-\tau)^2\} dt \\ &+ \int_{-\infty}^{\infty} I(t)I(t-\tau) dt. \end{aligned} \tag{4.10}$$

Summarizing, the interferometric autocorrelation trace is decomposed of (first line of Eq. 4.10) a constant, (second line) the interferogram of $E(t)$ oscillating at ω (excitation frequency) in delay, (third line) the interferogram of the second harmonic oscillating at 2ω and (fourth line) the intensity autocorrelation. General properties of the laser pulse, such as phase and shape, can be deduced from the interferometric autocorrelation trace. The pulse duration can be estimated from the FWHM of the intensity autocorrelation by assuming the pulse shape (generally a sech^2 or a Gaussian shape) and using tabulated ratios between the FWHM of the autocorrelation and that of the pulse. [119, 121] Furthermore, the type of phase modulation could be determined, a linear chirp could be measured and by applying appropriate fitting procedures the complete pulse shape and phase could be extracted. [121] For experimental issues, a good check on the interferometric autocorrelation is that it should be symmetrical and the peak-to-background ratio should be 8:1 for identical collinear pulses and an optimum spatial overlap. The intensity autocorrelation, often called phase-averaged autocorrelation, should exhibit a peak-to-background ratio of 3:1. [120, 121]

As already mentioned above, the measured autocorrelation trace in a photoemission setup is a convolution of the interferometric autocorrelation trace of the laser pulses and the energy and phase relaxation mechanisms of photoexcited electrons. Before introducing a detailed deconvolution procedure given by Refs. [118] and [43], the underlying photoemission processes leading to the so-called interferometric 2-pulse autocorrelation trace of photoemission (I2PC) are briefly discussed by considering a simple three level system, as shown in Fig. 4.28. A pump pulse can excite electrons from a ground state $|0\rangle$ below the Fermi energy either to an intermediate state $|1\rangle$ or directly to a final state $|2\rangle$ above the

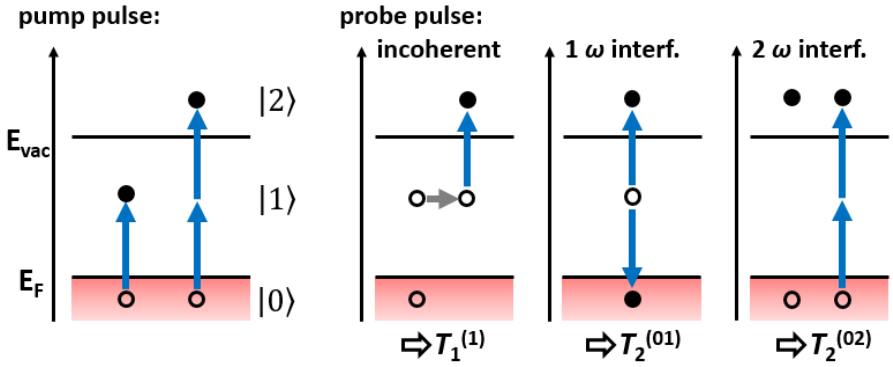

Figure 4.28: Schematic of the two-photon photoexcitation processes by two phase-coherent pulses. Modified from Ref. [118]

vacuum level via two photon absorption. However, due to its electric field the pump pulse induces both a linear and a non-linear polarization, a so-called field induced coupling between the states, which oscillates at the excitation frequency ω and its second harmonic 2ω, corresponding to intermediate and final state. Consequently, before populating intermediate or final states, photoexcited electrons lose their phase relation to the induced polarization by elastic scattering. A probe pulse, now, can interact either coherently with the induced polarization leading to interferences at both ω and 2ω or incoherently with the dephased hot-electron population giving a phase independent component of the autocorrelation trace. Following these considerations, the incoherent process gives information about the energy relaxation time $T_1^{(1)}$ of the intermediate state, whereas interference between the probe pulse and coherent electron-hole polarization at ω and 2ω provides access to phase relaxation times between states $|0\rangle$ and $|1\rangle$ ($T_2^{(01)}$) (or $|1\rangle$ and $|2\rangle$ ($T_2^{(12)}$)), and $|0\rangle$ and $|2\rangle$ ($T_2^{(02)}$). Note that if the decay times are much faster than the pulse width, the I2PC would be identical to an interferometric autocorrelation of the laser pulse. [118] However, a more theoretical approach is given in Ref. [43] describing the time evolution of populations and polarizations associated with the three levels by considering optical Bloch equations.

As a first step of the deconvolution process the phase averaged component, the ω and 2ω envelopes have to be extracted by integrating the measured interferometric 2-pulse correlation trace $I(\tau)$ over each optical cycle [118], as follows:

$$I'_{pa}(\tau') = \frac{c}{\lambda}\int_{\tau'-\lambda/2c}^{\tau'+\lambda/2c} I(\tau)d\tau \tag{4.11}$$

$$I'_{\omega}(\tau') = \frac{2c}{\lambda}\sqrt{\left[\int_{\tau'-\lambda/2c}^{\tau'+\lambda/2c} I(\tau)\cos(\omega\tau)d\tau\right]^2 + \left[\int_{\tau'-\lambda/2c}^{\tau'+\lambda/2c} I(\tau)\sin(\omega\tau)d\tau\right]^2} \tag{4.12}$$

$$I'_{2\omega}(\tau') = \frac{4c}{\lambda}\sqrt{\left[\int_{\tau'-\lambda/4c}^{\tau'+\lambda/4c} I(\tau)\cos(2\omega\tau)d\tau\right]^2 + \left[\int_{\tau'-\lambda/4c}^{\tau'+\lambda/4c} I(\tau)\sin(2\omega\tau)d\tau\right]^2} \tag{4.13}$$

The next step is more complicated as it covers the fitting procedure of each component by using convolution functions. The first part, the energy and phase relaxation, can be assumed as general exponential decay functions, however, the second part of the convolution integral consists of the laser pulse's electric field. The pulse shape and duration, thereby, have to be known in order to obtain reliable results for the time constants. At present, there are several difficulties restricting the implementation of this deconvolution procedure to the interferometric 2-pulse correlation trace measured with the current laser setup Fig. 3.12.

As an example, in Fig. 4.29 the autocorrelation trace of a Bi_2Se_3 surface is shown. As mentioned above, for identical collinear pulses and an optimum spatial overlap a good check on the interferometric autocorrelation can be performed by considering the symmetry and the peak-to-background ratio of 8:1. Both of these conditions are not perfectly satisfied. Possible reasons could be the presence of chirped pulses, insufficient collinearity or a deficient spatial overlap. By scanning the piezo-motorized delay stage with an increment of 50 nm (corresponding to a pump-probe delay of 330 as considering the doubled path) the pre-discussed oscillation at the excitation frequency ω (4710 THz $\widehat{=}$ 1.33 fs $\widehat{=}$ 400 nm $\widehat{=}$ 3.1 eV) can clearly be revealed, as shown in the insert of Fig. 4.29.

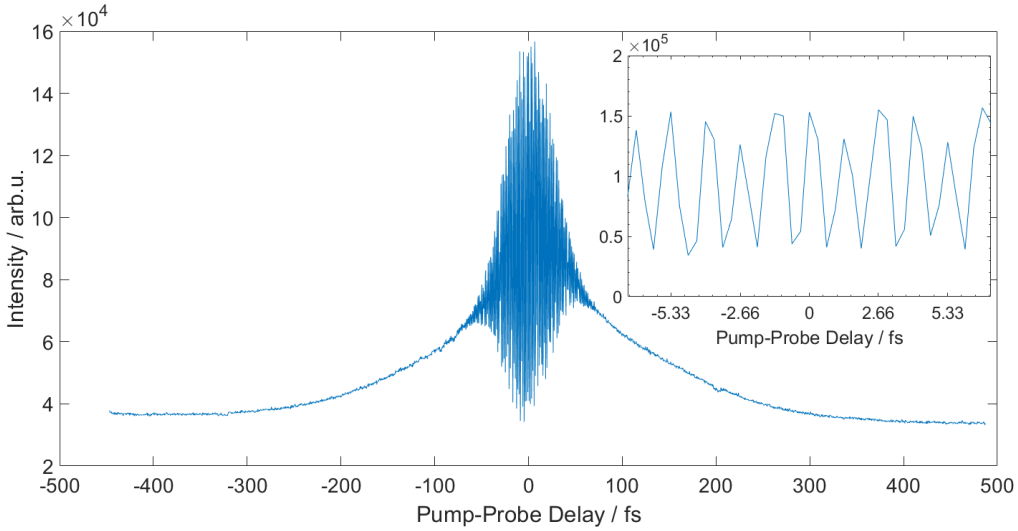

Figure 4.29: The interferometric 2-pulse correlation trace of Bi_2Se_3 measured at $E - E_F = 5.1$ eV. Insert shows the oscillation at the excitation frequency ω originating from the interference between the probe (or pump) pulse and the coherent electron-hole polarization.

Applying Eq. 4.11 to the measured signal, one can extract the phase averaged component, revealing information about the incoherent decay of the hot-electron population. The result of the integration over each optical cycle is depicted in Fig. 4.30(a), showing still an oscillating behaviour around the temporal overlap which complicates the fitting procedure and, furthermore, the decomposition of the frequency envelopes. The Fourier transformation of the interferometric 2-pulse correlation trace of Bi_2Se_3 (Fig. 4.30(b)) reveals several occurring frequencies beside the dominant excitation frequency at 750 THz (400 nm). Note that also a distinct sign of the second harmonic is missing, possibly due

to the large step width of the delay stage. The undesired frequency components could perhaps originate from chirped laser pulses [43], which one more time emphasizes the importance of a pulse characterization measurement.

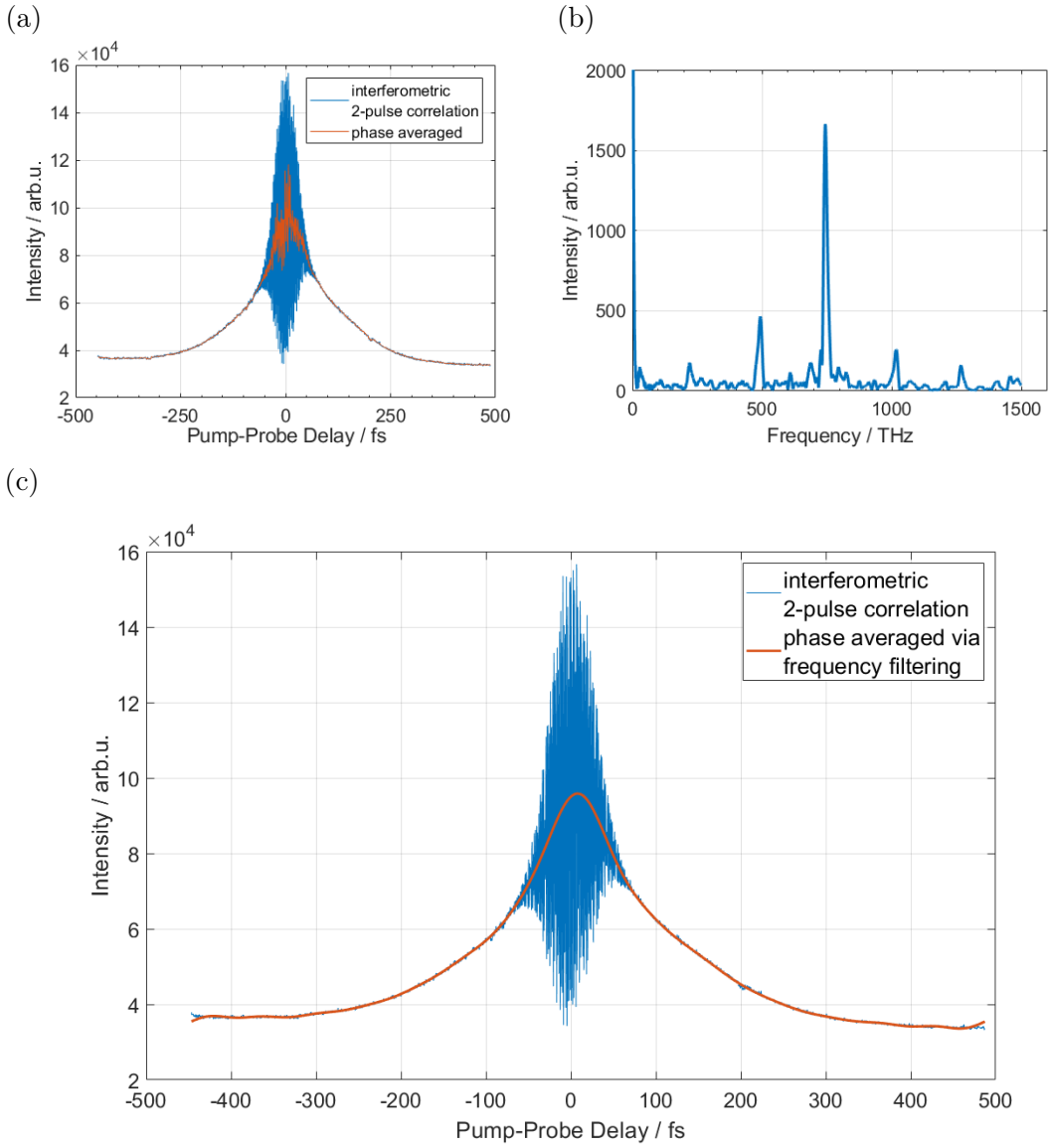

Figure 4.30: (a) The interferometric 2-pulse correlation trace of Bi_2Se_3 and its phase averaged component according to Eq. 4.11. (b) Fourier transformation of the interferometric 2-pulse correlation trace revealing several frequency components beside the excitation frequency at 750 THz. (c) The phase averaged component extracted by high-frequency filtering.

Another, rather qualitative method introduced by Ref. [116], employs filtering of high-frequency components. By substituting the high-frequency components of the Fourier transformation with zero samples and a subsequent inverse transformation, the FWHM

can be extracted from the phase-averaged signal (see Fig. 4.30(c)) reflecting differences in the relaxation dynamics. Fitting of the phase-averaged signal to a Lorentzian function results in a FWHM of approx. 180 fs which would correspond to a pulse duration of approx. 125 fs assuming a Gaussian pulse (pulse duration $\tau = \mathrm{FWHM}/\sqrt{2}$). Single shot autocorrelation measurements of the fundamental laser pulse unveiled a pulse width of approx. 90 fs. By considering that the second harmonic pulses have to travel through a beam splitter, a lens and an UHV-window, a pulse width above 100 fs seems to be plausible, which, consequently, means that the measured signal probably corresponds to the interferometric autocorrelation trace of the pulses and no energy and phase relaxations are involved. This clearly demonstrates the necessity of shorter pulses beside the pulse characterization.

Considering the real space mode, this frequency filtering technique can also be used to display lateral distributions of differences in the relaxation dynamics in terms of a FWHM map. [116]. However, two further difficulties arise for the image acquisition in dependence on the pump-probe delay. The fringe pattern shown in Fig. 4.27(b) manifests as a dramatic obstacle for imaging smaller structures as the pattern moves through the selected area and extinguishes at certain delay times the photoemission signal. This issue has to be further investigated, possibly smaller increments of the delay stage in the attosecond regime could compensate this effect. The second difficulty concerns the reproducibility of the delay stage movement. The sequence of recording follows a distinct scheme: For each pump-probe delay step a 10 s image is acquired, if the scan over time is complete the delay stage will again start at the beginning to record a new series of 10 s images. According to the manufacturer the reproducibility of the motorized actuator used for the Michelson interferometer is specified by 1 μm, restricting an accurate time-resolved measurement. Here, either a more precise delay stage or a reversed measuring sequence, which would need a modification of the current NanoESCA software, could possibly eliminate this problem.

In summary, in order to perform competitive time-resolved measurements in the near future one has to tackle a few challenges, such as the production of shorter laser pulses, the removal of refractive elements, the implementation of an appropriate pulse characterization measurement and a precise measuring scheme.

Chapter 5

Summary and Outlook

This Master's thesis presents first advances and results obtained with the NanoESCA photoemission electron microscope, paving the way for promising future research at the Institute of Experimental Physics.

A detailed description about this novel instrument together with characterization measurements introduces the sophisticated approach for visualizing the distribution of photoelectrons. In particular, the tandem arrangement of two identical hemispherical analysers allows for spectro-microscopy with high spatial, energy and momentum resolution. Employing different light sources reveals the great versatility of the NanoESCA instrument, enabling, for example, the analysis of chemical composition based on work function variations and core-level transitions, the mapping of band structures of single-crystalline surfaces, coherent electronic excitation processes, such as plasmons, and, furthermore, the probing of the temporal evolution of ultrafast processes. Within the scope of this thesis the EF-PEEM has been used to study several systems to show the capability of the microscope for the investigation of the previously mentioned photoemission phenomena.

A prime target was the investigation of nanoparticles, synthesized by the helium droplet approach, with the NanoESCA instrument. Throughout the series of experiments deficiencies have appeared. A major drawback is the spatial resolution of the NanoESCA instrument, which can not be eliminated without the modification of the electron optics and their settings. However, by introducing prefabricated templates (e.g. by electron beam lithography (EBL)) as substrates the arrangement of the deposited nanoparticles could be geared and, furthermore, the focusing procedure, including the correction of the astigmatism, could be improved, establishing an alternative route for visualizing the nanoparticles. Another limitation of the current setup is still the preparation of the substrate, since organic and inorganic contaminations, which drastically influence the photoemission signal, can not be removed as long as the installation of the preparation chamber is incomplete. Thus, comprehensible interpretations about the electronic structure, such as the work function, the valence band and the band gap, are currently complicated. Note that the preparation chamber will also open up new possibilities of the investigation of deposited cluster properties.

In the field of plasmonics a collaboration with the NanoOptics Group at the University of Graz has been initiated in order to obtain EBL test structures for the NanoESCA instrument that can be studied with pulsed laser sources. First results show the applicability for mapping of surface plasmon polaritons (SPP) or, strictly speaking, the Moiré

pattern caused by the interference between the electric field of the laser pulses and the SPPs. Additionally, calculations based on simple geometrical considerations have been applied, showing a good agreement between experiment and theory. Furthermore, recent research has revealed momentum microscopy as a powerful tool for imaging the angular emission distribution of electrons excited from nanostructured surfaces. Wave guides have been used to investigate such momentum-related phenomena and, by illuminating with s-polarized light, a distinct anisotropy of the photoemission horizon has been observed due to an induced dipole field which forces the photoexcited electrons to leave the surface under a preferred direction. However, these wave guides are still subject to current research.

The very first intention of this Master's thesis has been the implementation of an ultrafast pump-probe setup, allowing for time-resolved studies of dynamic processes in plasmonic nanoparticles. In the course of this process several challenges emerged which, unfortunately, proved to be intractable with the available resources. In order to perform competitive research in the field of ultrafast microscopy, shorter pulses, a precise measuring scheme and a pulse characterization measurement are indispensable. First time-resolved results, however, showed the great potential of the NanoESCA instrument together with the stability of the experimental setup as it is already possible to resolve the optical cycles of the laser pulse.

In summary, this work represents the first step towards extremely promising research in the field of photoemission microscopy at the Institute of Experimental Physiscs.

Acknowledgement

We thank the Nano-Optics Group at the University of Graz for providing us nano-structured samples fabricated by electron beam lithography and for fruitful discussions.

Furthermore, we gratefully acknowledge the support of the Surface Science Group at the University of Graz covering the manufacturing of new sample holders, the preparation of single crystals and molecular thin films for first attempts of orbital tomography, and, in particular, the sharing of their know-how in the field of photoemission from solid surfaces.

Bibliography

[1] M. Escher, N. Weber, M. Merkel, C. Ziethen, P. Bernhard, G. Schönhense, S. Schmidt, F. Forster, F. Reinert, B. Krömker, and D. Funnemann. Nanoelectron spectroscopy for chemical analysis: A novel energy filter for imaging x-ray photoemission spectroscopy. *J. Condens. Matter Phys.*, 17(16):S1329–S1338, 2005.

[2] FOCUS GmbH. *Instruction manual FOCUS PEEM*. 2015.

[3] FOCUS GmbH and ScientaOmicron GmbH. *NanoESCA technical reference manual: Instrument*. 2012.

[4] M. Dąbrowski, Y. Dai, and H. Petek. Ultrafast microscopy: Imaging light with photoelectrons on the nano–femto scale. *J. Phys. Chem. Lett.*, 8(18):4446–4455, 2017.

[5] M. C. Patt. *Bulk and surface sensitive energy-filtered photoemission microscopy using synchrotron radiation for the study of resistive switching memories*. Schriften des Forschungszentrums Jülich Reihe Schlüsseltechnologien. Forschungszentrum Jülich, Jülich, 2016.

[6] N. D. Lang and W. Kohn. Theory of metal surfaces: Charge density and surface energy. *Phys. Rev. B*, 1(12):4555–4568, 1970.

[7] J. Friedel. Metallic alloys. *Nuovo Cimento*, 7(2):287–311, 1958.

[8] W. Shockley. On the surface states associated with a periodic potential. *Phys. Rev.*, 56(4):317–323, 1939.

[9] M. W. Cole and M. H. Cohen. Image-potential-induced surface bands in insulators. *Phys. Rev. Lett.*, 23(21):1238–1241, 1969.

[10] P. D. Johnson and N. V. Smith. Image-potential states and energy-loss satellites in inverse photoemission spectra. *Phys. Rev. B*, 27(4):2527–2530, 1983.

[11] M. Z. Hasan and C. L. Kane. Colloquium: Topological insulators. *Rev. Mod. Phys.*, 82(4):3045–3067, 2010.

[12] K. Oura, V. G. Lifshits, A. Saranin, A. V. Zotov, and M. Katayama. *Surface science: An introduction*. Advanced Texts in Physics. Springer-Verlag, Berlin Heidelberg, 2003.

[13] F. Duan and J. Guojun. *Introduction to condensed matter physics*. World Scientific Publishing Company, 2005.

[14] H. Dai. *Laser spectroscopy and photochemistry on metal surfaces*. World Scientific, 1995.

[15] R. W. Schoenlein, J. G. Fujimoto, G. L. Eesley, and T. W. Capehart. Femtosecond studies of image-potential dynamics in metals. *Phys. Rev. Lett.*, 61(22):2596–2599, 1988.

[16] R. W. Schoenlein, J. G. Fujimoto, G. L. Eesley, and T. W. Capehart. Femtosecond dynamics of the n=2 image-potential state on Ag(100). *Phys. Rev. B*, 41(8):5436–5439, 1990.

[17] R. W. Schoenlein, J. G. Fujimoto, G. L. Eesley, and T. W. Capehart. Femtosecond relaxation dynamics of image-potential states. *Phys. Rev. B*, 43(6):4688–4698, 1991.

[18] T. Fauster, P. M. Echenique, and E. V. Chulkov. Electron dynamics at surfaces. In *Surface and Interface Science*, pages 637–678. Wiley-Blackwell, 2014.

[19] E. Wigner and J. Bardeen. Theory of the work functions of monovalent metals. *Phys. Rev.*, 48(1):84–87, 1935.

[20] R. Smoluchowski. Anisotropy of the electronic work function of metals. *Phys. Rev.*, 60(9):661–674, 1941.

[21] O. Renault, R. Brochier, A. Roule, P.-H. Haumesser, B. Krömker, and D. Funnemann. Work-function imaging of oriented copper grains by photoemission. *Surf. Interface Anal.*, 38(4):375–377, 2006.

[22] J. F. Jia, K. Inoue, Y. Hasegawa, W. S. Yang, and T. Sakurai. Variation of the local work function at steps on metal surfaces studied with STM. *Phys. Rev. B*, 58(3):1193–1196, 1998.

[23] J. Topping. On the mutual potential energy of a plane network of doublets. *Proc. Royal Soc. A*, 114(766):67–72, 1927.

[24] E. P. Gyftopoulos and J. D. Levine. Work function variation of metals coated by metallic films. *J. Appl. Phys.*, 33(1):67–73, 1962.

[25] R. W. Verhoef and M. Asscher. The work function of adsorbed alkalis on metals revisited: a coverage-dependent polarizability approach. *Surf. Sci*, 391(1):11–18, 1997.

[26] H. Z. Jooya, K. S. McKay, E. Kim, P. F. Weck, D. P. Pappas, D. A. Hite, and H. R. Sadeghpour. Mechanisms for carbon adsorption on Au(110)-(2x1): A work function analysis. *Surf. Sci*, 677:232–238, 2018.

[27] A. G. Knapp. Surface potentials and their measurement by the diode method. *Surf. Sci*, 34(2):289–316, 1973.

[28] W. Schottky. Über spontane Stromschwankungen in verschiedenen Elektrizitätsleitern. *Ann. Phys.*, 362(23):541–567, 1918.

[29] C. N. Berglund and W. E. Spicer. Photoemission studies of copper and silver: Theory. *Phys. Rev.*, 136(4A):A1030–A1044, 1964.

[30] S. Hüfner. *Photoelectron spectroscopy: Principles and applications*. Springer Series in Solid-State Sciences. Springer-Verlag, Berlin Heidelberg, 2 edition, 1996.

[31] E. Bauer. *Surface microscopy with low energy electrons*. Springer-Verlag, New York, 2014.

[32] H. Hertz. Über einen Einfluss des ultravioletten Lichtes auf die electrische Entladung. *Ann. Phys.*, 267(8):983–1000, 1887.

[33] A. Einstein. Über einen die Erzeugung und Verwandlung des Lichtes betreffenden heuristischen Gesichtspunkt. *Ann. Phys.*, 322(6):132–148, 1905.

[34] R. A. Millikan. A direct photoelectric determination of Planck's "$\hbar$". *Phys. Rev.*, 7(3):355–388, 1916.

[35] F. Reinert and S. Hüfner. Photoemission spectroscopy - from early days to recent applications. *New J. Phys.*, 7:97–97, 2005.

[36] P. J. Feibelman and D. E. Eastman. Photoemission spectroscopy - Correspondence between quantum theory and experimental phenomenology. *Phys. Rev. B*, 10(12):4932–4947, 1974.

[37] J. B. Pendry. Theory of photoemission. *Surf. Sci.*, 57(2):679 – 705, 1976.

[38] M. P. Seah and W. A. Dench. Quantitative electron spectroscopy of surfaces: A standard data base for electron inelastic mean free paths in solids. *Surf. Interface Anal.*, 1(1):2–11, 1979.

[39] A. Klein, T. Mayer, A. Thissen, and W. Jaegermann. Photoelectron spectroscopy in materials science and physical chemistry. *Bunsenmagazin*, 10:124–139, 2008.

[40] K. Giesen, F. Hage, F. J. Himpsel, H. J. Riess, and W. Steinmann. Two-photon photoemission via image-potential states. *Phys. Rev. Lett.*, 55(3):300–303, 1985.

[41] H. Ueba and B. Gumhalter. Theory of two-photon photoemission spectroscopy of surfaces. *Prog. Surf. Sci.*, 82(4):193–223, 2007.

[42] R. Haight. Electron dynamics at surfaces. *Surf. Sci. Rep.*, 21(8):275–325, 1995.

[43] H. Petek and S. Ogawa. Femtosecond time-resolved two-photon photoemission studies of electron dynamics in metals. *Prog. Surf. Sci.*, 56(4):239–310, 1997.

[44] M. Weinelt. Time-resolved two-photon photoemission from metal surfaces. *J. Condens. Matter Phys.*, 14(43):R1099–R1141, 2002.

[45] M. Malvestuto, R. Ciprian, A. Caretta, B. Casarin, and F. Parmigiani. Ultrafast magnetodynamics with free-electron lasers. *J. Phys.: Condens. Matter*, 30(5):053002, 2018.

[46] T. Mii and H. Ueba. Theory of time-resolved two-photon photoemission spectroscopy from metal surfaces. *J. Lumin.*, 87-89:898–901, 2000.

[47] M. Escher, K. Winkler, O. Renault, and N. Barrett. Applications of high lateral and energy resolution imaging XPS with a double hemispherical analyser based spectromicroscope. *J. Electron Spectrosc. Relat. Phenom.*, 178-179:303–316, 2010.

[48] R. M. Tromp, J. B. Hannon, A. W. Ellis, W. Wan, A. Berghaus, and O. Schaff. A new aberration-corrected, energy-filtered LEEM/PEEM instrument. I. Principles and design. *Ultramicroscopy*, 110(7):852–861, 2010.

[49] R. M. Tromp, J. B. Hannon, W. Wan, A. Berghaus, and O. Schaff. A new aberration-corrected, energy-filtered LEEM/PEEM instrument II. Operation and results. *Ultramicroscopy*, 127:25–39, 2013.

[50] M. C. Patt, C. Wiemann, N. Weber, M. Escher, A. Gloskovskii, W. Drube, M. Merkel, and C. M. Schneider. Bulk sensitive hard x-ray photoemission electron microscopy. *Rev. Sci. Instrum.*, 85(11):113704, 2014.

[51] J.A.R. Samson. *Techniques of vacuum ultraviolet spectroscopy*. Wiley series in pure and applied spectroscopy. Pied Publications, 1967.

[52] G. Schonhense and U. Heinzmann. A capillary discharge tube for the production of intense VUV resonance radiation. *J. Phys. E: Sci. Instrum.*, 16(1):74–82, 1983.

[53] FOCUS GmbH. *VUV source HIS 13 / HIS 14 HD and HIS Mono - Instruction manual*. Version 3.4 edition, 2018.

[54] A. Pifrader. Pulsed laser spectroscopic investigations of rubidium atoms attached to helium nanodroplets, 2009. Diploma thesis.

[55] Positive Light Inc. *Indigo-S laser operator's manual*. Coherent Inc., Santa Clara, CA, 2004.

[56] Coherent Inc. *Indigo-S operating procedures*. Coherent Inc., Santa Clara, CA, 2005.

[57] Coherent Inc. *Operator's manual vitara modelocked Ti:S laser*. Santa Clara, CA, 2011.

[58] C. Rulliere. *Femtosecond laser pulses: Principles and experiments*. Advanced Texts in Physics. Springer-Verlag, New York, 2 edition, 2005.

[59] Newport Corp. Precision motorized actuators, 2018.

[60] Newport Corp. Single-axis DC or stepper motion controller - SMC100, 2017.

[61] J. Stohr and S. Anders. X-ray spectro-microscopy of complex materials and surfaces. *IBM J. Res. Dev.*, 44(4):535–551, 2000.

[62] H.-J. Freund, N. Nilius, T. Risse, S. Schauermann, and T. Schmidt. Innovative measurement techniques in surface science. *ChemPhysChem*, 12(1):79–87, 2011.

[63] M. Escher, N. Weber, M. Merkel, B. Krömker, D. Funnemann, S. Schmidt, F. Reinert, F. Forster, S. Hüfner, P. Bernhard, Ch. Ziethen, H. J. Elmers, and G. Schönhense. NanoESCA: Imaging UPS and XPS with high energy resolution. *J. Electron Spectrosc. Relat. Phenom.*, 144-147:1179–1182, 2005.

[64] M. Cattelan and N. A. Fox. A perspective on the application of spatially resolved ARPES for 2d materials. *Nanomater.*, 8(5):284, 2018.

[65] A. Damascelli. Probing the electronic structure of complex systems by ARPES. *Phys. Scr.*, T109:61, 2004.

[66] P. Aebi, J. Osterwalder, R. Fasel, D. Naumović, and L. Schlapbach. Fermi surface mapping with photoelectrons at UV energies. *Surf. Sci*, 307-309:917–921, 1994.

[67] N. M. Buckanie, J. Göhre, P. Zhou, D. von der Linde, M. Horn-von Hoegen, and F.-J. Meyer zu Heringdorf. Space charge effects in photoemission electron microscopy using amplified femtosecond laser pulses. *J. Condens. Matter Phys.*, 21(31):314003, 2009.

[68] M. Wießner, D. Hauschild, C. Sauer, V. Feyer, A. Schöll, and F. Reinert. Complete determination of molecular orbitals by measurement of phase symmetry and electron density. *Nat. Commun.*, 5:4156, 2014.

[69] D. Luftner, T. Ules, E. M. Reinisch, G. Koller, S. Soubatch, F. S. Tautz, M. G. Ramsey, and P. Puschnig. Imaging the wave functions of adsorbed molecules. *Proc. Natl. Acad. Sci.*, 111(2):605–610, 2014.

[70] M. Willenbockel, D. Lüftner, B. Stadtmüller, G. Koller, C. Kumpf, S. Soubatch, P. Puschnig, M. G. Ramsey, and F. S. Tautz. The interplay between interface structure, energy level alignment and chemical bonding strength at organic-metal interfaces. *Phys. Chem. Chem. Phys.*, 17(3):1530–1548, 2015.

[71] M. B. Gawande, A. Goswami, T. Asefa, H. Guo, Ankush V. Biradar, D.-L. Peng, R. Zboril, and R. S. Varma. Core–shell nanoparticles: synthesis and applications in catalysis and electrocatalysis. *Chem. Soc. Rev.*, 44(21):7540–7590, 2015.

[72] H. A. Atwater and A. Polman. Plasmonics for improved photovoltaic devices. *Nat. Mater.*, 9(3):205–213, 2010.

[73] J. M. Luther and J. L. Blackburn. Optoelectronics: Plasmon-enhanced plastic devices. *Nat. Photonics*, 7(9):675–677, 2013.

[74] P. K. Jain, I. H. El-Sayed, and M. A. El-Sayed. Au nanoparticles target cancer. *Nano Today*, 2(1):18–29, 2007.

[75] F. Lackner, A. Schiffmann, M. Lasserus, R. Messner, M. Schnedlitz, H. Fitzek, P. Pölt, D. Knez, G. Kothleitner, and W. E. Ernst. Helium nanodroplet assisted synthesis of bimetallic Ag@Au nanoparticles with tunable localized surface plasmon resonance. *Eur. Phys. J. D*, 73(5):104, 2019.

[76] A. Schiffmann, D. Knez, F. Lackner, M. Lasserus, Roman Messner, M. Schnedlitz, G. Kothleitner, F. Hofer, and W. E. Ernst. Ultra-thin h-BN substrates for nanoscale plasmon spectroscopy. *J. Appl. Phys.*, 125(2):023104, 2019.

[77] J. P. Toennies and A. F. Vilesov. Superfluid helium droplets: A uniquely cold nanomatrix for molecules and molecular complexes. *Angew. Chem. Int. Ed.*, 43(20):2622–2648, 2004.

[78] C. Callegari and W. E. Ernst. *In: Handbook of High-Resolution Spectroscopy, Chapter: Helium droplets as nanocryostats for molecular spectroscopy - from the vacuum ultraviolet to the microwave regime*, edited by M. Quack and F. Merkt (John Wiley & Sons, Chichester, 2011), pp. 1551–1594, ISBN: 978-0-470-06653-9.

[79] M. Rohmer, F. Ghaleh, M. Aeschlimann, M. Bauer, and H. Hövel. Mapping the femtosecond dynamics of supported clusters with nanometer resolution. *Eur. Phys. J. D*, 45:491–499, 2007.

[80] D. Bayer, J. Lange, C. Wiemann, M. Rohmer, M. Bauer, and M. Aeschlimann. Time and space resolved studies on metallic nanoparticles. pages 61–68. 2009.

[81] T. Nakamura, N. Hirata, S. Nagaoka, and A. Nakajima. Two-photon photoemission spectroscopy for silver nanoparticles on a hydrogen-terminated Si(111) surface: Metal nanoparticle-enhanced photoemission. *Chem. Phys. Lett.*, 489(1):69–74, 2010.

[82] S. Tan, L. Liu, Y. Dai, J. Ren, J. Zhao, and H. Petek. Ultrafast plasmon-enhanced hot electron generation at Ag nanocluster/graphite heterojunctions. *J. Am. Chem. Soc.*, 139(17):6160–6168, 2017.

[83] A. Volk, P. Thaler, M. Koch, E. Fisslthaler, W. Grogger, and W. E. Ernst. High resolution electron microscopy of Ag-clusters in crystalline and non-crystalline morphologies grown inside superfluid helium nanodroplets. *J. Chem. Phys.*, 138(21):214312, 2013.

[84] A. Volk, P. Thaler, D. Knez, A. W. Hauser, J. Steurer, W. Grogger, F. Hofer, and W. E. Ernst. The impact of doping rates on the morphologies of silver and gold nanowires grown in helium nanodroplets. *Phys. Chem. Chem. Phys.*, 18(3):1451–1459, 2016.

[85] A. Volk, D. Knez, P. Thaler, A. W. Hauser, W. Grogger, F. Hofer, and W. E. Ernst. Thermal instabilities and Rayleigh breakup of ultrathin silver nanowires grown in helium nanodroplets. *Phys. Chem. Chem. Phys.*, 17(38):24570–24575, 2015.

[86] T. Jauk. Localized surface plasmon resonances of gold nano-clusters investigated by UV/VIS spectrophotometry, August 2017. Bachelor thesis.

[87] P. Thaler, A. Volk, D. Knez, F. Lackner, G. Haberfehlner, J. Steurer, M. Schnedlitz, and W. E. Ernst. Synthesis of nanoparticles in helium droplets - A characterization comparing mass-spectra and electron microscopy data. *J. Chem. Phys.*, 143(13):134201, 2015.

[88] L. F. Gomez, E. Loginov, R. Sliter, and A. F. Vilesov. Sizes of large He droplets. *J. Chem. Phys.*, 135(15):154201, 2011.

[89] P. Thaler, A. Volk, M. Ratschek, M. Koch, and W. E. Ernst. Molecular dynamics simulation of the deposition process of cold Ag-clusters under different landing conditions. *J. Chem. Phys.*, 140(4):044326, 2014.

[90] V. N. Popok, I. Barke, E. E. B. Campbell, and K.-H. Meiwes-Broer. Cluster-surface interaction: From soft landing to implantation. *Surf. Sci. Rep.*, 66(10):347–377, 2011.

[91] E. Loginov, L. F. Gomez, and A. F. Vilesov. Surface deposition and imaging of large Ag clusters formed in He droplets. *J. Phys. Chem. A*, 115(25):7199–7204, 2011.

[92] A. W. Dweydari and C. H. B. Mee. Work function measurements on (100) and (110) surfaces of silver. *Phys. Status Solidi A*, 27(1):223–230, 1975.

[93] L. Zhou and M. R. Zachariah. Size resolved particle work function measurement of free nanoparticles: Aggregates vs. spheres. *Chem. Phys. Lett.*, 525-526:77–81, 2012.

[94] G. Panaccione, G. Cautero, M. Cautero, A. Fondacaro, M. Grioni, P. Lacovig, G. Monaco, F. Offi, G. Paolicelli, M. Sacchi, N. Stojić, G. Stefani, R. Tommasini, and P. Torelli. High-energy photoemission in silver: Resolving d and sp contributions in valence band spectra. *J. Phys.: Condens. Matter*, 17(17):2671, 2005.

[95] R. Fink, M. R. Weiss, E. Umbach, D. Preikszas, H. Rose, R. Spehr, P. Hartel, W. Engel, R. Degenhardt, R. Wichtendahl, H. Kuhlenbeck, W. Erlebach, K. Ihmann, R. Schlögl, H. J. Freund, A. M. Bradshaw, G. Lilienkamp, Th. Schmidt, E. Bauer, and G. Benner. SMART: A planned ultrahigh-resolution spectromicroscope for BESSY II. *J. Electron Spectrosc. Relat. Phenom.*, 84(1):231–250, 1997.

[96] J. Lehmann, M. Merschdorf, W. Pfeiffer, A. Thon, S. Voll, and G. Gerber. Surface plasmon dynamics in silver nanoparticles studied by femtosecond time-resolved photoemission. *Phys. Rev. Lett.*, 85(14):2921–2924, 2000.

[97] National Institute of Standards and Technology (U.S.). *NIST X-ray photoelectron spectroscopy database*. NIST Standard Reference Database Number 20. Gaithersburg, MD, 2012. (retrieved 24.10.2019).

[98] M. S. Raven. XPS and Auger LMM analysis of ZnO/Si and ZnO/SiO2 interfaces. *Surf. Interface Anal.*, 1(1):20–25, 1979.

[99] K. B. Sundaram and A. Khan. Work function determination of zinc oxide films. *J. Vac. Sci. Technol. A.*, 15(2):428–430, 1997.

[100] M. Lasserus, M. Schnedlitz, R. Messner, F. Lackner, W. E. Ernst, and A. W. Hauser. Vanadium(V) oxide clusters synthesized by sublimation from bulk under fully inert conditions. *Chem. Sci.*, 10(12):3473–3480, 2019.

[101] M. Lasserus, D. Knez, F. Lackner, M. Schnedlitz, Roman Messner, D. Schennach, G. Kothleitner, F. Hofer, A. W. Hauser, and W. E. Ernst. Synthesis of nanosized vanadium(V) oxide clusters below 10 nm. *Phys. Chem. Chem. Phys.*, 21(37):21104–21108, 2019.

[102] J. Meyer, K. Zilberberg, T. Riedl, and A. Kahn. Electronic structure of Vanadium pentoxide: An efficient hole injector for organic electronic materials. *J. Appl. Phys.*, 110(3):033710, 2011.

[103] A. Chakrabarti, K. Hermann, R. Druzinic, M. Witko, F. Wagner, and M. Petersen. Geometric and electronic structure of vanadium pentoxide: A density functional bulk and surface study. *Phys. Rev. B*, 59(16):10583–10590, 1999.

[104] S. A. Maier. *Plasmonics: Fundamentals and applications*. Springer US, New York, NY, 2007.

[105] J. M. Fitzgerald, P. Narang, R. V. Craster, S. A. Maier, and V. Giannini. Quantum plasmonics. *Proc. IEEE*, 104(12):2307–2322, 2016.

[106] E. Ozbay. Plasmonics: Merging photonics and electronics at nanoscale dimensions. *Science*, 311(5758):189–193, 2006.

[107] Y. Dai and H. Petek. Plasmonic spin-Hall effect in surface plasmon polariton focusing. *ACS Photonics*, 6(8):2005–2013, 2019.

[108] Y. Fang, Y. Jiao, K. Xiong, R. Ogier, Zhong-Jian Yang, S. Gao, A. B. Dahlin, and M. Käll. Plasmon enhanced internal photoemission in antenna-spacer-mirror based Au/TiO2 nanostructures. *Nano Lett.*, 15(6):4059–4065, 2015.

[109] J. N. Anker, W. P. Hall, O. Lyandres, N. C. Shah, J. Zhao, and R. P. Van Duyne. Biosensing with plasmonic nanosensors. *Nat. Mater.*, 7(6):442–453, 2008.

[110] A. Kubo, N. Pontius, and H. Petek. Femtosecond microscopy of surface plasmon polariton wave packet evolution at the silver/vacuum interface. *Nano Lett.*, 7(2):470–475, 2007.

[111] L. Zhang, A. Kubo, L. Wang, H. Petek, and T. Seideman. Imaging of surface plasmon polariton fields excited at a nanometer-scale slit. *Phys. Rev. B*, 84(24):245442, 2011.

[112] N. M. Buckanie, P. Kirschbaum, S. Sindermann, and F. J. Meyer zu Heringdorf. Interaction of light and surface plasmon polaritons in Ag islands studied by nonlinear photoemission microscopy. *Ultramicroscopy*, 130:49–53, 2013.

[113] M. Lehr, B. Foerster, M. Schmitt, K. Krüger, C. Sönnichsen, G. Schönhense, and H. J. Elmers. Momentum distribution of electrons emitted from resonantly excited individual gold nanorods. *Nano Lett.*, 17(11):6606–6612, 2017.

[114] M. Lehr, K. Bley, N. Vogel, B. Rethfeld, G. Schönhense, and H. J. Elmers. Evidence of spatially inhomogeneous electron temperature in a resonantly excited array of bow-tie nanoantennas. *J. Phys. Chem. C*, 123(19):12429–12436, 2019.

[115] A. D. Rakić. Algorithm for the determination of intrinsic optical constants of metal films: application to aluminum. *Appl. Opt.*, 34(22):4755–4767, 1995.

[116] O. Schmidt, M. Bauer, C. Wiemann, R. Porath, M Scharte, O. Andreyev, G. Schönhense, and M. Aeschlimann. Time-resolved two photon photoemission electron microscopy. *Appl. Phys. B*, 74:223–227, 2002.

[117] F.-J. Meyer zu Heringdorf, L.I. Chelaru, S. Möllenbeck, D. Thien, and M. Horn-von Hoegen. Femtosecond photoemission microscopy. *Surf. Sci*, 601(20):4700–4705, 2007.

[118] W. Nessler, S. Ogawa, H. Nagano, H. Petek, J. Shimoyama, Y. Nakayama, and K. Kishio. Energy relaxation and dephasing times of excited electrons in $Bi_2Sr_2CaCu_2O_{8+\delta}$ from interferometric 2-photon time-resolved photoemission. *J. Electron Spectrosc.*, 88-91:495–501, 1998.

[119] J.-C. M. Diels, J. J. Fontaine, I. C. McMichael, and F. Simoni. Control and measurement of ultrashort pulse shapes (in amplitude and phase) with femtosecond accuracy. *Appl. Opt.*, 24(9):1270, 1985.

[120] R. Trebino. *Frequency-resolved optical gating: The measurement of ultrashort laser pulses*. Springer US, 2000.

[121] J.-C. M. Diels and W. Rudolph. *Ultrashort laser pulse phenomena: fundamentals, techniques, and applications on a femtosecond time scale*. Optics and photonics. Elsevier / Academic Press, Amsterdam ; Boston, 2nd ed edition, 2006.

Danksagung

„Keine Schuld ist dringender, als die, Dank zu sagen.“ Mit den Worten von Marcus Tullius Cicero möchte ich mich an all jene richten, die zu dieser Arbeit einen wertvollen Beitrag geleistet haben, und gleichzeitig um Verzeihung bitten für die folgenden Worte. (Meine literarische Ader ist wohl mit mir durchgegangen.)

Ohne ihn wäre all dies nicht möglich gewesen: Mein Betreuer Prof. Wolfgang E. Ernst. Wissen, Erfahrung und Motivation sind verantwortungsvolle Güter, die richtig kommuniziert, Begeisterung für eine wissenschaftliche Karriere wecken können. Mit großer Weitsicht hat Prof. Ernst dafür Sorge getragen, dass mit dem NanoESCA Photoemissionselektronenmikroskop am Institut weiterhin, gewiss für Jahrzehnte, bereichernde und faszinierende Forschung betrieben werden kann, und dass ich als einer der ersten - als Pionier - einen bedeutenden Teil dazu beisteuern durfte.

Gut zu wissen, dass es jemanden gibt, an den man sich jederzeit wegen jeder Kleinigkeit wenden kann: Mein Ko-Betreuer Florian Lackner. Fleiß, Begeisterung und Freude im und außerhalb des Labors, Tugenden, die er zu vermitteln weiß. Bei manch anregenden und auch heiteren Diskussionen über diverse Publikationen, angefangen bei Hrvoje Petek, über Martin Aeschlimann bis hin zu Hajo Freund, konnte er in mir einen Forschungsdrang wecken, der nun wartet gestillt zu werden.

Gemeinsame Stunden im Labor prägen doch am meisten die Zeit einer Masterarbeit: Alexander Schiffmann. Ordnung, kritisches Hinterfragen und Perfektion, um es mit den Worten von Florian zu sagen: Es ist gut, einen Alex in der Gruppe zu haben. Nicht nur die gemeinsame Arbeit, auch die interessanten Gespräche über Tagespolitik und Weltgeschehen werden stets in Erinnerung bleiben, bis wohl der letzte Matchball gespielt werden wird ;).

Soziale Aktivitäten, wie Kaffeepausen, Mittagessen und spannende Groupmeetings, stärken die Atmosphäre und das Gefüge in einer Forschungsgruppe: Maximilian Lasserus, Roman Messner und Martin Schnedlitz. Humor, Geduld und Kreativität, Eigenschaften, die im Leben nicht verloren gehen sollten. Hitzige, aber auch argumentative Diskussionen, geführt von drei vollkommen unterschiedlichen Charakteren, durfte ich genießen und gaben mir jedoch immer wieder gute Denkanstöße.

Über den eigenen „Forschungstellerrand“ hinauszublicken: Femtoguys, Heliumstreuer und die Hauser-Group. Laserpulse, Oberflächen und Theorie. Der Austausch mit den anderen Gruppen verhalf mir Unverstandenes zu verstehen und neues in Angriff zu nehmen.

Ohne sie wäre der Studienalltag nur halb so erträglich gewesen: Jakob Wilhelm Hinum-Wagner, Stefan Fortmüller und Felix Hajek. Prüfungen, Übungszettel und Protokolle konnten gemeinsam mit dem einen oder anderen Späßchen bewältigt werden.

Und zu guter Letzt: Meinen Eltern. Leben, Finanzen und Entscheidungsfreiheit, ohne dies wäre ein erfolgreiches Studium nie möglich gewesen. Danke!